SANDIA REPORT
SAND2008-5184
Unlimited Release
Printed August 2008

The Sandia MEMS Passive Shock Sensor: FY07 Maturation Activities

John A. Mitchell, Michael S. Baker, Jill Blecke, Rebecca C. Clemens, Douglas A. Crowson, David S. Epp, Jack E. Houston, Jeremy A. Walraven, Jonathan W. Wittwer

Prepared by
Sandia National Laboratories
Albuquerque, New Mexico 87185 and Livermore, California 94550

Sandia is a multiprogram laboratory operated by Sandia Corporation,
a Lockheed Martin Company, for the United States Department of Energy's
National Nuclear Security Administration under Contract DE-AC04-94AL85000.

Issued by Sandia National Laboratories, operated for the United States Department of Energy by Sandia Corporation.

Available to DOE and DOE contractors from
U.S. Department of Energy
Office of Scientific and Technical Information
P.O. Box 62
Oak Ridge, TN 37831

Telephone: (865) 576-8401
Facsimile: (865) 576-5728
E-Mail: reports@adonis.osti.gov
Online ordering: http://www.osti.gov/bridge

Available to the public from
U.S. Department of Commerce
National Technical Information Service
5285 Port Royal Rd.
Springfield, VA 22161

Telephone: (800) 553-6847
Facsimile: (703) 605-6900
E-Mail: orders@ntis.fedworld.gov
Online order: http://www.ntis.gov/help/ordermethods.asp?loc=7-4-0#online

SAND2008-5184
Unlimited Release
Printed August 2008

The Sandia MEMS Shock Sensor: FY07 Maturation Activities

John A. Mitchell, Rebecca C. Clemens
Electromechanical Engineering Department

Michael S. Baker, Jonathan W. Wittwer
MEMS Technologies Department

Jill Blecke, David S. Epp
Applied Mechanics Department

Douglas A. Crowson, Jack E. Houston
Surface and Interface Sciences Department

Jeremy A. Walraven
Failure Analysis Department

Sandia National Laboratories
P.O. Box 5800
Albuquerque, New Mexico 87185-MS1064

Abstract

This report describes activities conducted in FY07 to mature the MEMS passive shock sensor. The first chapter of the report provides motivation and background on activities that are described in detail in later chapters. The second chapter discusses concepts that are important for integrating the MEMS passive shock sensor into a system. Following these two introductory chapters, the report details modeling and design efforts, packaging, failure analysis and testing and validation. At the end of FY07, the MEMS passive shock sensor was at TRL 4.

Acknowledgments

The authors gratefully acknowledge funding and support from the Embedded Evaluation program run by Bob Paulsen and Paul Yoon, the Campaign 6 program run by T. Y. Chu, the Campaign 5 program run by Davina Kwon, the DSW Campaign run by Mike Sjulin and Russ Miller, and the overall support and guidance of Mary Gonzales. Without this support the accomplishments documented here would have not been possible. Finally, special thanks go to Patricia Oliver for helping to create the form and legibility of the report.

CONTENTS

FIGURES

TABLES

NOMENCLATURE

AutoCAD®	Computer-aided drafting product of AutoDesk, Inc.
CDA	Clean dry air
CIVA	Charge-induced voltage alteration
COR	Coefficient of restitution
COTS	Commercial off-the-shelf
CTE	Coefficient of thermal expansion
DIP	Dual inline package
DUT	Device under test
EE	Embedded evaluation
FEA	Finite element analysis
FIB	Focused ion beam
FRF	Frequency response function
FSP	First stable position
GCMS	Gas chromatograph/mass spectrometer
IC	Integrated circuit
IFM	Interfacial force microscope
Kovar™	Vacuum melted, iron-nickel-cobalt, low expansion alloy from Carpenter Technology Corporation
LCC	Leadless chip carrier
LDV	Laser Doppler vibrometer
LED	Light-emitting diode
LDV	Laser Doppler vibrometer
LHS	Latin hypercube sampling
LIVA	Light-induced voltage alteration
MATLAB®	"MATrix LABoratory" commercial software from The MathWorks, Inc.
MEMS	Micro-electro-mechanical systems
OBIRCH	Optical-beam induced resistance change
PCB	Printed circuit board
PID controller	Proportional–integral–derivative controller
PSS	Passive shock sensor switch
PTC	Product temperature control
RF	Radio frequency
RS	Reticle set
SDOF	Single degree of freedom
SEM	Scanning electron microscope
SNL	Sandia National Laboratories
SOM	Scanning optical microscope

SSP	Second stable position
SUMMiT V™	Sandia ultra-planar, multi-level MEMS technology 5
TIVA	Thermally induced voltage alteration
TRL	Technology readiness level
UEP	Unstable equilibrium position
VCSEL	Vertical-cavity surface-emitting laser
WETL	Weapons Evaluation Test Laboratory

1. INTRODUCTION

1.1 Report Scope and Objectives

In FY06, a prototype design for a Micro Electro Mechanical Systems (MEMS) passive shock sensor was developed and documented under the Embedded Evaluation (EE) program. The present report documents activities related to the maturation of the sensor in FY07 including development of requirements specifications, design, analysis, packaging, fabrication, and testing. Because this is a follow-up report, it does not provide all the basic background information available in Sandia Report 2006-5806 [1].

1.2 FY07 Project Goals

In FY06, "proof of concept" was demonstrated for a packaged shock switch in the laboratory, thereby achieving technology readiness level (TRL) 4 for the sensor. Ultimately our goal is to mature the shock sensor to TRL 6. To facilitate this, our FY07 goals included identifying functional, environmental and integration requirements for the shock sensor. Our FY07 goals also included exposing the shock sensors to thermal, vibration, and over-shock environments; developing and maturing a packaging solution; modeling and validation efforts; and understanding and minimizing the off-axis response of the switch. The team also worked to develop specific functional requirements for the shock sensor. This included establishing the desired inertial magnitude and bandwidth the shock sensor is required to detect as well as packaging requirements dictating the number and orientation of individual sensors on the packaged die.

1.3 Approach

In this section, we describe the guiding principles and approach taken to mature the passive shock sensor. The team used technology readiness levels ([2], [3]) criterion as guide posts and identified the following concepts related to maturation of the shock sensors:

- Functional requirements: inertial magnitude and pulse width, number and orientation of sensors on a die
- Key elements: spring flexures, packaging, thermal actuators, contacts, latching/unlatching
- Relevant environments: thermal, shock, vibration
- Customer integration: packaging that addresses inputs/outputs and mechanisms for attach
- Technology integration: integrating key elements and considering protection against adverse effects of environments

For reference, we list the Sandia definitions for technology readiness levels 5 and 6:

5) Key elements demonstrated in relevant environments
Fidelity of the key elements increases significantly. Key elements are integrated with realistic supporting elements so that the technology can be tested and demonstrated in simulated or actual environments.

6) Representative of the deliverable demonstrated in relevant environments

Represents a major step in a technology's demonstrated readiness. Examples include testing a prototype or representative of a deliverable in a high fidelity laboratory environment or in a simulated operational environment.

In the following subsections, we discuss FY07 activities. As a preface, we refer to and reflect on lessons learned and documented in FY06.

1.3.1 FY06: Lessons Learned

Hindsight and elapsed time allows for an improved measure of past accomplishments and a clearer vision of the path forward. The previously published report [1] includes section 2.2.5 entitled "Known issues and path forward for the micro-scale shock sensor." For purposes of continuity and for helping to clarify the path forward and challenges ahead, the aforementioned section is included in its entirety in *italics* below.

1. *General tendency of the model to under-predict set point. This has been described in previous sections, and will be addressed by continuing to focus on model accuracy and model validation in future designs.*
2. *Sensitivity of device to z-axis loads (normal to the plane of the substrate). Hammer strike and drop table tests have shown that the devices are very sensitive to z-axis loads, resulting in a softening of the in-plane stiffness (see section 5.3.2.2). In extreme cases this can result in the switch closing only due to z-axis loading. The ANSYS model predicts this behavior, so it can be useful as a design tool to minimize the effect. It has been shown that the lower force mechanisms are less sensitive to z-axis loading, implying that improvements could be made through a redesign of the springs where z-axis sensitivity becomes a key design parameter. In addition, process modifications to allow for thicker layers would have an impact on z-axis stiffness. Finally, the use of dimples in the process to limit the amount of z-axis travel would also decrease z-axis loading sensitivity. These solutions will be explored in the next design revision.*
3. *Sticking of the sense mass to the P4 shadow mask during metallization and packaging. We currently believe that the packaging and metallization process is causing the sense mass to deflect and stick to the P4 lid. The thermal actuator is not strong enough to free the mass but it can be freed manually by pushing on it with a probe tip. Once free, the device functions normally thereafter. This could be due to temperature cycles involved in both processes and we are currently testing this theory to confirm the source of the problem. Dimples added to the proof mass may eliminate the issue. This approach will be implemented in the next design iteration.*
4. *While not currently a problem, a final packaging solution needs to be explored. The package must be able to withstand shock levels well above levels the shock sensors are expected to detect as well as withstand expected thermal environments. It must also integrate easily within the customer's system both mechanically and electrically including methods/mechanisms for attachment to the platform being sensed. This is a need that will be addressed with funding in FY07.*

The FY07 design activities conducted for developing Revision 2 of the MEMS passive shock sensor die specifically address items 1, 2, and 3 above. The team also focused a significant amount of resources and efforts towards addressing item 4 in FY07.

There is a fundamental difference between items (1,2,3) and item 4. The former are directly related to the MEMS die-level design and fabrication (R&D leaning) whereas item 4 more closely aligns with the required engineering to deliver the shock sensor to a customer. To deliver the MEMS passive shock sensor, it is necessary to continue with die-level development, but that must be nearly equally balanced with packaging and attention to customer related details.

It is worth noting that in FY06 the deliverable was a laboratory demonstration of the shock sensor and its basic features: environmentally actuated, passive, latching/unlatching. With regard to reliability we note that the number of devices packaged and tested in FY06 was low—sufficiently low to make it difficult to fully characterize the switches in terms of shock threshold/pulse width. One of the goals for FY07 was to package and test sufficient number of devices to characterize and verify the following customer-centric features:

- *Environmental thresholds for closing the switch.*
- *Latch hold*: once the switch has closed/latched, how easy is it to re-open environmentally?
- *Reliability with regard to re-use*: In FY06, while numbers were low, there was some indication that failure rates were relatively high. In FY07, our goal was to gather additional information.

1.3.2 Functional Requirements

From a customer point of view, the passive shock sensor detects shock/impact and may be deployed as a sensor to a particular shock level or shock event. If the shock level is exceeded, the shock sensor closes a set of contacts. Continuity across the contacts may be monitored in the electrical system. Power is required only to open or close the contacts and read the sensor state. This description loosely fits as functional requirements but lacks specificity and requires further development.

From an implementation point of view, the passive shock sensor may be viewed as a shock filter, filtering shock magnitude, direction, and duration. For brevity we will refer to the shock sensor characteristics (response to magnitude and duration) as the bandwidth of the switch. Successfully deploying a shock switch requires understanding the system that the switch will be integrated within. Shock waves disperse out from the location of the impinging shock initiator, and subsequently ring the system to some extent. Damping is inherent in nearly all systems and the shock is dissipated. There are two obvious use cases for the passive shock sensor and we describe them in the following two subsections. In both cases, the shock switch bandwidth must be well understood. However, the required level of system understanding for integration of the shock sensors is different.

1.3.2.1 Use Case: Detecting a Particular Shock Event

Very careful attention must be given to sensor placement. Placement of the sensor requires a thorough understanding of the system and the expected shock event so that the local system response can be matched with the sensor bandwidth. As an example, consider placing the sensor directly adjacent to the location of impinging shock. The sensor would logically experience higher g-levels and shorter pulse widths than it would if it were placed some distance away where intervening geometrical and material boundaries would necessarily attenuate and disperse shock waves. Understanding this tradeoff and matching the switch response to the underlying system is critical. For the MEMS passive shock sensor, it may be beneficial to add multiple devices on a die in order to broaden the bandwidth or to increase reliability. These design choices can be finally made only after detailed analysis of the specific system and the expected shock event.

1.3.2.2 Use Case: Screening Operations to Identify Over-Shock Events

Careful thought should be given to the shock threshold that the system/component should be protected against. Once this threshold is established, the shock sensor can be designed to trigger for this threshold. This use case can be challenging if the threshold is not within the achievable bandwidth of the sensor. Obviously, the threshold environment must be specified in order to design and deploy an appropriate shock sensor.

1.3.3 Identification of Key Elements

To deploy any technology successfully, it is necessary to advance and develop individual elements of the technology. The final deployment integrates the individual elements in a way that comprises the functional capability that a customer seeks. The MEMS passive shock sensor includes the following key elements:

- Spring flexures, mass element, latching and unlatching
- Thermal actuators
- Electrical contacts
- Packaging

Each element must be integrated and matured such that the overall component can be successfully deployed. In the sections below, we describe FY07 activities conducted in order to develop and mature each of these key elements. To move beyond TRL 4, the key idea is to exercise and test key elements and features in relevant environments. Specific environmental levels and testing details are described in subsequent chapters.

1.3.4 Threshold and Functionality Testing – Laboratory Environments

In FY06, a limited number of devices were shock tested [1]. In order to firmly establish the shock levels and pulse widths associated with switch closure and to acquire additional data demonstrating the key shock detection features of the MEMS passive shock switch, it was necessary to shock test as many packages as budget and time would allow in FY07. Initially, it was decided that 60 die would be packaged for testing. This is approximately 6 times the number used in FY06.

For verifying basic functionality, shock tests were conducted on a shock table at room temperature. Prior to conducting the shock tests, each device on a die was toggled between open and closed to verify functionality of the thermal actuators and contact closure. After shock testing, the switch state was verified and the contacts were again toggled to verify continuing functionality of the thermal actuators.

1.3.5 Functionality Testing in Relevant Environments

In the subsections below, we discuss the key elements of the MEMS passive shock sensor with emphasis on testing in relevant environments.

1.3.5.1 Spring Flexures (Latching and Unlatching) and Environments

In FY06, a set of compliant spring flexures with a mass attached were developed and demonstrated to be bi-stable and capable of responding to inertial environments. In FY07, our goal was to explore and identify the functional behavior (latching and unlatching) of the bi-stable compliant mechanisms both during and after exposure to thermal and vibration environments. The latch hold capability was exercised by exposing the closed shock switch to random vibration environments (normal environmental spectra). The purpose of this testing was to demonstrate that the latching shock sensor would remain closed and that the latching feature was sufficient to keep the switch closed during and after exposure to normal environments. In addition, our goal was to demonstrate over-shock levels that the mass/spring system was capable of withstanding without fracture or failure.

1.3.5.2 Thermal Actuators and Environments

Validation testing conducted in FY06 was enhanced by the capability to open and close the shock switch contacts. From the EE program prospective, this capability is considered to be fundamental. While it does not provide a complete inertial self-test, a functional contact open and close capability does indicate that the electrical contacts can be open and closed and that the switch is not frozen in place. This functionality depends upon the thermal actuators [4]. In FY07, our goal was to demonstrate that the thermal actuators would remain functional after exposure to thermal, vibration, and over-shock environments.

1.3.5.3 Packaging and Environments

Packaging integrates the key elements of the MEMS shock sensor but is also a bona fide key element in its own right, although not in the same way as thermal actuators or spring and mass elements. Packaging is an external key element that requires customer consideration. Packaging is simply the mechanism or interface by which the customer gains access to the desired functionality. The package design must reflect the customer's need to integrate the sensor quickly and easily both mechanically and electrically. The package must also integrate the key elements of the shock sensor technology in order that expected environmental conditions do not adversely affect proper functioning of the sensor. In FY06, in order to demonstrate an integrated solution at the technology level, a ceramic package was chosen without regard to customer integration and relevant environments. A fundamental goal for FY07 was to develop additional packaging solutions, allowing for a broader range of potential integration scenarios while at the same time making considerations for thermal, vibration, and over-shock environments.

2. BASIC CONCEPTS FOR CUSTOMER INTEGRATION

2.1 Introduction

In order to successfully integrate the MEMS passive shock sensor within a system, consideration should be given to the following:

- Sense axis: die latching direction and impinging shock direction
- Methods for attach
- Expected shock magnitude and pulse width
- Electrical integration: multiplexing for addressing multiple devices in a package, connectors, power requirements

This chapter provides information and examples on integrating the MEMS passive shock switch into a larger system, including electrical and mechanical interfacing considerations as well as basic terminologies used to describe switch functionality.

2.2 Terminology and Functionality

2.2.1 Terminology

2.2.1.1 Sense Axis, Die Latching Direction, Nominal Impinging Shock Direction

The MEMS passive shock sensor is designed to detect shock along a particular direction or sense axis. This makes it necessary to orient and attach the packaged switch within to best facilitate shock detection. Each packaged switch has a designated "die latching direction" which should always be oriented in opposition to the expected "nominal impinging shock direction" as indicated in Figure 2-1. The "die latching direction" depends upon how the MEMS die is oriented relative to the overall packaged switch and is a function of packaging. The "nominal impinging shock direction" depends upon the placement of the shock switch within the larger system.

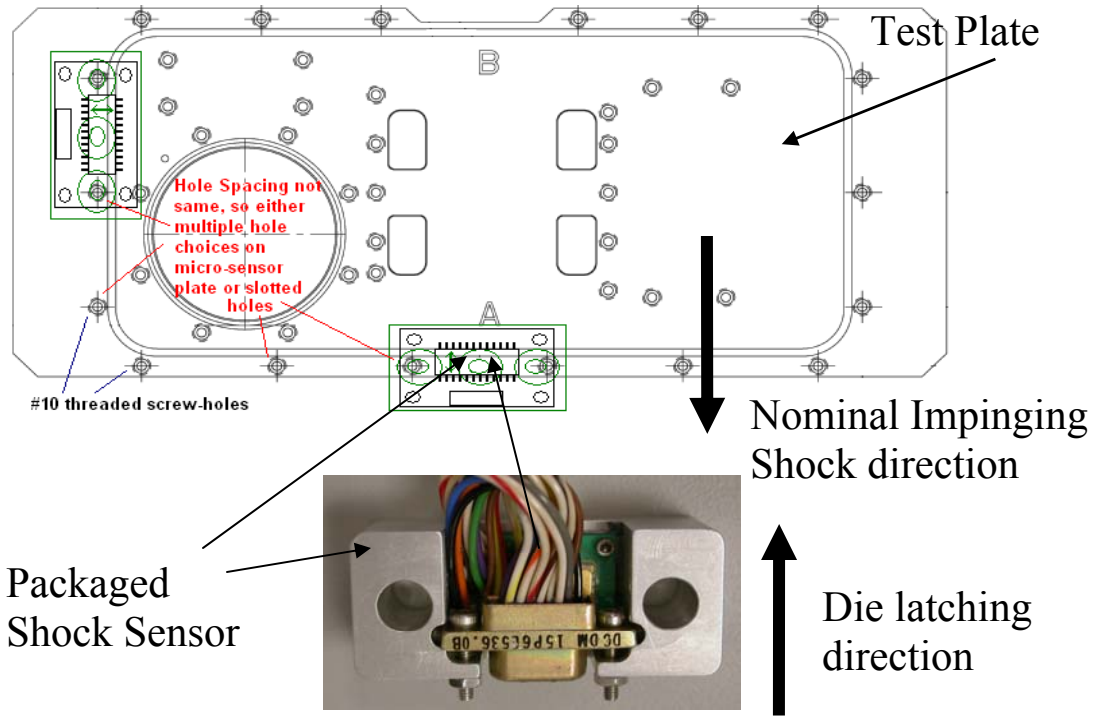

Figure 2-1. Sense axis schematic.

2.2.1.2 Contacts

The shock switch has a set of electrical contacts that may be in the open or closed position. A continuity check is used to detect switch state (open or closed). Table 2-1 below provides electrical contact resistances for the open and closed conditions.

Table 2-1. Electrical Contacts Resistance

State	Contact Resistance
Open	**Greater than a mega-ohm**
Closed	**50 to 100 ohms**

In the open position, metal contact surfaces are separated by approximately 6 to 7 microns which yields greater than a mega-ohm of isolation. In the closed position, two platinum covered surfaces come together yielding a circuit resistance of 50 to 100 ohms.

2.2.1.3 Thermal Actuators

The MEMS passive shock sensor uses thermal actuators to open and close the electrical contacts. A small pulse of power (on the order of 500 milliwatts for 10 milliseconds) is applied to the thermal actuators. Current flowing through slender silicon beams of the thermal actuator causes the beams to expand, thereby closing or opening the electrical contacts. For details on the design and functioning of the thermal actuators, see Baker et al. [4]. Specific power requirements for Revision 2 of the MEMS passive shock sensor are given in Table 2-2.

Table 2-2. Revision 2 Power Requirements—Opening and Closing the Contacts

Applied Voltage	Current Limit	Duration of applied power
9 volts	**50 milliamps**	**10 millisecond**

2.2.1.4 Shock Magnitude and Pulse Width

The MEMS passive shock sensor is designed to detect shock. It is particularly important to know the magnitude (gees) and pulse width (duration of shock) of shock that the switch will detect so that it may be correlated with end-user needs. For purposes of characterizing the response of the shock switch, we describe the shock event as a haversine with a given magnitude and pulse width as shown in Figure 2-2 below. The magnitude versus time curve of the input shock haversine is shown in red and the switch response is shown in blue. The collection of all shock inputs that close the switch contacts characterizes the switch. An example is shown in Figure 2-3 where the blue line with "x" marks indicates the combination of magnitude and pulse width that closes the switch. Any combination of magnitude and pulse width above the blue line (within reason) will close the switch. Technical details associated with generating Figure 2-2 and Figure 2-3 are described in section 5.3.1 of this report.

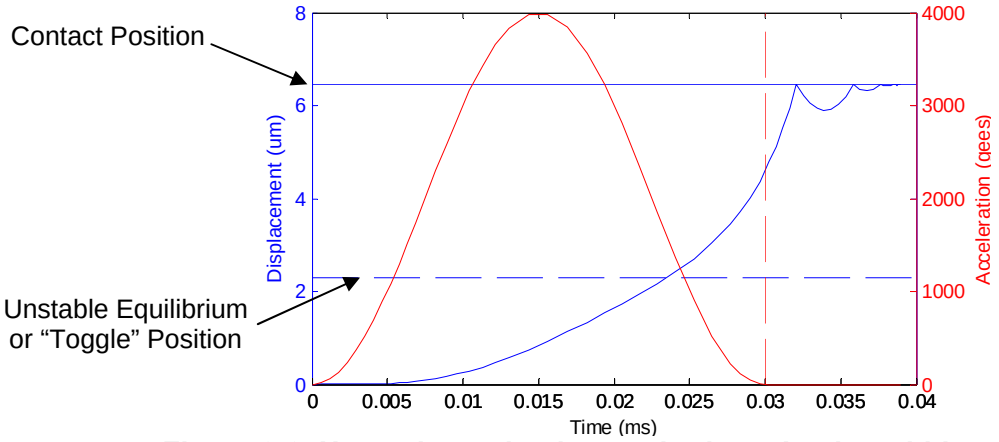

Figure 2-2. Haversine—shock magnitude and pulse width.

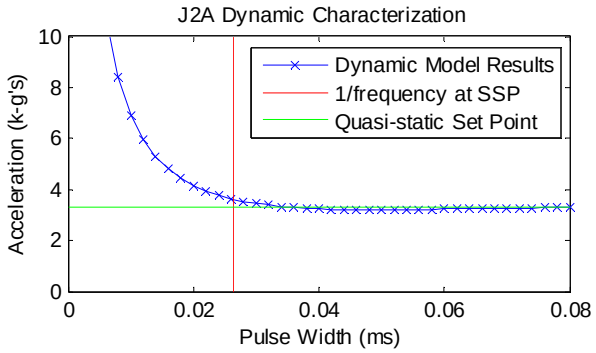

Figure 2-3. Detecting shock—example frequency response and bandwidth of MEMS passive shock sensor.

2.2.2 Overview of Functionality

The MEMS passive shock sensor is a switch designed to passively detect shock. It's described as passive because power is required only to open or close the switch or detect switch state; it will remain latched in the open or closed position indefinitely without a power supply. To detect shock, the switch should be in the open position, i.e., contacts are open. When shock is detected, electrical contacts on the MEMS die are closed. A resistivity/continuity check is used for sensing the switch state which may be either open or closed. Latching is implemented using an elastic bi-stable mechanism described in a subsequent chapter of this report. An important feature of the switch is the ability to open and close the switch electrically with a small pulse of power. The latching/unlatching feature is important for systems that require built-in test capabilities; the open/close feature of the switch can be used to demonstrate that the basic functionality of the switch is working and that the surrounding system which implements the continuity check is functional.

2.3 Mechanical and Electrical Interfaces

Methods for attach and electrical integration requirements are important considerations for an end-user. These concepts are introduced here briefly while details are provided in the packaging chapter of this report (see Section 8).

It is possible that nearly every application or end-user customer will require a slightly different implementation. In this section, we briefly review some of the concepts that were implemented in FY07.

2.3.1 Ceramic Dip

In this approach, the MEMS die is attached, wire bonded, and hermetically sealed inside of a ceramic dip package as shown Figure 2-4. This schematic shows a Revision 1 die that is placed inside of a ceramic dip package. The ceramic dip and wires addressing the individual devices on the die are soldered onto a printed circuit board (PCB) that is subsequently attached inside of an aluminum housing. Later, the interior volume of the aluminum housing is potted. Potting shock hardens the ceramic dip and wires in place. The aluminum box is then placed, oriented, and bolted down according to the appropriate sense axis.

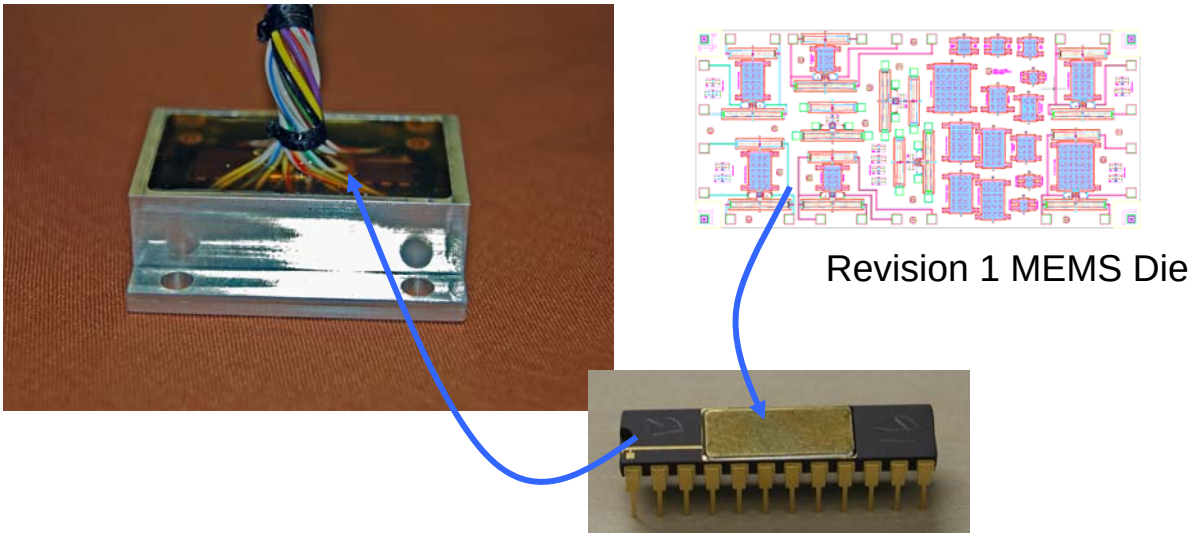

Figure 2-4. Methods for attach—ceramic dip.

2.3.2 Leadless Chip Carrier

The MEMS die is attached, wire bonded, and hermetically sealed inside a leadless chip carrier. The chip carrier is subsequently soldered to a PCB and wires (with a connector at one end) may be soldered to the printed circuit board. This phase of the packaged switch is shown in Figure 2-5 below. At this stage there are still many options for mechanical integration. Figure 2-1 shows an example consisting of a simple aluminum housing that may be bolted down and oriented within the system. The aluminum housing integrates the PCB/chip carrier and 15-pin electrical connector.

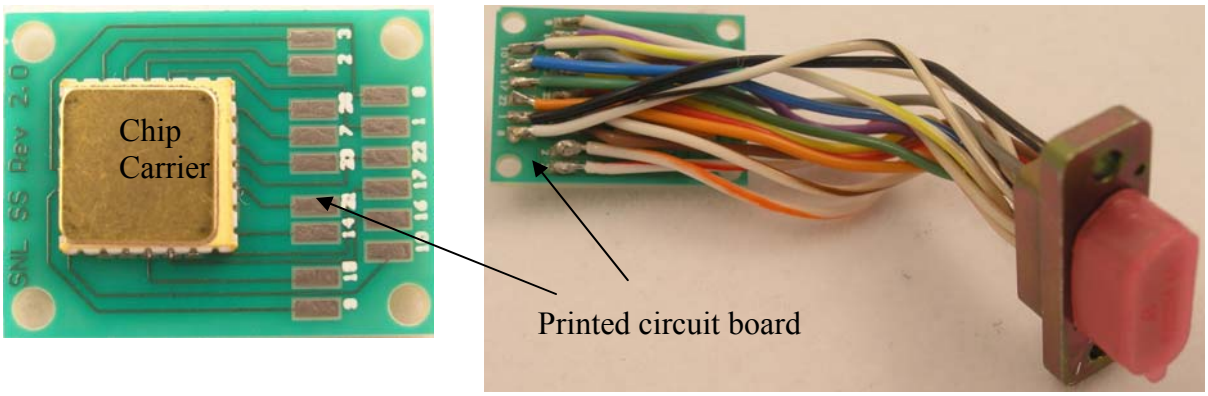

Figure 2-5. Leadless chip carrier on printed circuit board.

2.4 Addressing/Multiplexing Multiple Devices on a Revision 2 Die

Revision 2 of the MEMS passive shock sensor has 4 devices per die. Each device has dedicated electrical traces that allow for independent state detection and functionality. After packaging, there are four wires associated with each device: ground, contacts, power to open contacts, and power to close contacts. In order to electrically integrate a packaged die within a system, it is necessary to obtain a simple specification that relates the 4 devices on the die with the

appropriate pins or wires used for electrical interfacing. Specific packaging requirements and interfacing are different for every application. For illustrative purposes, the packaging solution shown in Figure 2-5 is used to further explain electrical interfacing.

2.4.1 Leadless Chip Carrier and Wire Bond Layout

This example uses Revision 2 of the shock sensor die and corresponds with a prototype delivered to a potential customer. To fully understand electrical integration requirements it is necessary to touch on some elements of packaging (details are provided in the packaging chapter of this report).

The die is attached inside the well of the leadless chip carrier and a wire bonding machine is used to connect wires from the die bond pads to the chip carrier bond pads. A schematic of this is shown Figure 2-6 below.

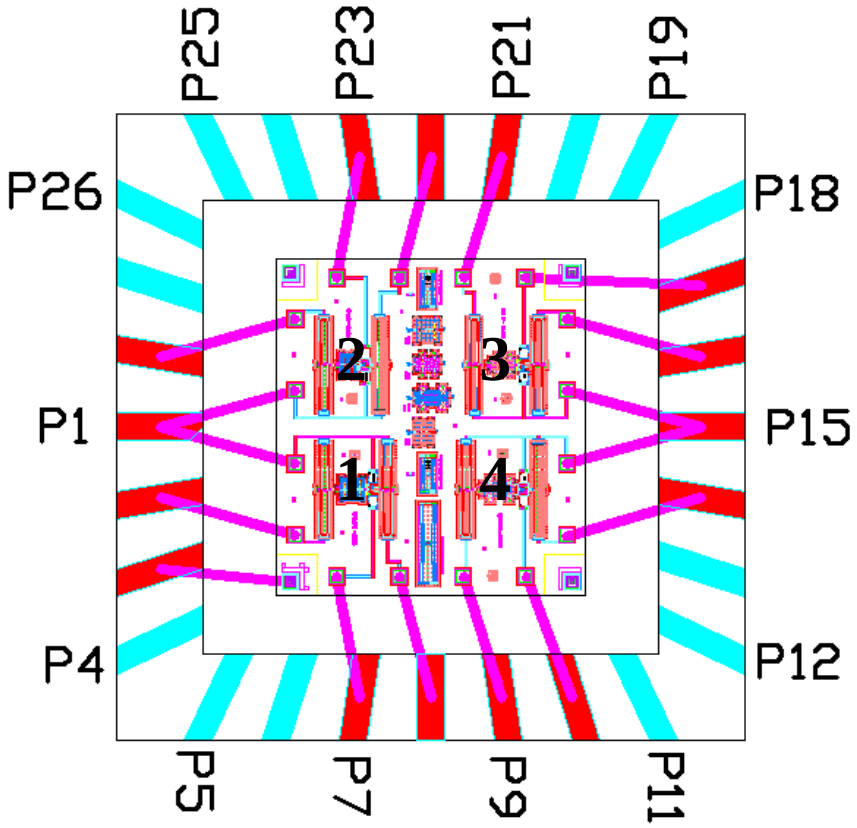

Figure 2-6. EE WETL wire bonding layout.

Wires are shown as thick lines in cyan; devices are labeled 1, 2, 3, and 4; and bond pads are labeled around the perimeter in a counter-clockwise manner. Note that the package has 28 bond pads while only 15 are used. Recall that each device needs 4 wires but one of those is a ground. A common ground was used for devices 1 and 2 as well as for devices 3 and 4. This reduces the overall wire count to 14. One more wire is used for a die-level ground—at the lower left corner of the die a wire is connected to P3. This last wire does not support any functionality.

2.4.2 15 Pin D-Sub Connector

To electrically interface with each device, each pin must be mapped to a particular functionality and device. A fully packaged device is show in Figure 2-1. The device contains a standard 15-pin D-Sub connector with colored wires. The mapping of wire colors, functionality, and pin numbers is given in Table 2-3 (pin numbers are described in Section 2.4.1 and depicted in Figure 2-6).

Table 2-3. Revision 2—Mapping Functionality to 15-Pin D-Sub Connector

Description	Pin #	Connector Color
Open 1	8	BLACK
Contact 1	7	BROWN
Close 1	2	RED
Common 1	1	ORANGE
Common 2	1	ORANGE
Close 2	28	YELLOW
Contact 2	23	GREEN
Open 2	22	BLUE
Close 3	21	VIOLET
Contact 3	17	GREY
Open 3	16	WHITE
Common 3	15	BLACK/WHITE
Common 4	15	BLACK/WHITE
Open 4	14	BROWN/WHITE
Contact 4	10	RED/WHITE
Close 4	9	ORANGE/WHITE

3. DESIGN AND MODELING OF REVISION 2

3.1 Background on Shock Switch Design

This section describes the bi-stable mechanisms used in the MEMS passive shock sensor with a focus on overall design and on how devices are actuated (toggled open and closed). Finally, the section ends with an overview of the final AutoCAD layout for Revision 2.

3.1.1 Bi-stable Mechanisms

A general background on stability and the fundamental behavior governing bi-stable mechanisms has been provided in the FY06 report [1] and in the literature [5]. The micro bi-stable mechanisms used in the shock switches are *fully compliant*, meaning that motion is obtained through the deflection of flexible members and that there are no pin joints or rubbing-sliding surfaces. The *bi-stable* behavior means that they can be in one of two different stable equilibrium positions and remain there without requiring power. Figure 3-1 shows a micro bi-stable mechanism in its first stable position (or as-fabricated position) and in its second stable position.

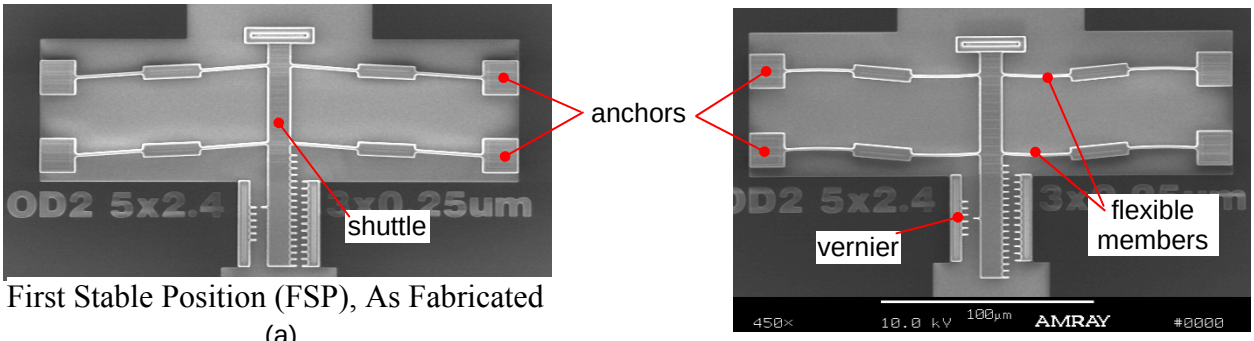

First Stable Position (FSP), As Fabricated
(a)

Second Stable Position (SSP)
(b)

Figure 3-1. A bi-stable mechanism in its (a) first and (b) second stable equilibrium positions.

The mechanism is essentially a proof mass connected to the wafer substrate via a set of parallel springs. The springs are designed to be nonlinear, meaning that the *actuation force*, or the force required to push or hold the proof mass at a specific location, is a nonlinear function of displacement of the mass. Whereas the force vs. displacement relationship for a linear spring is a line, the bi-stable mechanism used here is designed such that the force vs. displacement curve drops below zero at some point along the curve. This results in three locations in which the force is zero (see Figure 3-2): (1) the first stable equilibrium position or fabricated position, (2) the unstable equilibrium position or toggle point, and (3) the second stable equilibrium position.

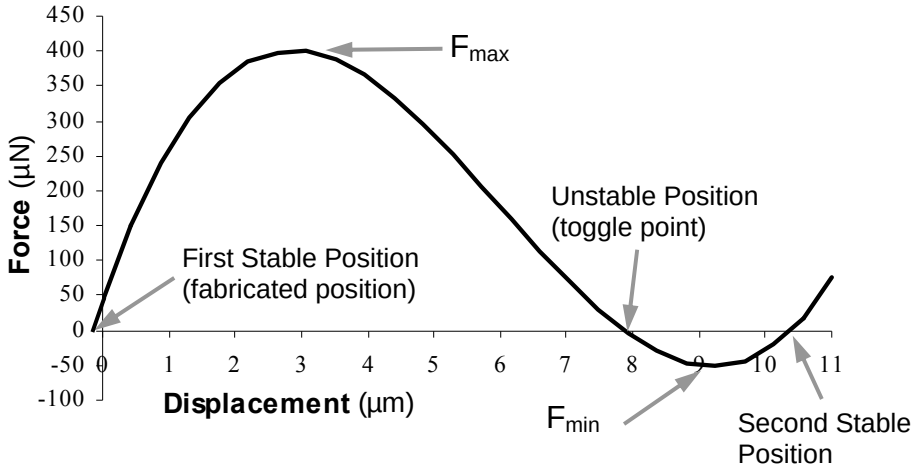

Figure 3-2. Example force vs. displacement curve for a bi-stable mechanism.

For application as a shock switch, the mechanism is designed with a specific mass and target set point such that an acceleration greater than that set point causes the mechanism to toggle from one stable position to the other. For these types of nonlinear springs, it is possible to design the spring such that the magnitude of the minimum force (F_{min}) is much lower than the magnitude of the maximum force (F_{max}). The device then behaves somewhat like a trigger or circuit-breaker mechanism. First, the mechanism is toggled to the second stable position using a thermal actuator. Then, the force required to toggle the mechanism back to the first stable position is the magnitude of F_{min}. The acceleration required to toggle the mechanism is determined from Newton's law, $a = F_{min} / m$, where m is the mass of the shuttle or proof mass.

When the acceleration threshold is met, the mechanism moves un-powered toward the first stable position. Rather than allowing the mechanism to return to its original fabricated (zero-force) position, electrical contacts are placed at the location of F_{max} so that in the closed position there is a contact force of F_{max}.

3.1.2 Shock Switch Layout and Operation

Figure 3-3 shows an example layout of a shock switch, with thermal actuators for opening and closing the switch. It is important to understand that the device is fabricated with the electrical contacts in the unlatched position (see Figure 3-3). The contacts are latched permanently into position with the first use of the open actuator (see Figure 3-4). All subsequent uses of the open actuator simply toggle the position of the mass from the closed to open position.

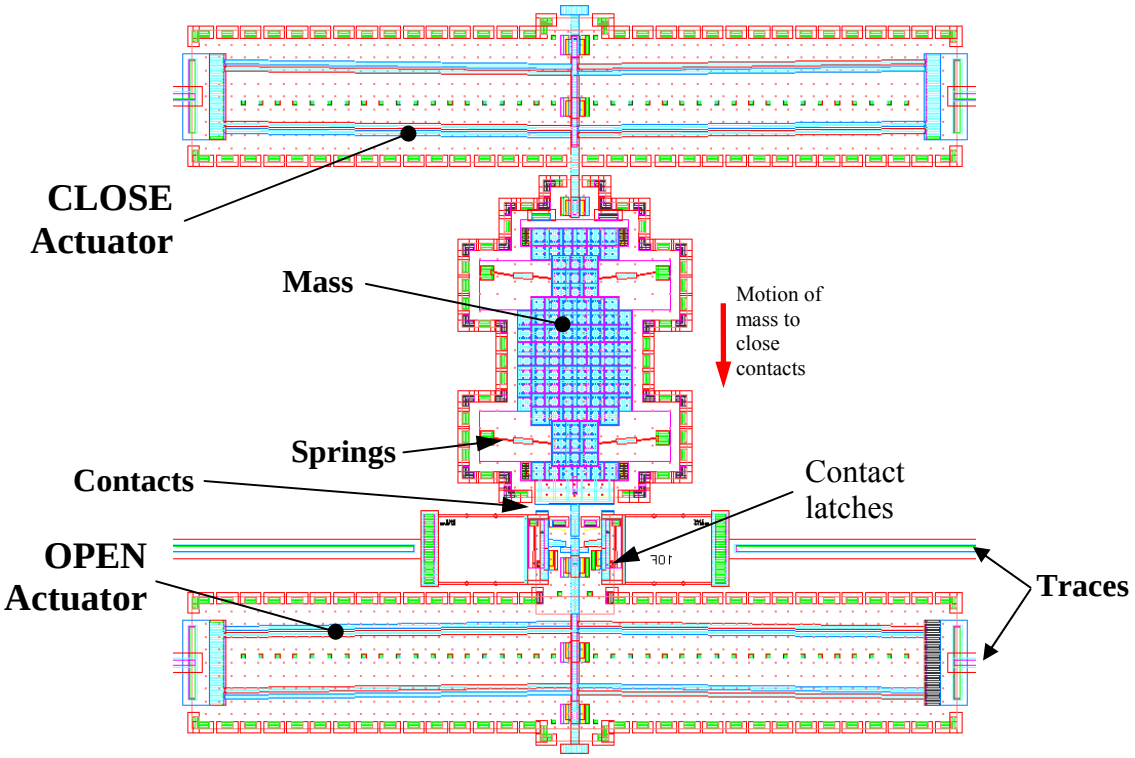

Figure 3-3. Shock switch layout in AutoCAD showing actuators, mass, and contacts.

The CLOSE actuator allows the device to have a self-test feature in which the electrical contacts and bi-stability of the mechanism can be tested without requiring an acceleration input. In operation, the device is meant to remain in the open position until it has seen a shock event over the designed threshold or set point. After closure, the device is meant to remain closed. The device is interrogated by simply measuring whether the contacts have been shorted by the mechanism.

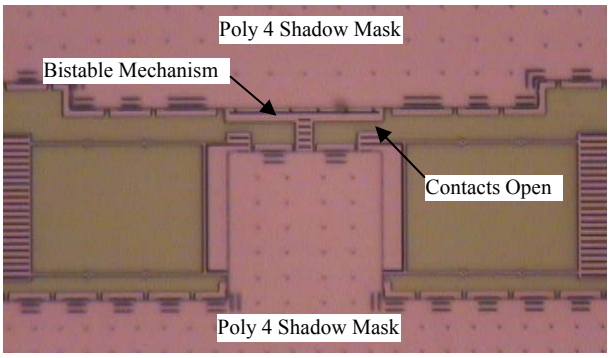

1. Fabricated Position

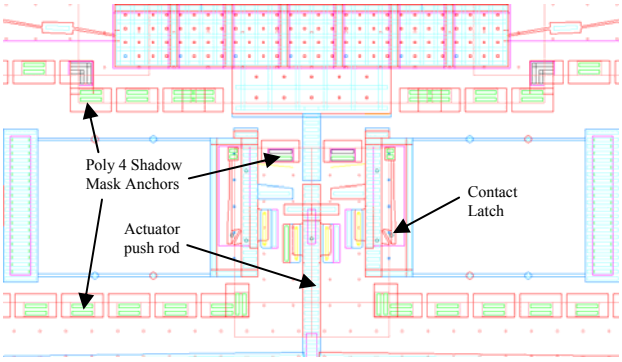

AutoCAD Layout

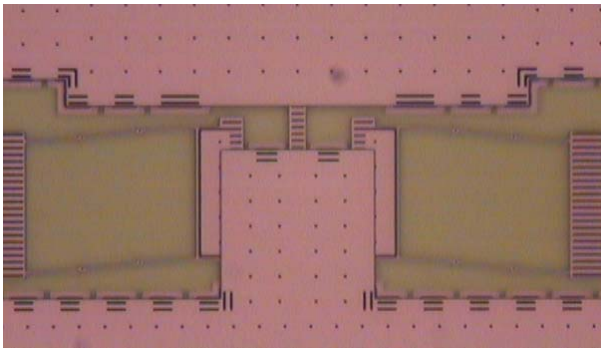

2. Contacts latched, Device open

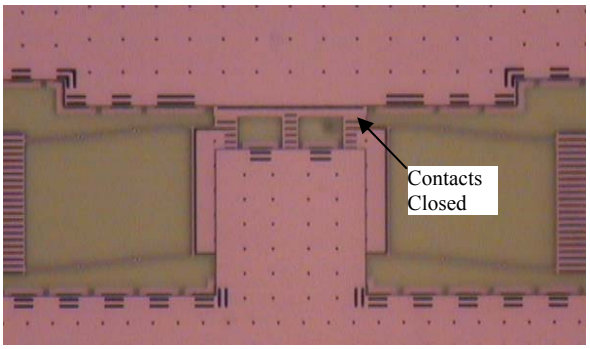

3. Contacts latched, Device closed

Figure 3-4. Contacts in the fabricated, latched/closed, and latched/open positions.

3.1.3 Layout of the Revision 2 Module

Figure 3-5 shows the final design layout for the Revision 2 module. In the remainder of this report, devices will be referred to using the designation J2A, J2B, J2C, J2D, M2A, M2B, M2C, and M2D, where the "2" refers to Revision 2.

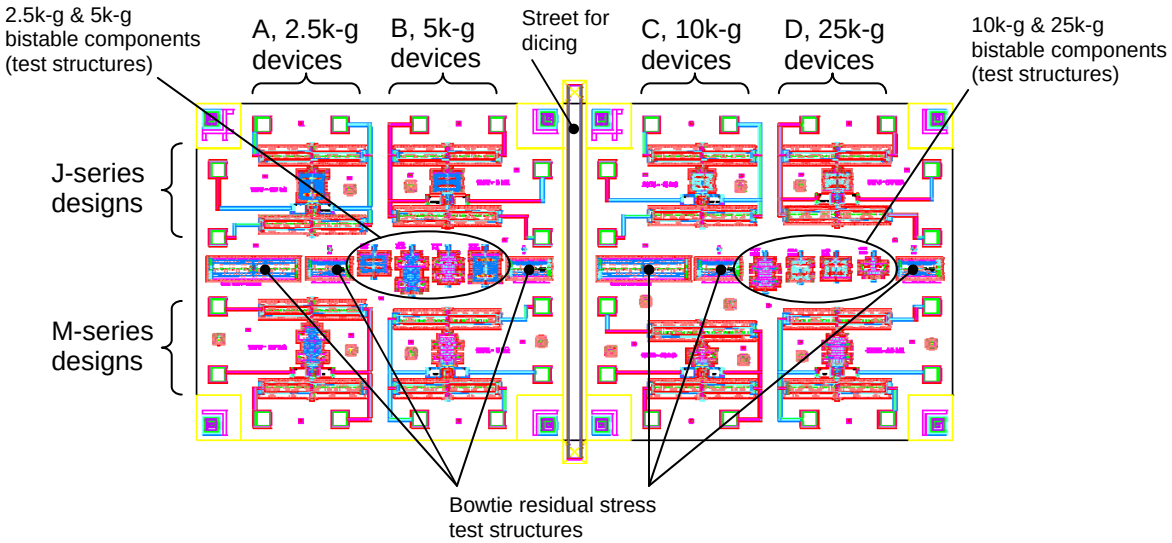

Figure 3-5. Revision 2 final design layout in Reticle Set (RS) 630.

3.2 Motivation for Revision 2 Designs

This section describes device designs for Revision 2 (RS 630) shown in Figure 3-5. It was imperative that Revision 2 reflect and address the lessons learned from Revision 1 (see Section 1.3.1). It was also decided that Revision 2 devices and designs would have higher quasi-static set-points. This section introduces and discusses in some detail design considerations and issues related to Revision 1 lessons learned with an emphasis toward impacting Revision 2.

3.2.1 Sensitivity to Uniform Residual Stress in the Bi-stable Mechanism

In this section, the effects of residual stresses on performance of the bi-stable mechanism are introduced. Residual stresses in the MEMS die can arise from several sources including the Sandia Ultra-planar, Multi-level MEMS Technology 5 (SUMMiT V) [6] fabrication and packaging processes. For purposes of discussion, residual stresses are those stresses that are permanently built into die and or packaged parts due to fabrication and packaging processes. Later, after parts have been fabricated and packaged, changes in temperature may create additional stresses in the die due to coefficient of thermal expansion (CTE) mismatches within the package. For conceptual reasons, stresses induced due to changes in temperature are considered as residual stresses. As a final caveat, it is necessary to mention that creep and stress relaxation effects are not considered although this is thought to be a reasonable approach and assumption for silicon.

The shape of the force versus displacement curve for the bi-stable mechanism can change due to residual stresses in the die. This means that locations of equilibrium positions can change. It also means that force thresholds that cause the switch to toggle from one stable position to the other also change. For this reason, it is very important to consider residual stresses in the design.

Experimental results on Revision 1 designs showed models consistently under-predicting the set point. Further analysis showed that designs were sensitive to residual stress; residual stress was thought to be a likely cause for the discrepancy. Some amount of residual stress is expected after the devices are released due to micro fabrication processes. SUMMiT V consists of multiple layers of polysilicon and sacrificial oxide, and involves many thermal cycles. There is a difference between the CTE of polysilicon and the oxide layers. When devices are released, the sacrificial oxide in the back-side film is not completely removed. This leads to a wafer having some amount of curvature, which ultimately leads to residual stress (normally compressive) in the polysilicon where MEMS devices are located.

It is generally known that packaging processes can induce residual stresses. There was reason to believe the discrepancy between model and experimental results for Revision 1 designs was due in part to residual stress induced through packaging. This effect is more difficult to understand and quantify as it translates to changes in position of device anchors.

Finite element models of the bi-stable mechanism were used to understand and quantify effects of residual stresses. Inputs to the model include a uniform residual stress in the bi-stable mechanism. Using this approach is straightforward, but it does not include effects that are likely to occur such as stress gradients through the thickness due to SUMMiT fabrication. It is also

likely that packaging effects are of a non-uniform nature as well. However, the modeling approach used here for residual stresses highlights some very important features and effects related to the performance of the devices.

Using thought experiments and finite element models, a new design concept for the bi-stable mechanism was developed. This new design reflects a basic understanding of the way uniform residual stress effects can be mitigated. By placing the anchor positions in the middle of the device, a new design for the bi-stable mechanism component was developed that greatly reduces the sensitivity to residual stress. This new design (called the J-series) allows the frame or mass to freely expand due uniform changes in the temperature (thus creating uniform residual stresses). The original designs are called the M-series. Schematics for these two designs are shown in Figure 3-6.

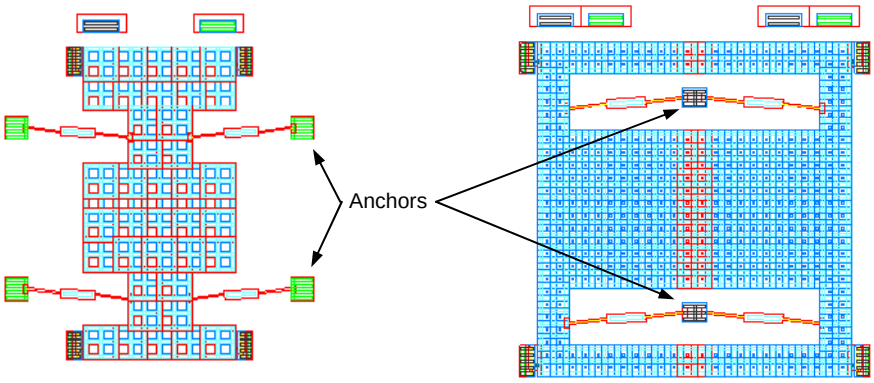

Figure 3-6. (a) M-series and (b) J-series designs showing location of anchors.

Results of a parametric study on the M-series and J-series devices are shown in Figure 3-7. Of particular importance to the design is the actuation force (indicated in the figure by F_{min} = 10 μN). This force changes with residual stress. Depending upon anchor spacing, the simulation shows that the J-series design is about 13 to 27 times less sensitive to uniform residual stress. There is also a difference in the sign of the sensitivity. In the M-series, an increase in residual stress results in an increase in the set point. In the J-series designs, an increase in residual stress results in a decrease in the set point.

To quantify residual stress and help validate models for Revision 2, test structures were added to the Revision 2 die design in order to measure residual stress in the die. A test plan was created that would measure the residual stress after release and then after each major stage in the metallization and packaging process. These tests and results are discussed in Section 9.3.

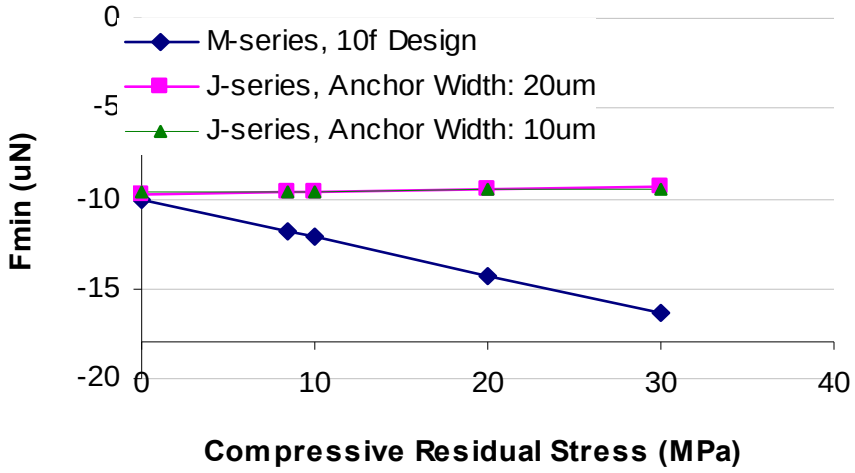

Figure 3-7. Sensitivity to residual stress.

3.2.2 Sticking Parts

Anecdotal evidence was collected in FY06 related to devices that were found dysfunctional. One observation was that after metallization of the die, thermal actuators were found to be stuck down to the substrate. The number of stuck devices was not collected but there was enough evidence to consider this a problem. Often it was possible to manually free the thermal actuator at a MEMS probe station, but this was considered undesirable. The exact cause is unknown. However, because no dimples were used in the Revision 1 design, it was theorized that the thermal actuators were rotating and bending out of plane during or after elevated temperatures of metallization. At some point the push tabs on the thermal actuators were coming into contact with the substrate and upon cooling they remained in contact and stuck. Welding of the push tab to the substrate (with the platinum metal) did not seem to be occurring as it was often possible to manually release the push tab using a probe tip at a MEMS probe station.

To address this problem, dimples were used in the Revision 2 design to limit the amount of out-of-plane displacement of the actuators and the bi-stable mechanisms so that the exposed ends (the contacts and tabs not covered by the Poly 4 metallization lid) could not touch the substrate. In addition, the Poly 4 shadow layers covered more of the thermal actuator push tabs leaving less exposed to metallization.

3.2.3 Off-axis Considerations and Uncertainties

In FY06 it was demonstrated that Revision 1 device designs would close due to off-axis shock inputs. By “off-axis” we mean a direction other than the intended in-plane sense-axis. The principle concern here is to understand the device set point and how that may change due to combined sense-axis and off-axis loading. In practice, devices will experience both in-plane and out-of-plane loading.

Devices are designed using an idealized quasi-static uni-axial inertial load aligned with the sense-axis. Revision 1 designs did not consider inertial environments in which impinging shock

was not perfectly aligned with the sense axis. It is desirable that the set point of the device remain constant even when in the presence of an off-axis acceleration. Through simulation, Revision 1 devices were shown to be somewhat sensitive to off-axis acceleration. In this case, the off-axis acceleration tends to lower the nominal set point of the device in the sense direction. For example, if a 10 k-g device is exposed to a 9 k-g shock in the sense direction and a 9 k-g shock in the out-of-plane direction, the device may close even though the 10 k-g set point was not exceeded.

To reduce off-axis sensitivity, bi-stable mechanisms for Revision 2 were re-optimized. In addition, a new process for "thick-poly" fabrication was developed. Models showed that by increasing the transverse thickness of polysilicon layers an increase in out-of-plane stiffness relative to the in-plane direction could be achieved.

Another new design feature included to combat out-of-plane motion was dimples. Dimples were included both above and below the bi-stable mechanism components to prevent significant out-of-plane motion. It was thought that the dimples may act as bumpers.

3.3 Design of the Bi-stable Mechanisms

Section 3.1.1 described the bi-stable mechanism used in the shock switch. This section provides details on how devices are designed for a specific acceleration set point, and how they are optimized to reduce sensitivity to fabrication variations. A summary of the final design parameters for the springs is provided.

3.3.1 Spring Design: Force vs. Displacement

To review, the bi-stable mechanism component of the shock switch is designed such that the nonlinear spring has a specified minimum force corresponding to the threshold acceleration, or set point. To design a device with a specific set point, i.e., the shuttle inertial mass, the device is sized using $F = ma$, where F is the minimum force F_{min}. Using this approach, designs having different set points can be created by using the same springs with different masses.

Figure 3-8 shows a schematic of one spring or "leg." Note that an actual device has 4 such springs, all of which would be attached to an inertial mass. When designing a bi-stable mechanism for a specific force level, the lengths, angles, and widths of spring segments can be modified. The thicknesses of the layers and the material properties are determined by the fabrication process. For a given spring design, the mass can be modified to arrive at devices with different quasi-static set points.

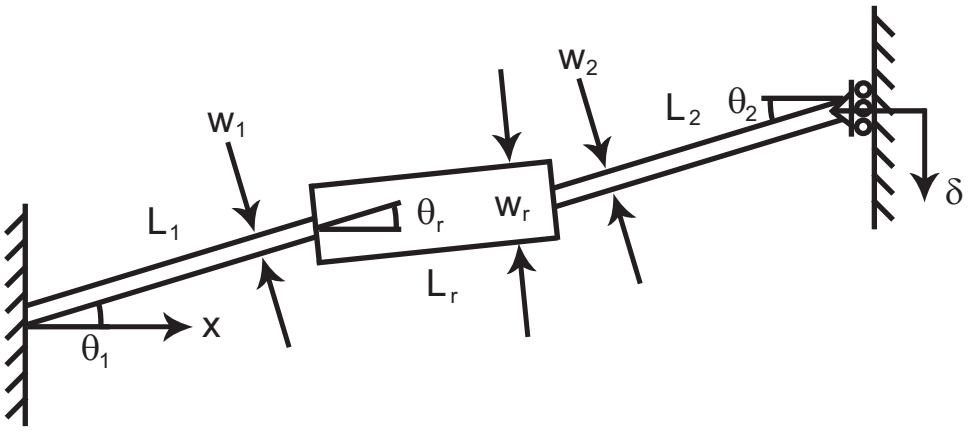

Figure 3-8. Design parameters for the bi-stable mechanisms.

An example of the force vs. displacement curve for one of the devices is shown in Figure 3-9. The figure includes a 95% confidence region for both force and stress. Red and green curves represent two different methods for calculating the confidence region (first- and second-order methods respectively). The pink regions represent uncertainty in the contact and hard stop locations, discussed in Section 3.4. However, at the time these plots were created, the uncertainty in contact position was assumed to be ±0.5μm, or a standard deviation of 0.25 μm (as opposed to 0.17 μm as calculated in Section 3.4).

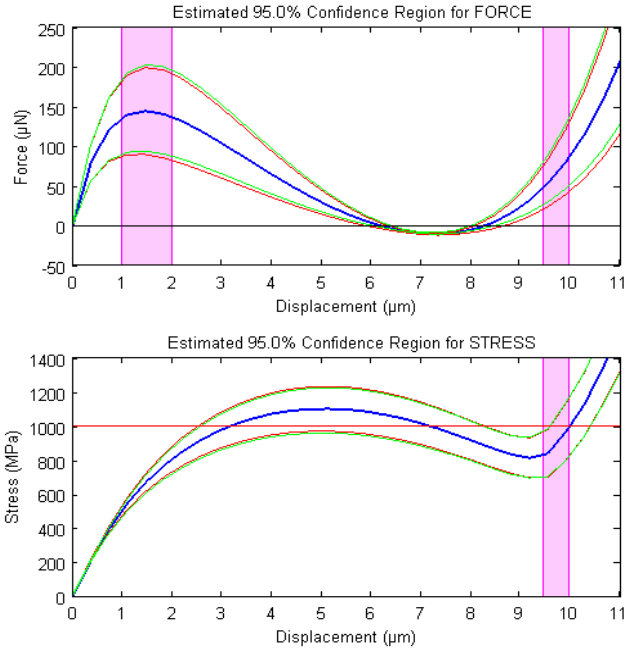

Figure 3-9. Uncertainty analysis of the J2B device.

3.3.2 *Development of Beam Element Model to Account for Out-of-Plane Stiffness*

To evaluate the sensitivity to off-axis loading and uniform residual stresses, new models were created that included the ability to handle out-of-plane loading and motion. To accurately model out-of-plane stiffness of the springs, a combination of beam elements and rigid link elements were used for Poly2 and Poly3 layers. Figure 3-10 shows a 3D view of the spring geometry (a) and the corresponding beam finite element model (b).

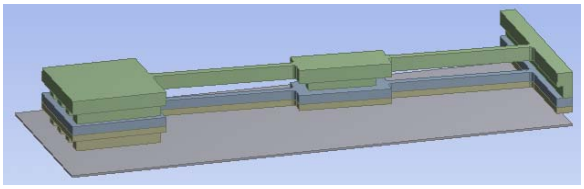

(a) 3D CAD model showing 1 of 4 legs

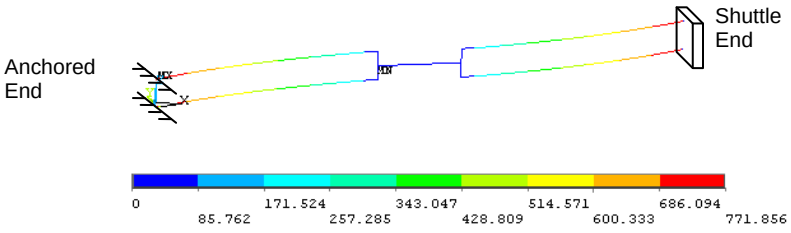

(b) Beam-element model showing stress distribution

Figure 3-10. (a) CAD and (b) finite element model of the springs for the bi-stable mechanism.

In the beam element model, the displacement due to residual stress in the mass can be accounted for by imposing a displacement boundary condition on the shuttle end that corresponds with the change in width of the shuttle due to residual stress and/or thermal stress. The approximation is that the shuttle is infinitely stiff compared to the flexible beams. An out-of-plane acceleration load can be applied to this model by using a symmetry condition at the shuttle end and adding mass elements to the shuttle end to account for ¼ of the inertial force carried by each spring.

The J-series devices required a new model. Although a first-pass at the spring design can be obtained using the beam element model above, the J-series devices must include frame stiffness. It was found that using beam elements to model both the springs and frame was not sufficient to obtain the needed accuracy. A 2D model was created that included holes in the frame as shown in Figure 3-11. This model requires a relatively fine mesh to obtain accurate results. The mesh shown would be considered a coarse mesh.

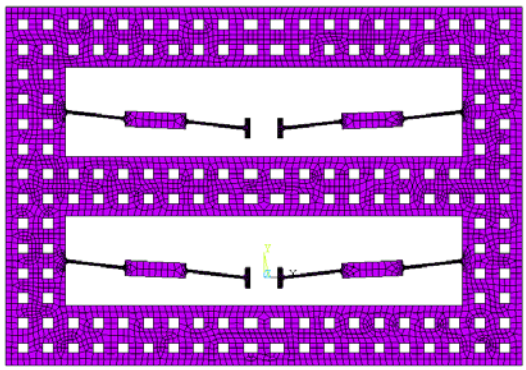

Figure 3-11. 2D model of the J-series device.

3.3.3 Optimization of Revision 2 Designs

Because the mass is fairly straight forward to calculate and design, optimization of the shock switch consists mostly of designing the nonlinear springs. The design, analysis, and optimization of these types of bi-stable mechanisms have been described in the literature ([7], [5]) as well as in the previous 2006 report [1]. Normally, the objective function is to minimize uncertainty in the minimum force while simultaneously targeting a specific minimum force or set point. Also, a number of design constraints relate to the capabilities of the thermal actuators, the stresses in beams, and the SUMMiT V or other processing design rules such as minimum line widths.

For the Revision 2 designs, additional objectives and constraints were included to achieve higher out-of-plane stiffness. A robust optimization technique (see [5]) was used to minimize sensitivity of critical performance parameters to edge bias variation. Some reliability-based constraints were also included. The objective function and constraints are summarized below.

3.3.3.1 Algorithm

The robust optimization of spring designs was performed using the MATLAB Optimization Toolbox, a nested uncertainty analysis algorithm, and a custom MATLAB function that would run the ANSYS Finite Element Analysis (FEA) model (see Figure 3-12). For each evaluation of the model, the MATLAB function would (1) create an input file defining the current set of values for design and uncertainty variables (2) run the analysis using ANSYS, and (3) post-process the ANSYS output to return response values.

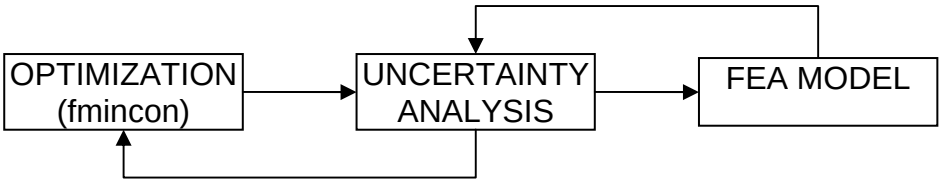

Figure 3-12. Schematic showing nested optimization algorithm.

3.3.3.2 Objective

The objective function for the optimization algorithm consists of three weighted objectives:

- Minimize uncertainty in F_{min}, (σ/F_{min}) weight: 3
- Minimize sensitivity to off axis load weight: 1
- Minimize $(F_{target}-F_{min})^2$ to hit target weight: 6

As shown in Figure 3-12 above, the optimization function calls a nested uncertainty analysis function. The uncertainty analysis algorithm is a mean-value first-order second-moment method in which gradients are numerically determined using forward difference derivative calculations.

The uncertainty analysis consists of calling the FEA model four times. The first call evaluates the device at nominal parameter levels. The second and third calls are used for the uncertainty analysis. The two uncertain variables are (1) edge bias and (2) residual stress.

To evaluate off-axis load sensitivity, the fourth call to the FEA model evaluates the response with an added off-axis acceleration load equal to 10 times the nominal set point. For example, let F_o be the nominal value of F_{min} determined from the first function call. The off-axis acceleration in the fourth call would be $10F_o/m$, where m is the mass of the shuttle. Let F_z be the value for F_{min} determined from the fourth call. Off-axis acceleration causes the magnitude of F_{min} to decrease. The objective is to minimize $(F_z/F_o\text{-}1)^2$, so that as the ratio F_z/F_o approaches 1, sensitivity to off-axes acceleration decreases.

3.3.3.3 Design Variables

The design variables and their bounds are listed in Table 3-1. The variable names correspond to those shown in Figure 3-8 (Section 3.3.1). Note that a simplified notation has been used to show equality of subscripted parameters, i.e., $L_{1,2} = L_1 = L_2$.

Table 3-1. Design Variables Used for Optimization

Variable	min	max
$L_{1,2}$ (μm)	5	75
$\theta_{1,2}$ (deg)	0.1	10
$w_{1,2}$ (μm)	1	2.5
L_r (μm)	10	100
θ_r (deg)	0.1	10

3.3.3.4 Constraints

In addition to the constraints associated with the bounds on the input variables, the optimization algorithm includes a number of reliability-based constraints based on various response variables. The constraints for the 4 different responses are listed below.

1. Stress: $S_{max}+2\sigma < 1200$ MPa
2. Force Ratio: $(F_{min}/F_{max}) + 2\sigma < 0.2$
3. Second Stable Position: SSP$+2\sigma < 12$ μm
4. Unstable Equilibrium Position (UEP): UEP$+2\sigma > 3$ μm

In each of these cases, the sigma (σ) is the standard deviation of the response as determined from the uncertainty analysis.

The force ratio is important because it is desirable that the acceleration required to overcome the contact force (F_{max}) is much greater than the acceleration required to close the contacts (F_{min}). A

constraint of 0.2 means F_{max} should be at least 5 times greater than the magnitude of F_{min} (the inverse of 0.2). Constraints on the second stable position and unstable position were based on actuator capabilities. The actuators are displacement limited.

3.3.4 Global Optimization

In the course of this project, many sets of springs have been designed with different set points. It is anticipated that future work will also involve new spring designs, tailored to specific acceleration levels. Because the design space is highly nonlinear, the search for global optima was implemented using a number of random starting locations for input parameters.

One issue with the design space is that there are pockets of designs in which the springs exhibit buckling behavior, leading to discontinuities in the force vs. displacement curve. These cases usually lead to convergence problems in the analysis. Therefore, the optimization and uncertainty analysis algorithms must be able to handle these convergence failures. To understand the design space better, and possibly find better starting values for the optimization routine, an extensive study was conducted to explore the design space.

3.3.4.1 Design Space

Figure 3-13 shows the bounds used for the design space. Also shown are the 2000 points generated using Latin Hypercube Sampling (LHS). The LHS algorithm was used because it's an efficient space-filling method and fairly easy to implement using available MATLAB functions.

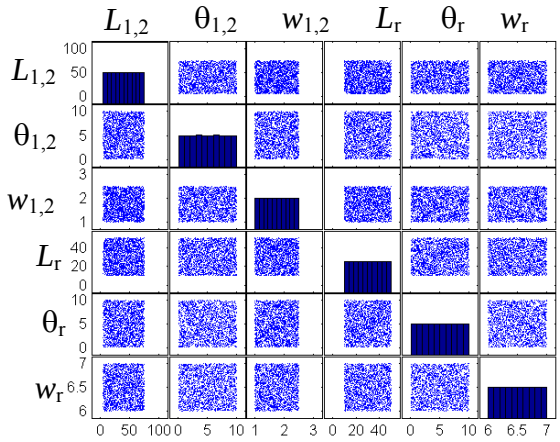

Variable	min	max
$L_{1,2}$ (μm)	5	75
$\theta_{1,2}$ (deg)	0.1	10
$w_{1,2}$ (μm)	1	2.5
L_r (μm)	10	50
θ_r (deg)	0.1	10
w_r (μm)	6	7

Figure 3-13. Design space for exploration study of the bi-stable mechanisms.

3.3.4.2 Unconverged Solutions

Due to time constraints, only 1733 of the original 2000 points were analyzed. Of the 1733 analyses, 411 failed due to convergence problems. Upon a closer inspection and analysis of these designs, it was determined that these failures generally occur when beams exhibit undesirable buckling behavior. Figure 3-14 illustrates an example of a force-displacement curve of a failed design. Note that to get the analysis to converge, the allowable number of equilibrium iterations must be increased (using the NEQIT command in ANSYS). In some cases, it is convenient that devices fail to converge as that provides a means of filtering out bad designs. However, for

optimization, it may be desirable to reduce the number of failures so that the algorithm does not crash when it ventures through undesirable pockets in the design space.

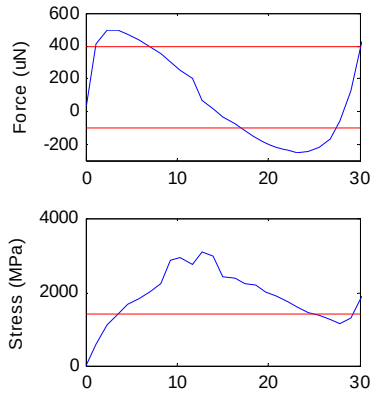

Figure 3-14. Force and stress vs. displacement showing a discontinuity in the force curve.

Unfortunately, there is not a clear location in the design space in which failures always occur. If that were the case, the design space could be adjusted to avoid problematic designs.

3.3.4.3 Response Analysis and Pre-filtering

One of the purposes for performing the design space exploration study was to identify a set of feasible starting locations for the optimization algorithm. Although the sensitivity to off-axis loads was not included as one of the responses in the design space exploration study, the stress, forces, and displacements were included. This allowed the constraints listed above as well as a range for the target force (one of the objectives) to be included in the initial filter.

Figure 3-15 shows a matrix of scatter plots with the response on the *y*-axis and the input variable along the *x*-axis. All of the points *outside* of the pink shaded regions were discarded. Of the original 1322 converged solutions, 156 points survived the filter process. These points were then used as starting values for the optimization of Revision 2 designs.

The process of performing the global optimum was to pick a target minimum force and then run the optimization a number of times using a subset of the 156 filtered starting points. The four target forces used in Revision 2 were: 10 µN, 20 µN, and 50 µN. The 20µN design was used by only one of the J-series devices.

After optimization runs, results were analyzed and the best-of-the-best designs were chosen. In some cases, the optimization converged on designs that were clearly not optimal (due to getting stuck in some local minimum), and these could be discarded. The uncertainty analysis in the optimization used only forward difference derivatives, so the uncertainty analysis at each of the optimum points could be repeated using a more accurate method. Therefore, the choice of the "best" design was based on metrics other than just having the best value for the objective. Some of the other issues to consider were the new calculated uncertainty, the size of the mechanism, and the weighting placed on the individual metrics and constraints.

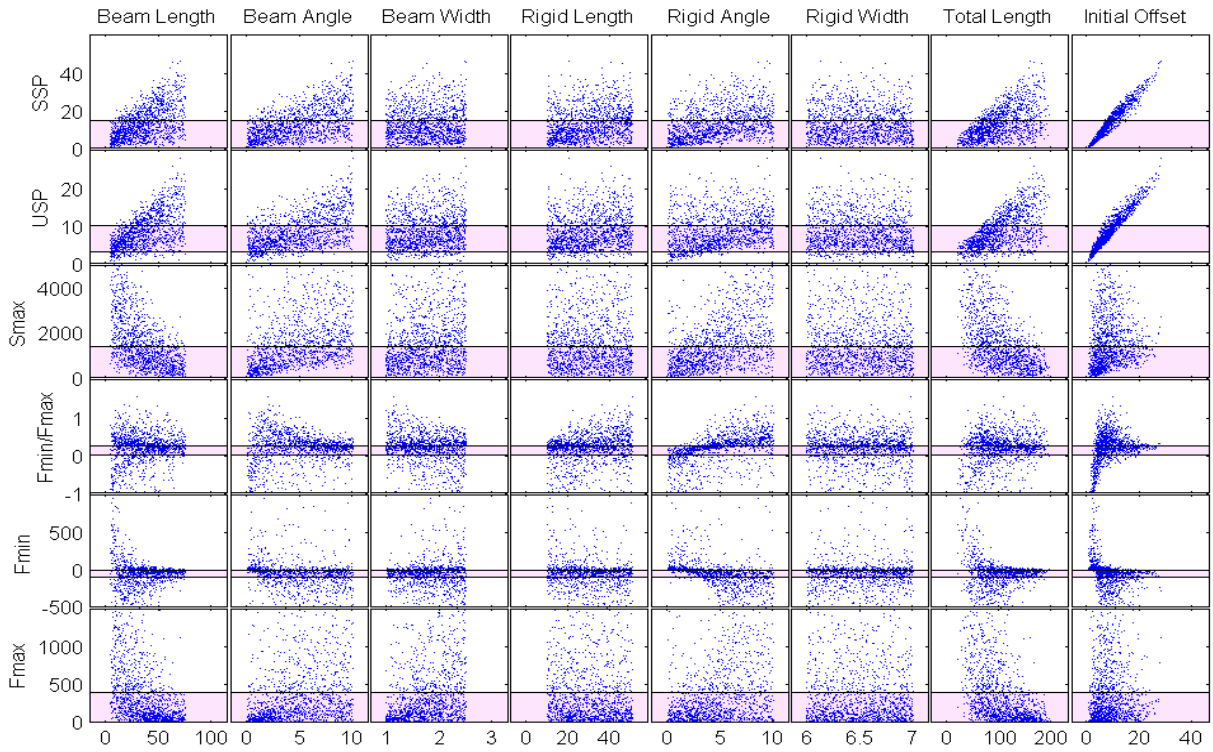

Figure 3-15. Scatter plots of response values vs. design parameters.

3.3.5 Finalized Designs: M-Series and J-Series

This section summarizes final design parameters for Revision 2 shock switches. Table 3-2 provides spring design parameters and Table 3-3 summarizes results from quasi-static analyses. The nomenclature used in these tables is given below.

"set point"	::	The force or the corresponding g-level required to toggle the device closed
"as-drawn"	::	Refers to the dimensions of the device in the layout drawings
F_{min}	::	Minimum force; is equivalent to "set point"
SSP	::	Second Stable Position relative to "as-drawn" position
F_{max}	::	Maximum force
$x(F_{max})$	::	The position of the maximum force relative to the "as-drawn" position
FSP	::	The first stable position relative to the "as-drawn" position
UEP	::	Unstable equilibrium position relative to the "as-drawn" position
S_{max}	::	Maximum stress in the device between the FSP and SSP
zSense	::	Sensitivity of F_{min} to out-of-plane shock where 1 = not sensitive and 0 = non-bistable.

Table 3-2. As-drawn Geometry Parameters (Not Including Edge Bias)

Device	Label on Die	$L_{1,3}$ (μm)	$\theta_{1,3}$ (deg)	$w_{1,3}$ (μm)	L_2 (μm)	θ_2 (deg)
M2A	10FM - 2.5 kG	22.53	6.99	1.16	23.34	2.37
M2B	10FM - 5 kG	22.53	6.99	1.16	23.34	2.37
M2C	10FM - 10 kG	22.53	6.99	1.16	23.34	2.37
M2D	50FM - 25 kG	23.68	3.754	1.21	15.05	4.373
J2A	10FJ - 2.5 kG	23.712	6.83	1.295	24.489	2.49
J2B	10FJ - 5 kG	23.712	6.83	1.295	24.489	2.49
J2C	20FJ - 10 kG	15.675	4.892	1	15	3.262
J2D	50FJ - 25 kG	23.8	3.95	1.36	15.02	4.65

Table 3-3. Summary of Results from Quasi-Static Analysis

Device	Set Point g's	Mass mg	F_{min} μN	SSP μm	F_{max} μN	$x(F_{max})$ μm	FSP μm	UEP μm	S_{max} MPa	zSense
M2A	2486	4.053E-04	-9.89	8.05	111.42	1.29	-0.0534	5.80	1047.2	0.905
M2B	4985	2.022E-04	-9.89	8.05	111.42	1.29	-0.0534	5.80	1047.2	0.904
M2C	9717	1.037E-04	-9.89	8.05	111.42	1.29	-0.0534	5.80	1047.2	0.849
M2D	25694	1.985E-04	-50.03	6.59	200.84	1.15	-0.0603	3.69	995.8	0.339
J2A	3294	4.302E-04	-13.90	8.25	149.31	1.48	-0.0032	5.96	952.2	n/a
J2B	5168	2.105E-04	-10.67	8.14	143.04	1.58	-0.0022	6.12	912.1	n/a
J2C	9933	2.224E-04	-21.67	4.78	138.22	0.95	-0.0007	3.17	877.2	n/a
J2D	22951	2.299E-04	-51.76	6.61	242.36	1.49	-0.0025	4.13	885.9	n/a

3.4 Contact and Hard-stop Positions

It is important to account for edge bias and the thickness of the deposited metal layer when determining how to lay out mask designs for fabrication. It is also important to specify contact and hard-stop locations relative to the as-drawn position. The contact position should be close to $x(F_{\max})$ and the hard stop should be placed such that the device will not break for an acceleration in the reverse direction.

3.4.1 Contact Position

The position of the latched contact relative to the as-fabricated position of the bi-stable mechanism is not a trivial calculation when taking into account the edge bias and metal deposition thickness. The contacts move a distance of 8.2 μm when latched into place. The as-drawn distance between mating surfaces of the latch as measured parallel to the direction of motion is defined as d_{latch} and is shown in Figure 3-16b. d_{gap} is defined to be the as-drawn gap between the contact and the mechanism in the Poly3 layer as shown in Figure 3-16a. The relative contact distance is then calculated using

$$x_{contact} = (d_{latch} - 2p) - (d_{gap} + 2p - 2t_m) \quad (1)$$

where p is the edge bias (nominally 0.1 μm) and t_{m} is the thickness of the metal.

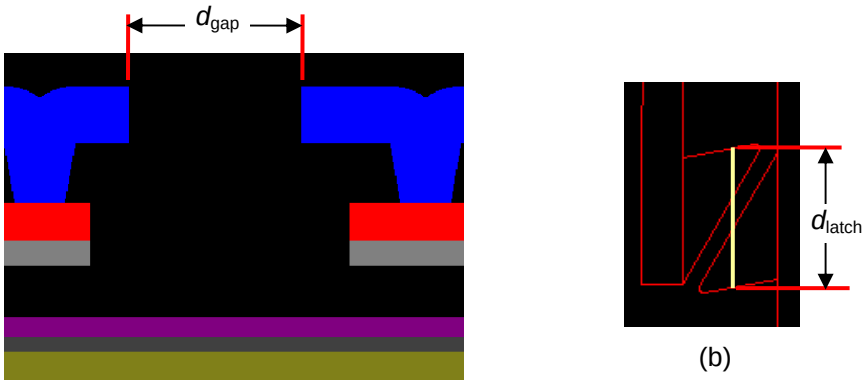

Figure 3-16. (a) Cross section of the as-drawn gap between the contact and the mechanism and (b) the latch distance.

An uncertainty analysis was performed to determine the uncertainty in the contact position given variation in the edge bias and metal thickness. The edge bias was assumed to be a normal distribution with mean 0.1 µm and standard deviation 0.04 µm. The metal thickness was assumed to be a normal distribution with mean 0.15 µm and standard deviation 0.03 µm. A Monte Carlo simulation was run using Equation 1 above, and the uncertainty in the contact position was found to be a standard deviation of 0.17 µm. The contact position for each of the devices is summarized in Table 3-4.

Table 3-4. Position of the Contact and Hard Stops, Taking into Account Edge Bias and Metal Thickness

Device	d_{gap} (um)	d_{latch} (um)	$x_{contact}$ (um)	x_{stop} (um)
M2A	6.9	8.408	1.408	9.7
M2B	6.9	8.408	1.408	9.7
M2C	6.9	8.408	1.408	9.7
M2D	7.1	8.408	1.208	8.2
J2A	6.8	8.408	1.508	9.7
J2B	6.8	8.408	1.508	9.7
J2C	7.4	8.408	0.908	5.95
J2D	6.8	8.408	1.508	7.95

3.4.2 Hard-stop Position

The hard-stop position x_{stop} represents the travel distance of the bi-stable mechanism from the as-drawn position to the point at which the mechanism touches the hard stop. The purpose of the hard stop is only to prevent the mechanism from moving too far in the reverse direction and breaking. The device is not meant to be touching the hard stop when it is at rest in the open position. This is done to prevent stiction or other reliability problems associated with maintaining contact for an extended period of time. The uncertainty in the hard-stop position is a standard deviation of 0.08 µm (twice the standard deviation of the edge bias). The hard-stop position for each of the devices is summarized in Table 3-4.

3.5 Modal Analysis

A modal analysis was performed on each of the bi-stable mechanisms in Revision 2. This was done to determine vibration characteristics of each device and to provide a way to experimentally validate models.

Frequencies of different vibration modes can be used to validate in-plane and out-of-plane stiffnesses predicted by the model. See chapter 0 for a description of modal testing. This report does not contain experimental results for modal testing of Revision 2 devices although model predictions for Revision 1 devices compared very well with experimental results (to within a few percent).

3.5.1 Mass Calculation via 3D Models

To perform an accurate modal analyses that takes into account the actual shape of the mass, the AutoCAD 3D Geometry Modeler was used to convert AutoCAD layouts to .SAT files that were then imported into ANSYS. Before doing this, each of the 8 designs was modified in AutoCAD to take into account edge bias. This involved manually increasing hole sizes by 0.1 μm and reducing beam widths and other external features by 0.1 μm.

Each of the 8 designs was imported into ANSYS Workbench to calculate the total volume of polysilicon. Figure 3-17 shows the 3D models used to calculate the mass. Given a density of 2.33e-15 kg/um^3, the mass was calculated and summarized in Table 3-5. Note that the mass includes the springs and anchors, so the mass values in Table 3-5 are somewhat higher than the nominal effective mass.

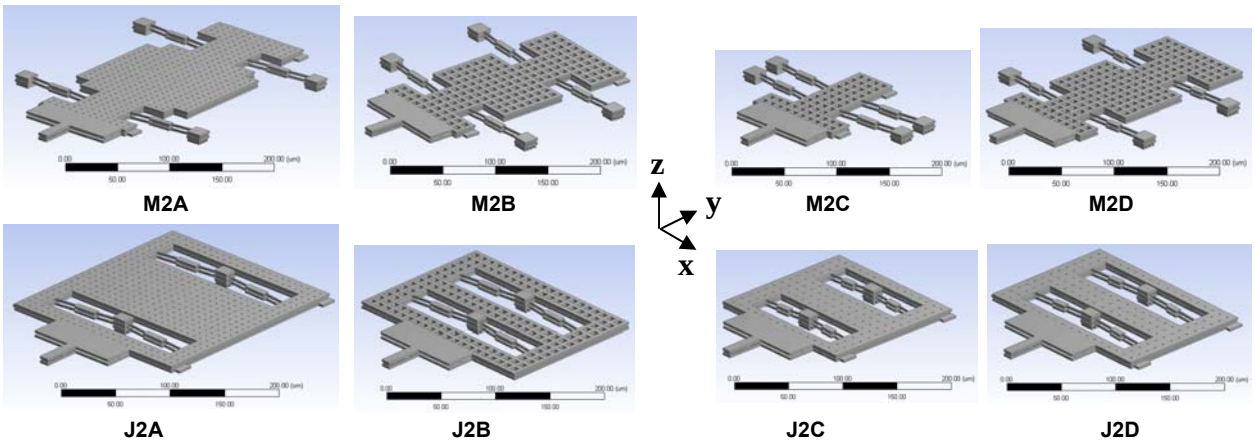

Figure 3-17. 3D models for the 8 different Revision 2 designs.

Table 3-5. Mass Calculations (from 3D Model) for Revision 2 Designs

Device	Mass (mg)
M2A	4.053E-04
M2B	2.022E-04
M2C	1.037E-04
M2D	1.985E-04
J2A	4.302E-04
J2B	2.105E-04
J2C	2.224E-04
J2D	2.299E-04

3.5.2 Modal Analysis Results

Mode shapes and frequencies were calculated at both the first stable position (FSP) and the second stable position (SSP) using a nonlinear pre-stressed analysis. Table 3-6 summarizes Revision 2 device frequencies for in-plane modes. The period was calculated from the frequency and is provided for reference only.

Table 3-6. Summary of In-plane Mode Frequencies Using the 3D Model

	First Stable Pos.		Second Stable Pos.	
	Period	Freq	Period	Freq
Device	(µs)	kHz	(µs)	kHz
M2A	8.1	124 *	25.9	39 *
M2B	5.8	171	18.3	55 *
M2C	4.1	243	12.9	78 *
M2D	5.3	188	9.5	106 *
J2A	7.8	128 *	24.0	42 *
J2B	5.8	172	17.9	56 *
J2C	5.2	193	10.9	92 *
J2D	5.2	192	9.4	106 *

* Evaluated using a coarse mesh

The analysis at the SSP is computationally expensive because the device must first be pushed to its SSP, and then the displacement constraint must be removed so the device can settle to the SSP. A coarse mesh was used for the analysis at the SSP because even with a coarse mesh, it takes about 2 hours per device to solve. For example, running the analysis for device J2B using a finer mesh (6 times the number of nodes) took about 24 hours. The frequency for the in-plane mode was 50.9 kHz (compared to 56 kHz using the coarse mesh).

For the modal analysis at the first stable position (FSP), it was possible to use a finer mesh since the model required only a single pre-stressed solution (to account for the residual stress). Therefore, the model error is much less than 5 kHz.

Mode shapes for M2D device are shown in Figure 3-18. These shapes are characteristic of other devices as well. Table 3-7 summarizes the results for all 8 devices at the second stable position.

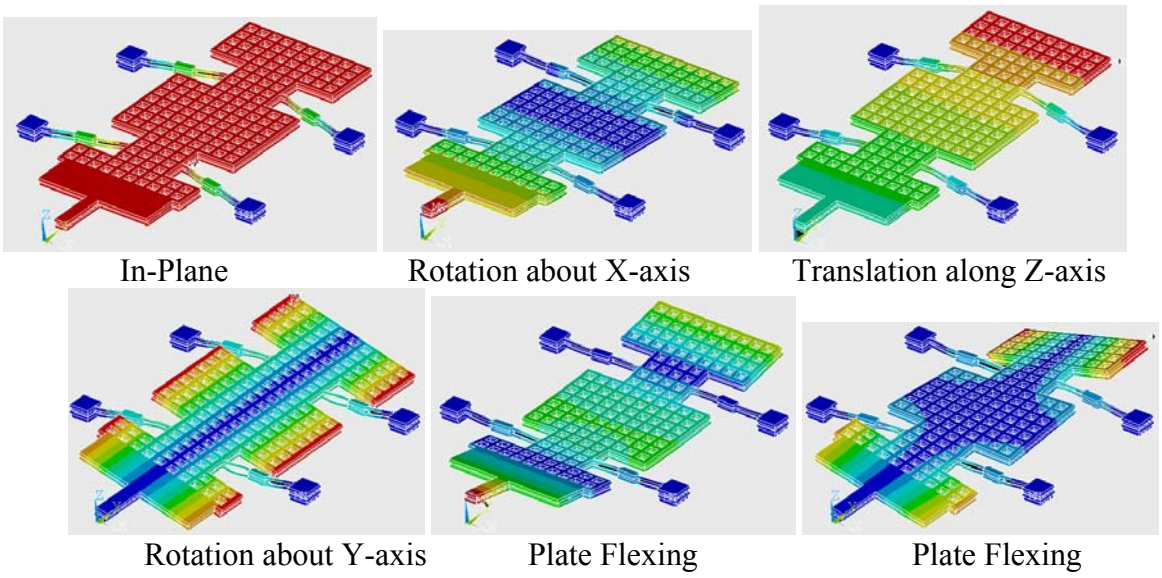

Figure 3-18. First 6 modes at SSP for device M2D, showing the magnitude of the sum of the displacements (blue is zero displacement).

Table 3-7. Modal Analysis at the Second Stable Position (SSP) Using a Coarse Mesh

Frequencies in kHz, Model error roughly 5 kHz

Mode	M2A	M2B	M2C	M2D	J2A	J2B	J2C	J2D
1	38.6	54.7	63.4	105.8	41.6	55.9	92.0	105.8
2	105.5	107.9	77.6	125.9	102.7	80.2	184.6	120.3
3	117.2	152.3	271.6	178.1	105.5	146.0	213.4	159.7
4	230.8	354.0	323.9	391.8	112.7	155.8	274.4	185.9
5	548.9	616.8	544.7	646.8	585.4	385.2	957.0	833.6
6	637.7	639.7	1114.8	828.9	651.7	619.7	1221.9	1101.8
7	709.2	792.5	1116.4	1090.2	760.7	771.9	1307.5	1102.7
8	1115.0	942.8	1119.9	1309.9	828.9	1073.6	1743.0	1568.4
9	1116.5	1114.5	1129.2	1310.3	1254.7	1176.6	2092.3	1626.4
10	1117.3	1115.3	1576.3	1313.7	1256.1	1256.9	2095.4	1629.0

In-Plane
Z-Trans
X-Rotation
Y-Rotation
Z-Rotation
Plate Flex

Typically, the in-plane mode at the FSP was not the lowest frequency mode. However, the analysis at the SSP is more critical because in operation, the device will never actually be at the FSP.

4. MODELING PACKAGING EFFECTS

4.1 Modeling for Thermal Expansion

Differences in the coefficient of thermal expansion (CTE) across the various materials in the packaged device contribute to variations in performance. For example, if the package expands more than the silicon die, the silicon may be placed in a state of tension. In the M-series, if this stress were large enough, the device might self-actuate. J-series designs are less sensitive to residual stress and thermal environments which includes thermal cycles during packaging.

The polysilicon bi-stable mechanism and the silicon substrate to which they are anchored have nearly the same CTE. If the die is allowed to expand or contract freely due to thermal environments then there is no significant change in the force vs. displacement curve. Problems arise when the die is constrained (due to die attach) thereby leading to displacement fields at device anchor locations that are inconsistent with free expansion. In this case, devices are un-naturally constrained leading to residual stresses that are built into each device.

Shock switch simulations which include thermal environments are complicated by the difference in scale between the bi-stable mechanism component and the package. To simulate the effect of thermal environments and packaging on device performance, the mechanism model and the package model are coupled via the relative displacement of anchor locations. See Figure 4-1 below.

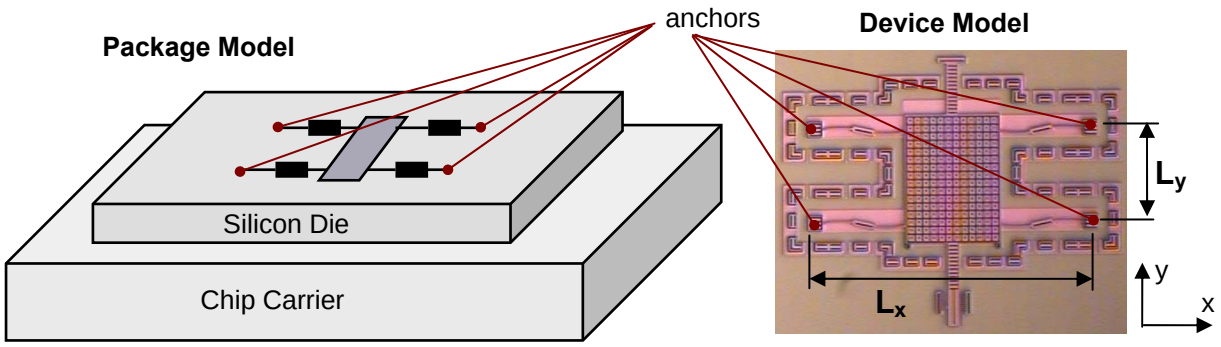

Figure 4-1. Package and device model coupled via anchor displacement (not to scale).

The package model is set up to output the displacement of the top surface of the silicon die. Displacements at anchor locations are then interpolated from these results and input into the bi-stable mechanism model. These displacements lead to a change in L_x and L_y shown in Figure 4-1. The analysis of the mechanism shows that the force vs. displacement curve is not significantly affected by a change in L_y, but a change in L_x is significant for the M-series devices, as shown in Figure 4-2. Results and analysis also show that out-of-plane displacement of anchors on the order of a few nanometers do not have a significant affect on F_{min}.

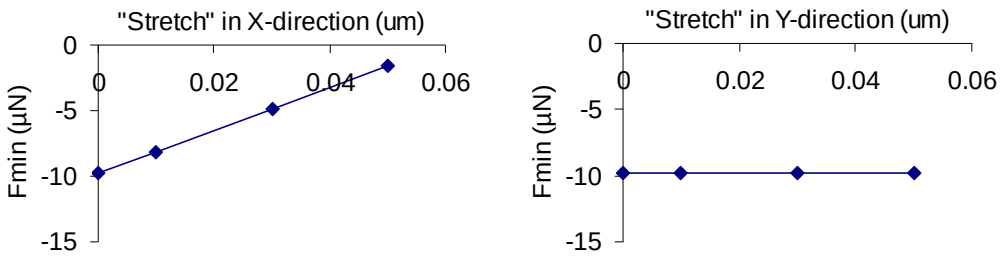

Figure 4-2. Effect of ΔL_x and ΔL_y on F_{min} for the M2B device.

Figure 4-3 conceptually illustrates how to determine ΔL_x. First, symmetry is used to reduce the size of the problem. Then the die is allowed to freely expand due to an increase in temperature. *The unconstrained die represents the expansion of the bi-stable mechanism*. Next, the die is constrained at the bottom surface and heated to the same temperature. Figure 4-4 shows the 3D model used to perform this analysis. The die was heated to 74°C from a reference temperature of 22°C. This is a theoretical constraint used to discuss the effect of a temperature change, where the die is attached to a material with a different CTE.

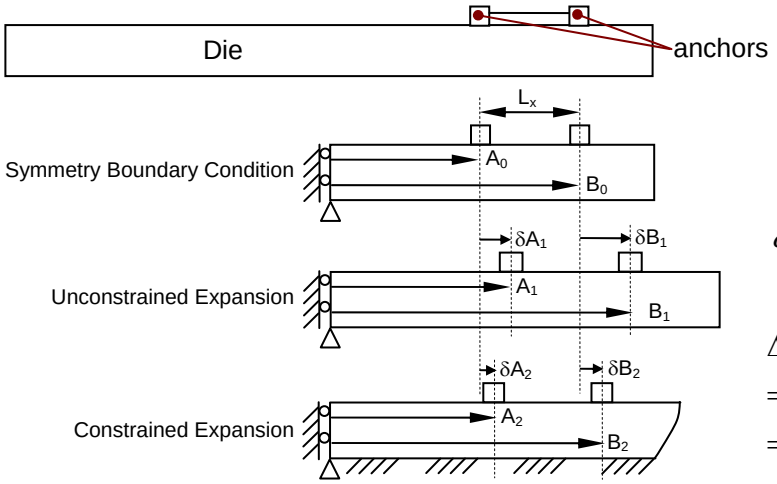

$$\delta X_i = X_i - X_0$$

$$\Delta L_x = L_{x2} - L_{x1}$$
$$= (B_2 - A_2) - (B_1 - A_1)$$
$$= (\delta B_2 - \delta B_1) - (\delta A_2 - \delta A_1)$$

Figure 4-3. Calculating ΔL_x as the difference between constrained expansion and unconstrained expansion.

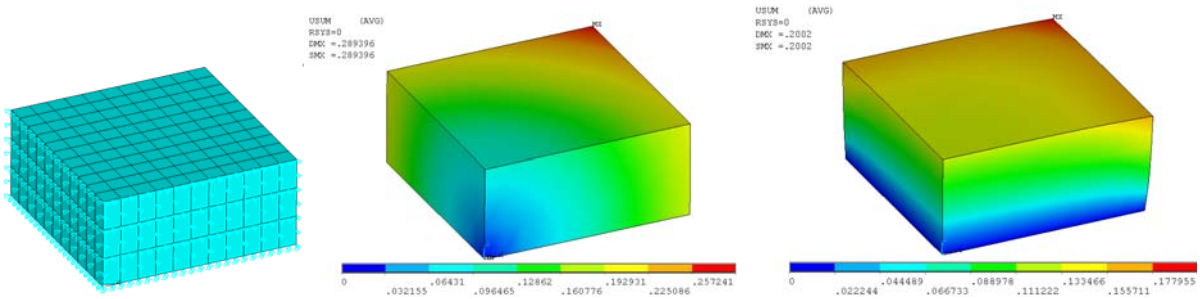

(a) Mesh (b) Unconstrained (c) Constrained

Figure 4-4. Thermal model of a silicon die heated to 74°C (quarter model).

Using the approach shown in Figure 4-3, the difference between the displacement output from the constrained model and the unconstrained model is computed. Then a contour plot is used to determine the optimal placement of the bi-stable mechanism on the die. Figure 4-5 shows the resulting contour plots for differences in *x*-displacement.

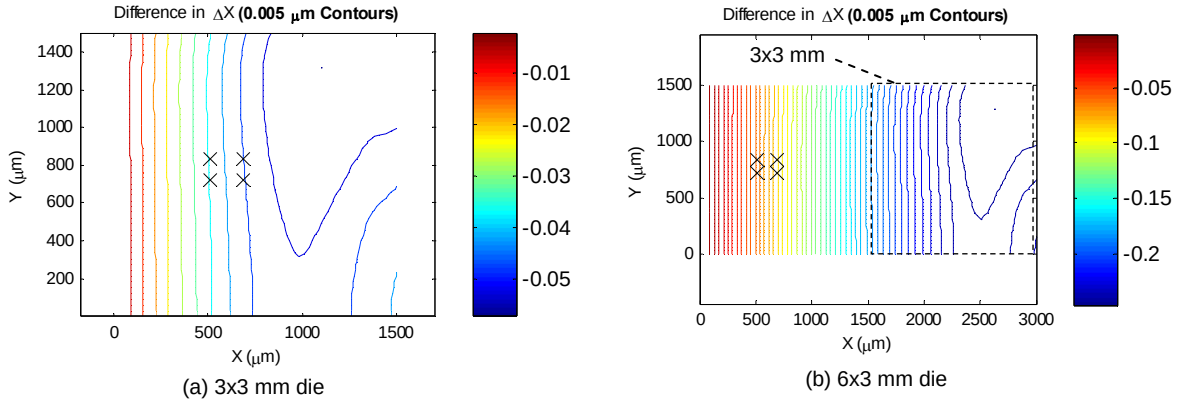

Figure 4-5. Difference in *x*-displacement between constrained and unconstrained die.

The amount anchors are stretched or compressed, ΔL_x, is determined by calculating the difference in the contours between anchor points. It is not good to place devices in an area of high gradient (many contour lines), therefore a large portion of the 3×6 cm die results in poor placement. This analysis provides some justification for using smaller die. If the bi-stable mechanisms were rotated 90°, then it would be important to look at the gradients along the *y*-axis also.

4.1.1 Residual Stress via CTE Mismatch

Packaging involves a number of thermal processes. Die attach using JM7000 epoxy to the leadless chip carrier (LCC) needs a 150°C or 300°C cure. The lid seal is done at 300°C. Then the LCC is soldered to a board which may be subsequently potted in a metal housing. The silicon die, the epoxy die attach, the ceramic carrier, the potting material, and the metal housing all have different coefficients of thermal expansion, and different stiffnesses. When the package returns to room temperature after one of these processes, the various materials shrink at different rates. This packaging process may leave devices with an effective residual stress which depends upon the packages processes, materials, and geometry.

Although the simulation process explained in the previous section is only qualitative, as there are many uncertain factors associated with packaging that are both known and unknown, it can be used for modeling the effects of packaging steps on the residual stress.

4.1.1.1 Epoxy Die Attach

This section provides a preliminary thermal analysis of the die attach process, where the die is attached to a ceramic carrier using epoxy. Results need to be verified and validated

experimentally. Results from a model that includes an epoxy layer used for die attach are shown in Figure 4-6. The LCC itself is not attached or constrained in any way except to remove rigid body modes. The model does include an epoxy layer for die attach.

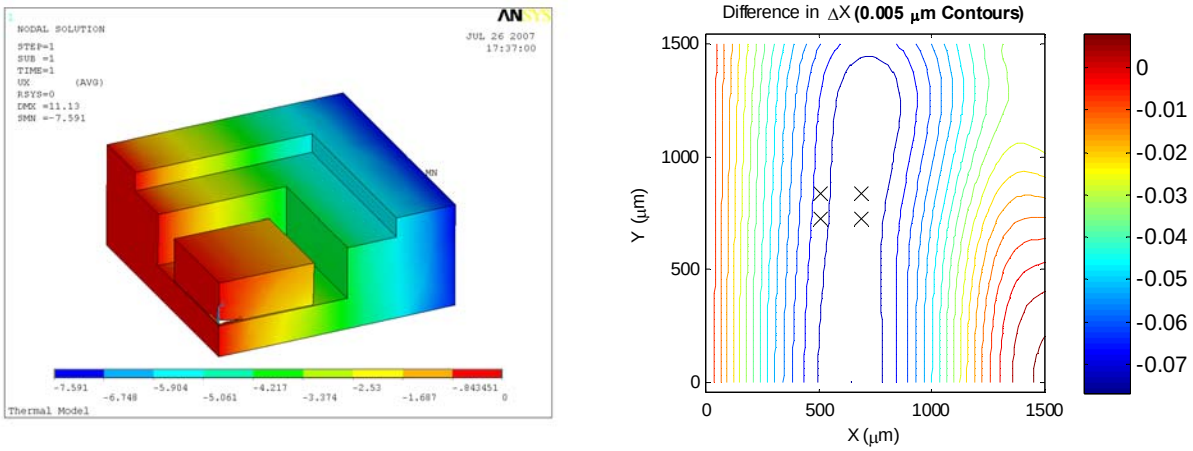

Figure 4-6. Epoxy die attach at 300°C cooled to 22°C, showing displacement in *x*-direction.

The analysis was repeated except with the bottom of the LCC constrained in the transverse/Z-direction. Figure 4-7 illustrates the difference between the constrained and unconstrained case. These results indicate that there is some sensitivity to bending of the LCC package. This could result from how the LCC is attached to the housing or circuit board. To estimate the change in set-point/F_{min}, use the contours to estimate the change in distance between anchor locations and then refer to Figure 4-2.

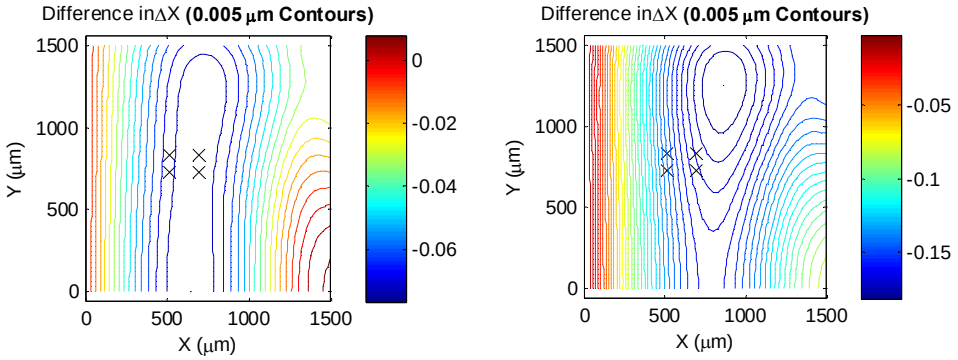

(a) LCC unconstrained (b) LCC constrained in *z*-direction

Figure 4-7. Epoxy die attach at 300°C cooled to 22°C.

The results above raise the question of whether the mechanism is sensitive to bending of the package as Figure 4-8 conceptually illustrates. Figure 4-9 compares results (edges are deflected δ_z = 1 µm, reaction force is 15.7 Newtons (3.5 lbs)) to the unconstrained case.

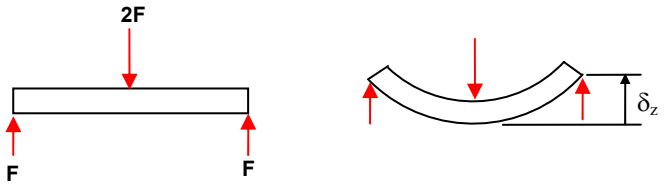

Figure 4-8. Bending of the LCC to predict effect on residual stress in the mechanism.

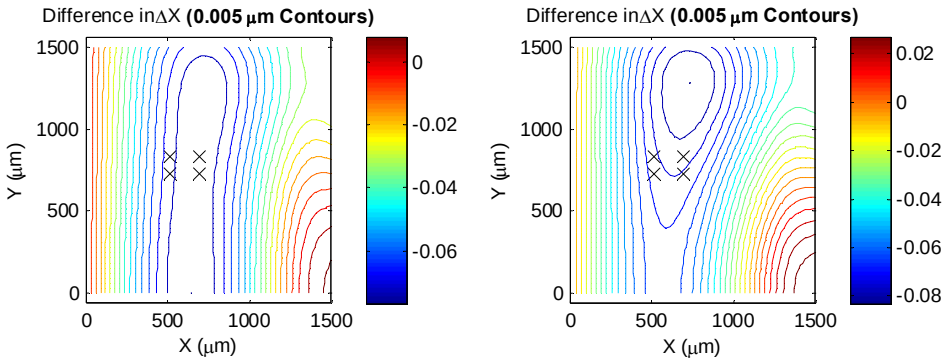

(a) LCC unconstrained (b) Edges deflected δ_z=1 µm

Figure 4-9. Bending the LCC. Epoxy die attach at 300°C cooled to 22°C.

4.1.1.2 Lid Seal

The lid seal process appears to not have a significant additional effect on the residual stress beyond die attach. Figure 4-10 below should be compared to Figure 4-7a. The lid makes the LCC stiffer with respect to bending. With the epoxy die attach 3.5 lb was required to bend the device 1 µm, whereas the bending force after lid seal was 6.0 lb.

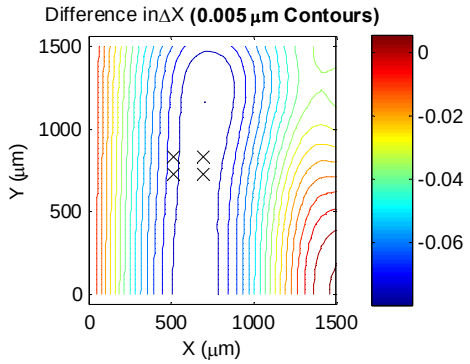

Figure 4-10. Epoxy die attach with lid seal at 300°C then cooled to 22°C.

4.2 Residual Stress Test Structures

Test structures were included in the Rev 2 design layout in order to evaluate the effect of packaging on residual stress in bi-stable mechanism components (see Figure 4-11). These test structures, referred to as "bowtie" structures due to their shape, can be used to measure a wide range of residual stress. The displacement of the bent beams is measured using either a vernier or image processing (pattern matching). The residual stress is determined using a model of the device to back out the stress based on the geometry of the beams. Uncertainties in processing, such as edge bias, and uncertainties in material properties, such as the Young's modulus, contribute to uncertainty in measurements, in addition to uncertainties associated with the vernier or image processing.

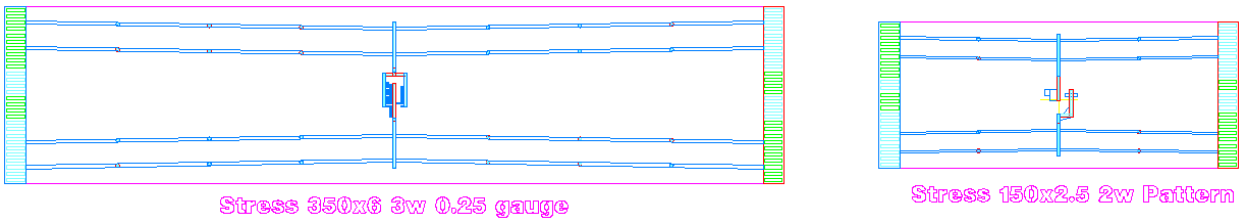

Figure 4-11. Bowtie structures on the Rev 2 die.

Although analytical equations exist for evaluating stresses for a given displacement [8], a simple approach is to use a curve fit from a finite element analysis. This analysis includes the effects of the center shuttle; however, for test structures on Rev 2 die, the shuttle is small (3 μm wide) so that the effect is insignificant.

4.2.1 Nominal Stress vs. Displacement

Uni-axial residual stress (σ_u) vs. displacement (d) can be fit using a quadratic polynomial

$$\sigma_u = c_1 d^2 + c_2 d + c_3 \tag{2}$$

where coefficients are unique to a particular design. This model is referred to as the "meta-model" where the displacement, d is the vernier reading. The individual sets of beams actually displace $d/2$ toward or away from each other. This curve fit has some error associated with it, and is valid only for a specified range of displacement. The range of displacement is chosen such that the error is some minimal value, say less than 0.02 MPa. Using a quadratic polynomial, the device is not as accurate for tensile stresses, but we rarely expect to see residual stress that is tensile in our case.

Table 4-1 gives the coefficients for calculating the nominal residual stress from the displacement measurements of the two bowtie structures on Rev 2.

Table 4-1. Coefficients for Stress vs. Displacement of Bowtie Structures

Structure	c_1	c_2	c_3
350x6	-0.1657	4.811	0.1704
150x2.5	-0.6255	13.21	0.1004

4.2.2 *Uncertainty Analysis*

Stress measurements include 4 main uncertainty variables: displacement, edge bias, modulus, and model error. The curve fit in Equation 2 does not account for these uncertainties because the coefficients are actually functions of the edge bias and the modulus. A second-order response surface model was created to include the effects of small changes in the uncertain variables, to calculate overall uncertainty, and to map out the effects of uncertainty variables. For small changes in uncertain variables, coefficients in Equation 2 vary either linearly (with respect to the modulus) or quadratically (with respect to the edge bias). The coefficients for a specific design are a function of the edge bias and modulus,

$$c_i = b_{io} + b_{i1}p + b_{i2}E + b_{i4}p^2 + b_{i5}E^2 \tag{3}$$

where p is the edge bias and the b coefficients are determined using regression analysis. Figure 4-12 shows the difference between stresses calculated using the meta-model and stresses from ANSYS. Although model error is not statistical in nature, it is small. From these plots it was assumed that 95% of the time model error is within ±0.2 MPa.

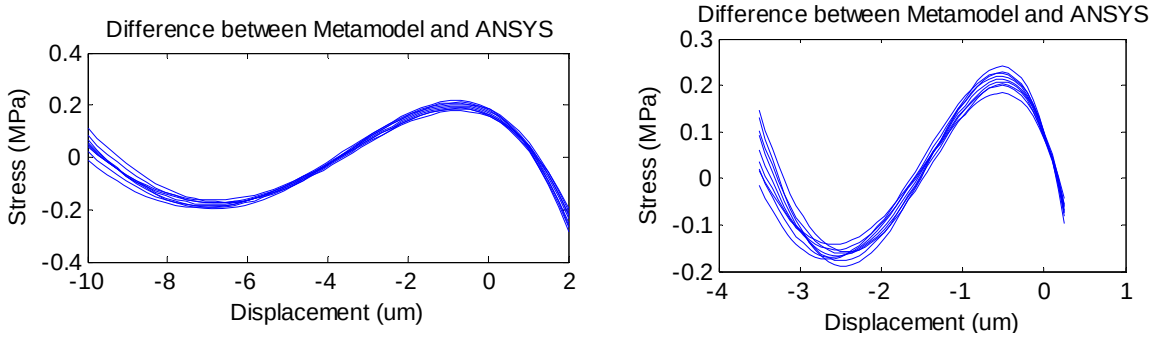

Figure 4-12. Difference between the metamodel and the ANSYS results for (a) the 350×6 µm test structure; (b) 150×2.5 µm test structure.

4.2.3 *Results from Parametric Testing (P-Test)*

For each lot run through fabrication, parameter tests are performed on quarter wafers to make measurements of residual stress in Poly1/2 and Poly3. For RS630, the P-Test residual stress data is summarized in Figure 4-13. The *x*-axis is the radial distance in cm to the center of the reticle with respect to the center of the wafer. The *y*-axis is the uni-axial residual stress in MPa.

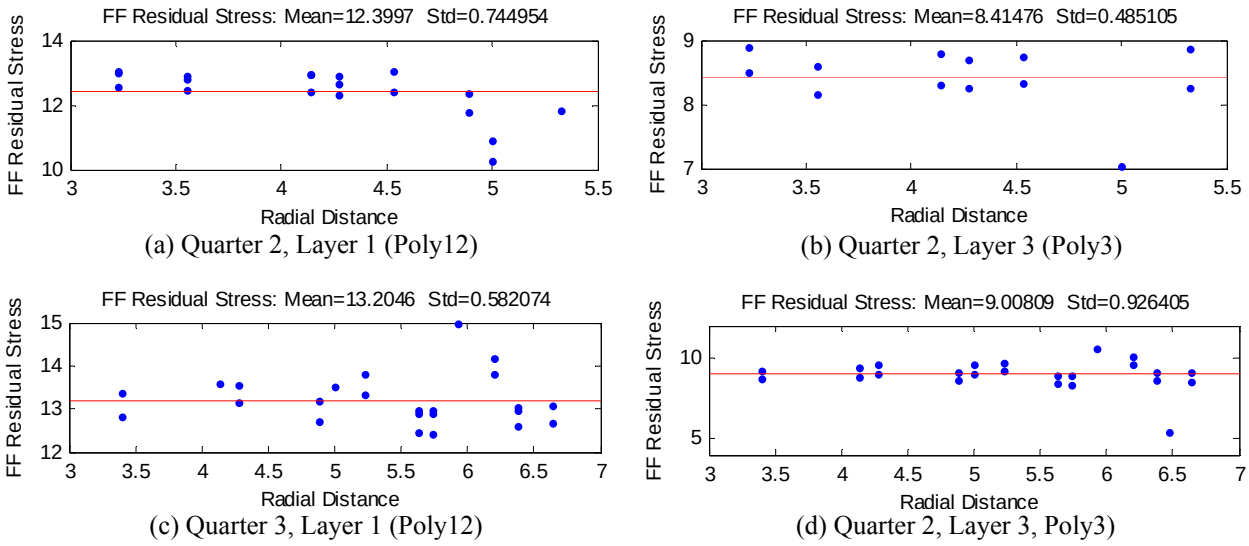

Figure 4-13. Residual stress measurements from P-Test.

4.2.4 Effect of Different Residual Stress in Poly1/2 and Poly3

P-Test data shows a difference in residual stress in the Poly1/2 and Poly3 layers. The question that must be answered is whether residual stress test structures are affected by this difference. Residual stress calculated from displacement measurements of test structures represents a combination of the stress in both layers. To isolate the stress in a single layer, the test structure would need to be fabricated in just one layer.

To investigate this question, a model was created that would allow a different residual stress to be specified for the Poly1/2 and Poly3 layers. Figure 4-14 shows the model, where beam elements are used to model the flexible segments, and rigid links are used to connect the two layers.

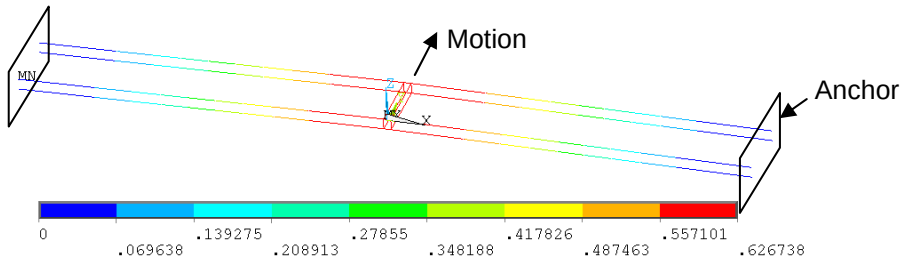

Figure 4-14. Displacement of one side of the residual stress test structures.

To investigate whether the longer test structure would be more sensitive to a difference in residual stress between the layers than the shorter test structure, a hypothetical case was studied in which the Poly1/2 layer sees -20 MPa and Poly3 sees -15 MPa. The displacement of the multi-layer model gave a displacement of 3.296/2 for the longer device, and 1.253/2 for the shorter device. Note that the model includes only one side of the structure, so the vernier reading would be twice the reported displacement. With an input displacement of 3.296 and 1.254 μm, the metamodel predicts a stress of -17.49 MPa for the longer device and -17.44 MPa for the shorter

device. The difference in the calculated stresses was not very significant (only 0.05 MPa) and was lower than the measurement uncertainty. Therefore, differences between measurements in Structure 1 and Structure 2 are not due to differences in stress in the individual layers.

The test structures were purposely made with two layers because that closely resembles the topology of the bi-stable mechanisms. The multi-layer model shows that differences in residual stresses across the different layers can produce an out-of-plane displacement.

5. DYNAMIC MODELING

5.1 Background

The previous 2006 report [1] described a single degree of freedom dynamic model in MATLAB® used to characterize the shock switches. This model treated the device as a second-order system, consisting of a nonlinear spring, a dashpot, and an inertial mass. The model included both the contacts and the hard stop, and a coefficient of restitution (COR) was specified to simulate the impact and rebound of the mass. The spring force was calculated by interpolation from the force vs. displacement curve predicted by the quasi-static finite element model. The mass was assumed to be a point mass. The amount of damping is unknown, but can be estimated based on experiments.

5.2 Model

The dynamic model used to analyze the Revision 2 designs is similar to the model described in the previous report [1]. The state-space form of the differential equation is

$$\begin{aligned} \dot{x}_1 &= x_2 \\ \dot{x}_2 &= a_g(t)\cdot g - \frac{b}{m}x_2 - \frac{f(x_1)}{m}, \end{aligned} \tag{4}$$

where m is the mass, g is gravity, $a_g(t)$ is the input acceleration in g's as a function of time, x_1 is the position, x_2 is the velocity, b is the damping coefficient, and the force $f(x_1)$ from the nonlinear springs is a function of the position.

5.2.1 Frequency Calculation

The frequency f (not to be confused with the force, $f(x_1)$, described above) at the open position or second stable position (SSP) and the corresponding period, $T=1/f$, are useful for describing the general operating characteristic of the shock switch. This section will describe how the frequency is calculated, and following sections will show how results relate to the dynamic behavior of the switch.

The frequency, $f = \omega/(2\pi)$, of the in-plane mode at the SSP was determined via modal analysis using the 3D model described in Section 3.5.2 and Table 3-7. It was also evaluated using the analytical single-degree-of-freedom (SDOF) transient dynamic model followed by an FFT analysis (the discrete Fourier transform function in MATLAB). The frequency can also be calculated from the stiffness obtained from the derivative of the force vs. displacement curve. Table 5-1 compares frequency results from all three methods for the 8 devices. Note that the modal analysis used a relatively coarse mesh and in one test case was found to be off by 5 kHz (about 10%). Note all results are within 10% of each other with the exception of the J2C device.

Table 5-1. Frequency Calculation at the SSP via 3 Different Methods

		From F vs. D		**SDOF**	Modal
Device	**Mass** (mg)	***k*** (N/m)	***f*** (kHz)	***f*** (kHz)	***f*** (kHz)
M2A	4.053E-04	19.72	35.1	37.7	39
M2B	2.022E-04	19.72	49.7	53.5	55
M2C	1.037E-04	19.72	69.4	74.6	78
M2D	1.985E-04	86.94	105.3	100.0	106
J2A	4.302E-04	27.05	39.9	38.0	42
J2B	2.105E-04	22.98	52.6	53.5	56
J2C	2.224E-04	62.42	84.3	79.4	92
J2D	2.299E-04	96.54	103.1	105.3	106

The frequency at the SSP and the corresponding period, $T=1/f$, are useful for determining the length of time to run simulations. The period for all eight devices falls between 9 and 26 microseconds. Table 5-2 summarizes periods and frequencies calculated using the SDOF model along with the FFT at both the first and second stable positions.

Table 5-2. Frequency at FSP and SSP Calculated Using the SDOF Model with No Damping

	First Stable Pos.		**Second Stable Pos.**	
	Period	**Freq**	**Period**	**Freq**
Device	(µs) ±0.05	kHz	(µs) ±0.1	kHz
M2A	7.82	128	26.5	37.7
M2B	5.52	181	18.7	53.5
M2C	3.95	253	13.4	74.6
M2D	4.88	205	10.0	100.0
J2A	7.69	130	26.3	38.0
J2B	5.78	173	18.7	53.5
J2C	5.57	180	12.6	79.4
J2D	5.19	193	9.5	105.3

5.2.2 Damping

Damping can be included in the SDOF model by specifying a value for the damping coefficient *b*. In simulations, the value *b* is estimated from a damping ratio determined from experimental results or using the relationship between the damping ratio and the quality factor $\zeta = 1/(2Q)$. A quality factor of 100 gives a damping ratio of 0.005. The damping coefficient is then calculated using the relationship for a linear system, $b = 2m\omega\zeta$, where omega is the natural frequency. Because of the nonlinear force vs. displacement in the bi-stable mechanism, the natural frequency as defined by $\omega = \sqrt{k/m}$ is not constant since *k* varies with position. For purposes of dynamic modeling, the natural frequency for calculating the damping coefficient is based on the stiffness at the second stable position.

To determine what level of damping to use in simulations, oscillatory decay of a Revision 1 50g device was compared against test data. The comparison is shown graphically in Figure 5-1. A quality factor of 150 was determined to best represent the test data. This quality factory was used for dynamic simulations results presented in this chapter unless otherwise noted.

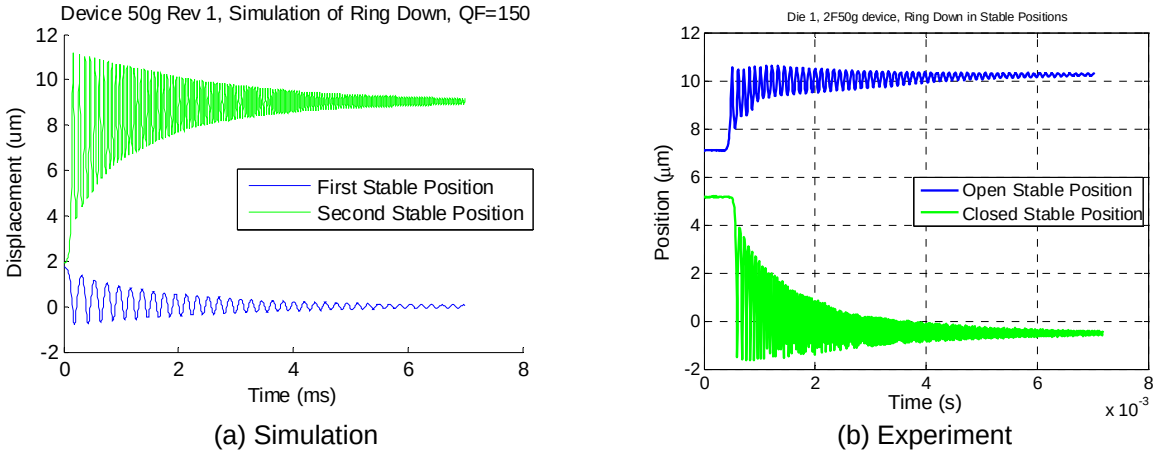

(a) Simulation (b) Experiment

Figure 5-1. Simulation of ring down—Revision 1 50g device using SDOF model.

5.2.3 Force Calculation

The force $f(x_1)$ is calculated via interpolation from the force vs. displacement curve produced by the quasi-static analysis of the shock switch, where the FSP is at x=0 (or near zero due to residual stress). Simulation results represent device response to a shock event starting from rest at the open position or SSP. The force vs. displacement curve is transformed so that x=0 at the SSP and a positive displacement represents motion of the shuttle in the direction of the FSP. This new "reversed" curve is then saved as a data table in a text file which is subsequently interpolated during simulations to calculate a force for a particular displacement.

5.2.4 Acceleration Profile

The driving force in the SDOF model is the shock event, represented as an acceleration vs. time profile. A haversine pulse function is used to simulate a shock event and characterize devices. Profiles may include an "echo" or "ringing" and can be used to simulate non-ideal profiles by either creating a custom $a_g(t)$ function or by interpolating from a data table.

5.3 Dynamic Model Predictions

This section describes dynamic response to in-plane acceleration loads. The dynamic model does not simulate the response to an out-of-plane shock because it uses a 1-D force vs. displacement curve to evaluate spring force.

Figure 5-2 shows the dynamic response of the J2A device to a 4000g-30μs shock pulse. The bounce on the contact is modeled using a coefficient of restitution of 0.5. The dashed blue line is the unstable equilibrium position and the dashed red line is the specified pulse width.

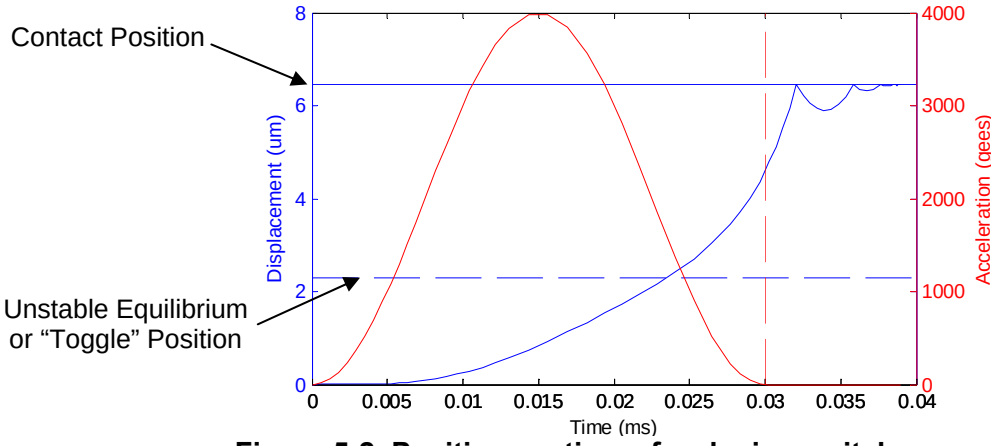

Figure 5-2. Position vs. time of a closing switch with the acceleration profile superimposed.

5.3.1 Acceleration vs. Pulse Width

One convenient way to characterize the dynamic response is to determine the acceleration for which the device closes as a function of the pulse width. Broadly speaking, long pulse widths correlate with loading the switch into a centrifuge and very slowly increasing the angular speed until the switch closes. Long pulse widths correspond very well with quasi-static analyses of the shock switch. However, to properly characterize the switch for short pulse widths, dynamic effects must be considered. In general, the notion of short versus long pulse widths is relevant only when specific devices are considered.

Figure 5-3 shows multiple simulations (fixed pulse width of 30 µs but different shock magnitude) superimposed on the same graph. Note that frequency of oscillation is dependent upon amplitude of oscillation, and that ringing is not a perfect sine wave. These are nonlinear spring effects.

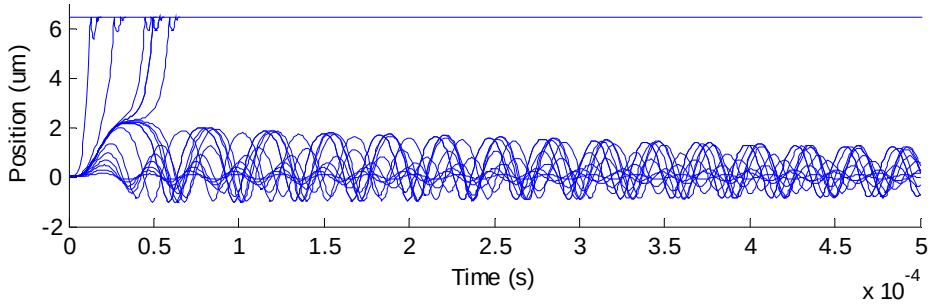

Figure 5-3. J2A device: dynamic response for fixed pulse width of 30 µs but different shock magnitudes.

When the previous simulations are run for multiple pulse widths, a plot of acceleration vs. pulse width can be created. Figure 5-4 and Figure 5-5 characterize the overall response for J-series and M-Series devices respectively. Any point above the blue curves represent a particular combination of shock magnitude and pulse width that will close the device. In contrast, combinations of shock magnitude and pulse widths below the blue curve represent cases that do

not close the switch. Also shown in each figure is a vertical line representing the inverse of the resonant frequency at the SSP and a horizontal line representing the quasi-static set point from Table 3-3. Note how resonant frequencies at the SSP roughly coincide with the location of the elbow in each curve.

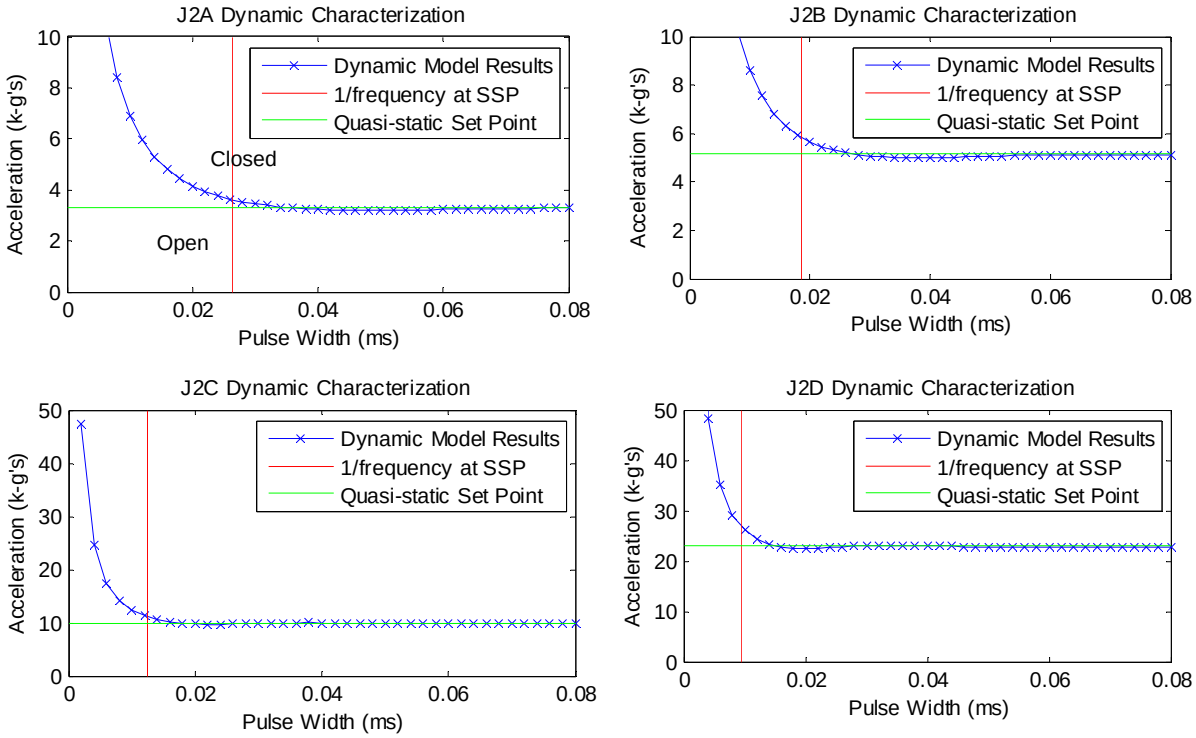

Figure 5-4. Dynamic characterization of J-series devices. Note change in y-axis scale (acceleration) for different devices.

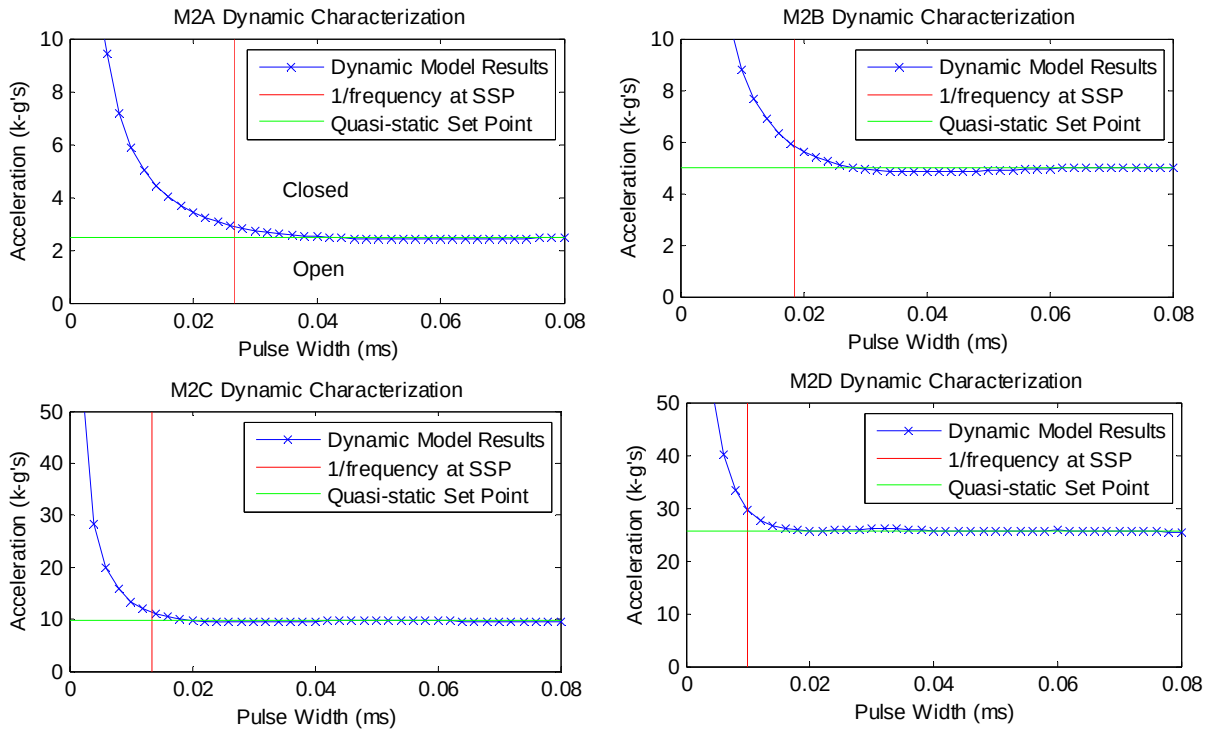

Figure 5-5. Dynamic characterization of M-series devices. Note change in y-axis scale (acceleration) for different devices.

5.3.2 Response to Shock in Reverse Direction

In this section, response of the switch (in its open position (SSP)) to shock in the reverse direction is briefly presented. By applying shock in the reverse in-plane direction, the mass moves towards the hard-stop—at least initially. In this scenario, closure typically occurs when shock magnitude and duration are such that the proof mass bounces off the hard-stop, reverses direction, and moves towards closing the contact. It may or may not close the contacts; this depends upon shock magnitude and duration. Several scenarios are presented in this section.

Modeling results presented are for device labeled J2A which has a quasi-static set-point of 3294 g's (see Table 3-3). The first scenario shows results for a 10 k-g magnitude shock with 30 micro-seconds pulse width. This in indicated in Figure 5-6. Note that the bottom solid blue line is the hard-stop position and the top solid blue line is the position of contact closure. The dashed blue line is the unstable equilibrium position. In this case, the mass initially moves towards the hard-stop but does not reach it and subsequently returns to the open position and oscillates. Two more scenarios are presented in Figure 5-7. Note that the coefficient of restitution (COR) in these cases was COR=0.5. In case (a), both shock magnitude and duration were increased and the mass reaches the hard-stop and chatters 3 times, but then it simply returns to the open position and oscillates. In case (b) a much longer pulse-width is applied and the switch response is similarly slowed down and correlates very well with the applied shock. Once again the device returns to the open condition. In both cases it is worth noting that the device is not predicted to close.

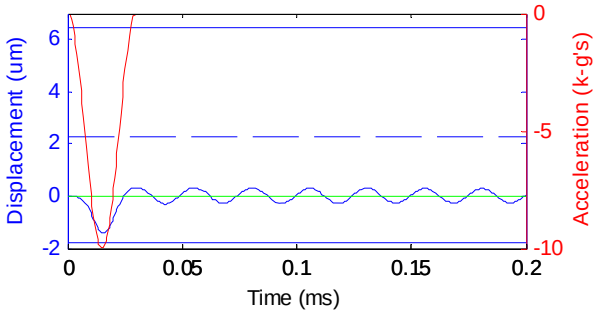

Figure 5-6. Device J2A response to -10k-g, 30µs pulse.

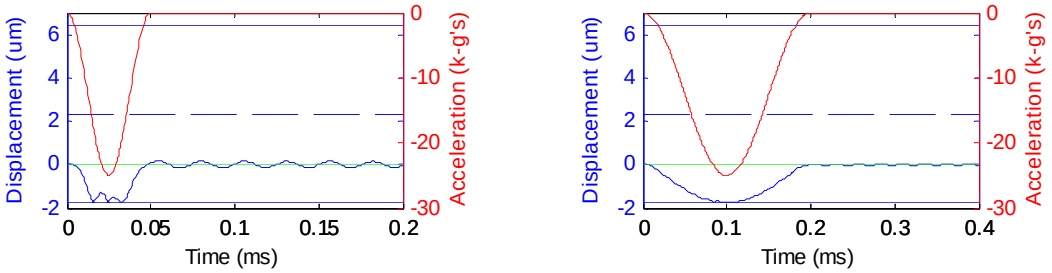

(a) -25k-g, 50µs Pulse (b) -25k-g, 200µs Pulse

Figure 5-7. Device J2A response to -25k-g and (a) 50 µs pulse; (b) 200 µs pulse

A different result is shown in Figure 5-8 where the pulse-width is reduced. In both cases the device closes. In case (a), the mass does not quite bounce off the hard-stop but it has stored enough elastic energy at the end of the shock event so that its subsequent exchange and conversion of elastic energy to kinetic energy ultimately causes the device to close. In case (b) the combination of shock magnitude and direction causes the mass to quickly reach the hard-stop and bounce but quickly reverse direction and move toward the hard-stop once again. In the end, the scenario in (b) is very similar to (a) – the device is very close to the hard-stop when the shock event is over, and stored elastic energy is ultimately sufficient to cause the device to close. Note that all simulation results are for COR=0.5.

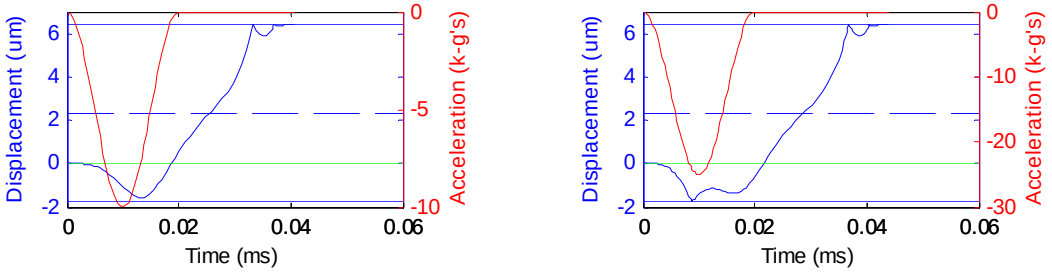

(a) -10k-g, 20µs Pulse (b) -25k-g, 20µs Pulse

Figure 5-8. Device J2A response. (a) -10 k-g, 20 µs pulse; (b) -25 k-g, 20 µs pulse.

To toggle devices closed, a rule of thumb is that pulse widths for shocks in the reverse in-plane direction must be smaller than the period corresponding to the resonant frequency (T=1/f) at the open position. A full characterization of a device in response to shock in the reverse direction is complicated by the fact that at higher accelerations the mass hits the hard stop and may or may not bounce, depending on the coefficient of restitution. The rule of thumb above generally applies, but for a given shock pulse that is shorter than the period at the SSP (open), there is not just one acceleration that defines the threshold at which the shock will or will not close. This is shown in Figure 5-9 for device J2A (COR=0.5). The blue curve represents a boundary between two areas—one area being the combination of shock magnitude and duration for which the device closes and the other representing shock magnitude and duration for which the device remains open (not closed).

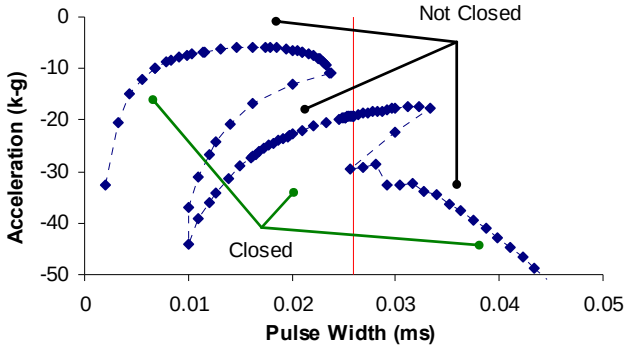

Figure 5-9. Acceleration vs. pulse-width curves for device J2A in response to a shock in the reverse direction, starting from the SSP (COR=0.5).

5.3.3 Shock Response When Closed

It is theoretically possible for a shock event or quasi-static acceleration to re-open a device after it has closed. However, the magnitude of the shock or steady acceleration is very high. In this section such scenarios are briefly presented. For this to occur, an acceleration in the reverse direction must first overcome the contact force. In general, the contact force is quite high compared to the quasi-static set-point. Modeling results for two scenarios are shown in Figure 5-10. It is important to note that the quasi-static set-point of J2A (see Table 3-3) is 3294 g and that in both scenarios shown the applied shock magnitude is approximately 35 k-g. The magnitude of applied shock is more than 10 times the quasi-static set point. Also note that the duration of applied shock is in milliseconds rather than micro-seconds. In both cases the mass overcomes the contact force and moves beyond the open position and bounces off the hard-stop and then subsequently settles down at the open position.

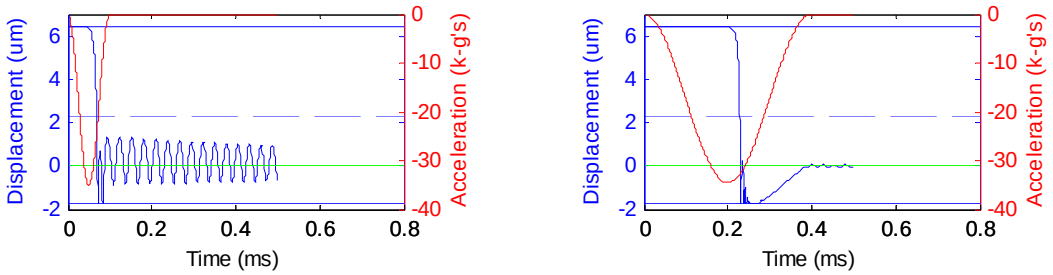

(a) -35.1 k-g, 0.1 ms pulse (b) -34.5 k-g, 0.4 ms pulse

Figure 5-10. J2A (3294 k-g) response to shock events: closed device to re-opened device.

From a quasi-static view point, applied accelerations in the reverse direction can open a device. These accelerations are given in Table 5-3 for all Revision 2 device designs. This force is slightly different from F_{max} because it is calculated at the nominal contact position given in Table 3-3, which does not exactly correlate with the location of F_{max}.

Table 5-3. Static Acceleration Required to Close/Open Rev 2 Devices

Device	Close k-g's	Mass mg	$F_{contact}$ mN	Open k-g's	Ratio open/close
M2A	2.49	4.053E-04	-105.4	-26.5	10.7
M2B	4.99	2.022E-04	-105.4	-53.1	10.7
M2C	9.72	1.037E-04	-105.4	-103.6	10.7
M2D	25.69	1.985E-04	-151.0	-77.5	3.0
J2A	3.29	4.302E-04	-145.3	-34.4	10.5
J2B	5.17	2.105E-04	-141.0	-68.3	13.2
J2C	9.93	2.224E-04	-93.1	-42.7	4.3
J2D	22.95	2.299E-04	-230.8	-102.3	4.5

In theory, it is possible to open a device with short pulse widths; however it is more difficult. Three scenarios for J2A are shown in Figure 5-11. Under precise conditions where there is sufficient damping in the mechanism, the device could be toggled open. Notice that for the -41000 k-g and the -42000 shock the device does *not* open. For simulations in which a quality factor of 150 is assumed for damping, the window for which the device stays open is only within a few g's.

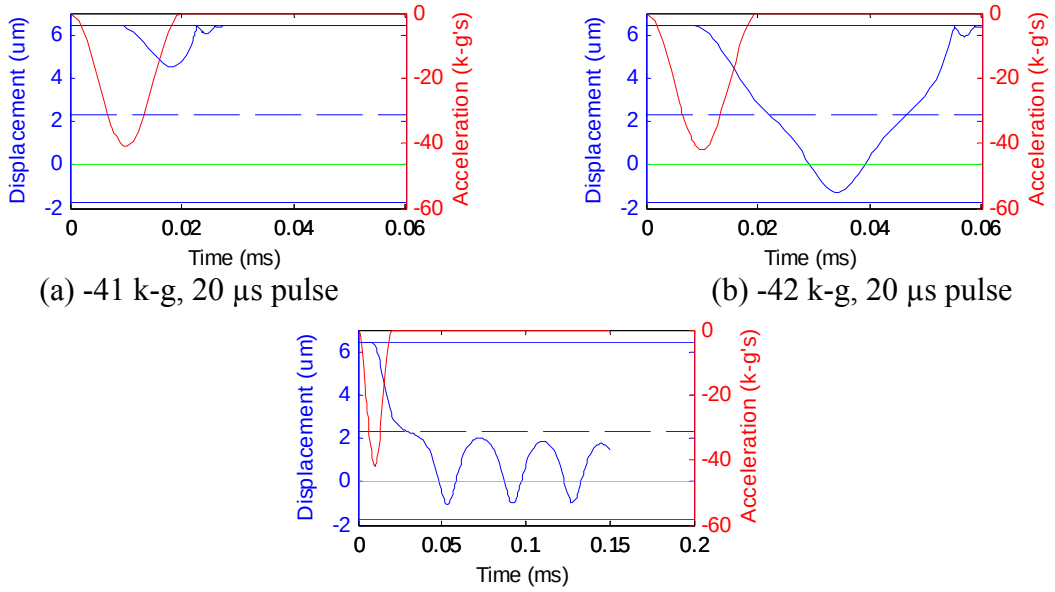

Figure 5-11. Shock response of J2A from the closed position for a short pulse width.

5.3.4 Vibration Response

It is very important to characterize device response to vibration. Frequency response characteristics provide insight into how devices will respond to shock. Practically speaking, shock events of interest usually contain a broad band of frequency content. This content is often induced by a localized event that results in wave propagation and ringing in the vicinity of the event. Shock switches mounted nearby such events experience a broad range of inputs along all axes.

Frequency response is characterized by applying steady harmonic acceleration to the device. Of particular interest is the combination of frequency and magnitude of input which will cause a device to close. Assuming zero initial conditions, the transient response of J2A for two harmonic inputs is shown in Figure 5-12. In case (a), the device does not close and in case (b), it does. Two different frequencies were used while the amplitude of the harmonic input was fixed at 2000 g. This clearly illustrates sensitivity to frequency content. The harmonic excitation is characterized as $a_g(t)=A\sin(\omega t)$, where a_g is the acceleration in g's, A is the 0 to peak amplitude in g's and ω is the frequency of oscillation in rad/s. Note that in case (b) the magnitude of excitation is lower than the J2A set-point and yet the device closes. This is because the frequency of excitation is the resonant frequency at the open position for J2A.

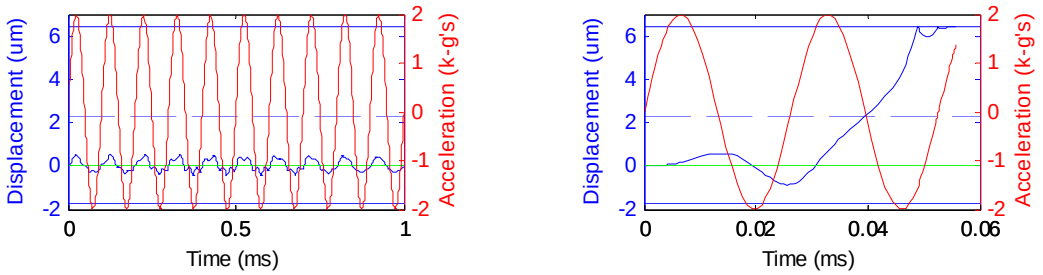

(a) 2 k-g, 10 kHz (b) 2 k-g, 38 kHz

Figure 5-12. J2A response to harmonic input with amplitude of 2 k-g (1414 RMS).

The frequency response of each device is computed by numerically sweeping through the full range of frequencies. Each case is evaluated and characterized using the dynamic model with zero initial conditions and then determining whether or not the device closes for a given magnitude of harmonic input. Results for J2A are given in Figure 5-13 below. The plot shows the amplitude in k-g's for convenience of comparing to other devices. For reference or comparison to test results, the root mean square (RMS) value of the harmonic input is 0.707*A* (sine wave).

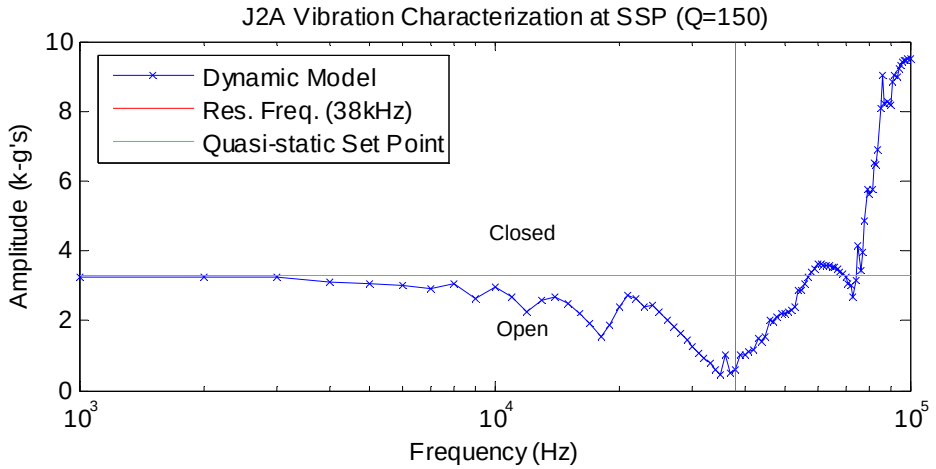

Figure 5-13. Computed frequency response for J2A.

As expected, the lowest amplitude required to toggle the device is near the resonant frequency of the device (38 kHz). Note that this amplitude is significantly less than the quasi-static set-point. The quasi-static set-point is accurately represented at low frequencies. At frequencies beyond the resonant frequency very large amplitudes (much higher than the quasi-static set-point) are required to close the device. In general these results depend on the level damping used in calculations. For results presented here, a quality factor of Q=150 was used. These results indicate that J2A devices close at levels near the quasi-static set-point for frequencies below 10 kHz. For all other frequencies, the model predicts that J2A device closures strongly deviate from the quasi-static set-point as indicated.

Figure 5-14 and Figure 5-15 are the similarly computed frequency response functions for the remainder of the J-Series and M-Series devices, respectively. Note that all the graphs have the

same general shape and characteristics. Because springs for three of the M-series are identical (M2A, M2B, and M2C devices), only M2A and M2D device results are presented.

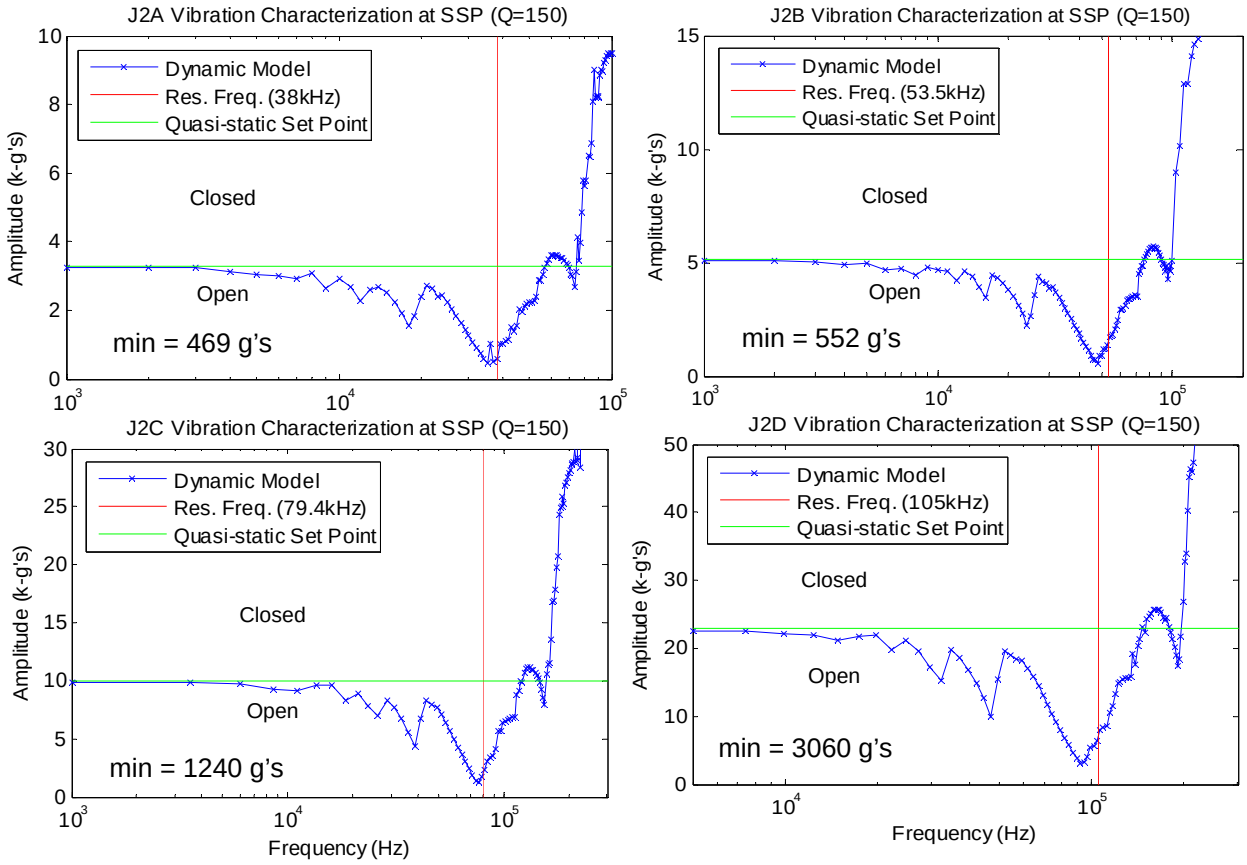

Figure 5-14. J-Series computed frequency response.

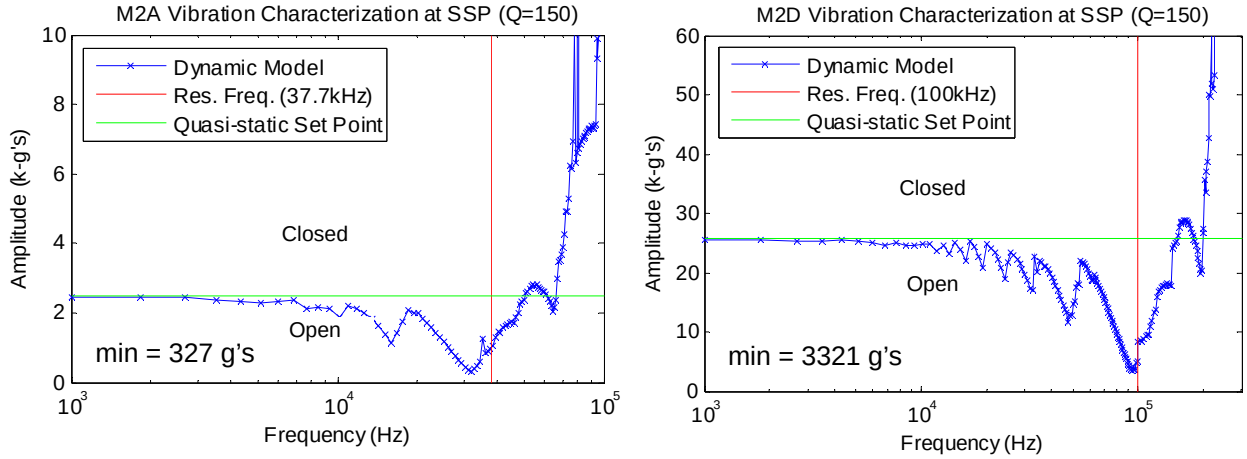

Figure 5-15. M-Series computed frequency response.

6. MEMS METROLOGY: MEASURING THE FORCE VERSUS DEFLECTION RELATIONSHIP

6.1 Interfacial Force Microscopy

6.1.1 Introduction

The Interfacial Force Microscope (IFM) is a unique scanning-probe technique invented at Sandia to study adhesion and the nano-mechanical properties of surfaces and interfaces. It is distinguished from other scanning probes, for example the Atomic Force Microscopy, by its use of a self balancing, force-feedback sensor. The technique was specifically designed to eliminate the inherent instability present in all force sensors which depend on the deflection of a spring element to determine the force. The sensor, schematically illustrated in Figure 6-1 below, consists of a "teeter totter"-like top plate suspended on torsion bars extending in and out of the page. The schematic shows the silicon top plate suspended above two gold capacitor pads deposited on a Pyrex substrate. The capacitor gap is etched into the Pyrex. These two are then anodically bonded to form the sensor. The teeter-totter top plate is suspended by torsion bars above the pads with a gap of about 6 μm. A tip (of virtually any solid material) is attached to one side of the teeter totter. The dimensions of the finished sensor are 1×1 cm^2.

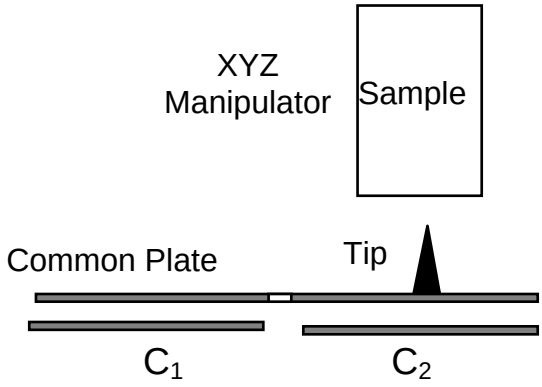

Figure 6-1. IFM sensor schematic.

A sharp tip is placed on one side of the teeter totter so that a force applied to the tip by, for example, an adhesive interaction with a sample, rotates it about the torsion-bar axis. This rotation, in the present version, is detected by an radio-frequency (RF) bridge circuit, which causes the appropriate voltages to be applied to the two capacitor pads by a full proportional-integral-derivative) PID controller in order to ensure that the teeter totter remains balanced in its original position. Thus, the tip force is automatically balanced by the applied electrostatic force and the sensor is mechanically stable. In its present form, the sensor balances the total torque applied to the tip and is, thus, sensitive to lateral as well as normal forces. However, it does not measure the two independently. The stability of the sensor is absolutely necessary when applied to the measurement of devices that are mechanically unstable. In its application to the force/displacement rheology of MEMS-type devices, only lateral forces are present so that the lack of independence is not an issue. An SEM image of a shock sensor device and the IFM tip

are shown in Figure 6-2 below. The image of the IFM tip is positioned to push on the left-hand tab (indicated by the grey arrow).

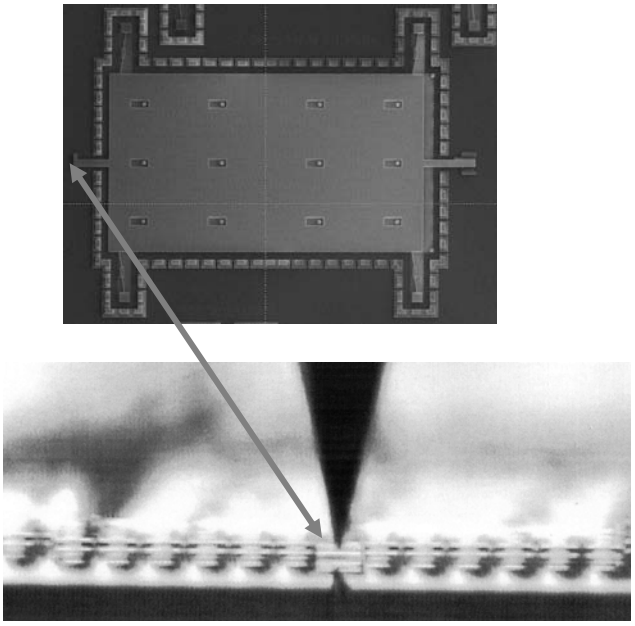

Figure 6-2. An SEM image of a shock-switch and IFM tip.

6.1.2 Demonstration Measurements

In recent demonstration measurements using this older IFM version, the tip was positioned at the ends of the shuttle mass by optical microscopy, which was a rather tedious and time-consuming operation. Figure 6-2 shows a schematic of a particular component on the MEMS shock-switch die as well as a video frame of the W tip in position to displace the shuttle mass and record the force vs. displacement profile up to the point at which the shuttle goes unstable and snaps to its other (right-hand) stable position. The instability is clearly indicated on the force vs. displacement map as the point at which the lateral force suddenly goes to zero. The tip is then moved to the right-hand side of the shuttle and pushed backwards to characterize the second half of the force vs. displacement behavior. The two results are then brought together at the point where they both loose contact. A typical result is shown in Figure 6-3. For purposes of comparison, both model results and IFM measurements are included on the same plot.

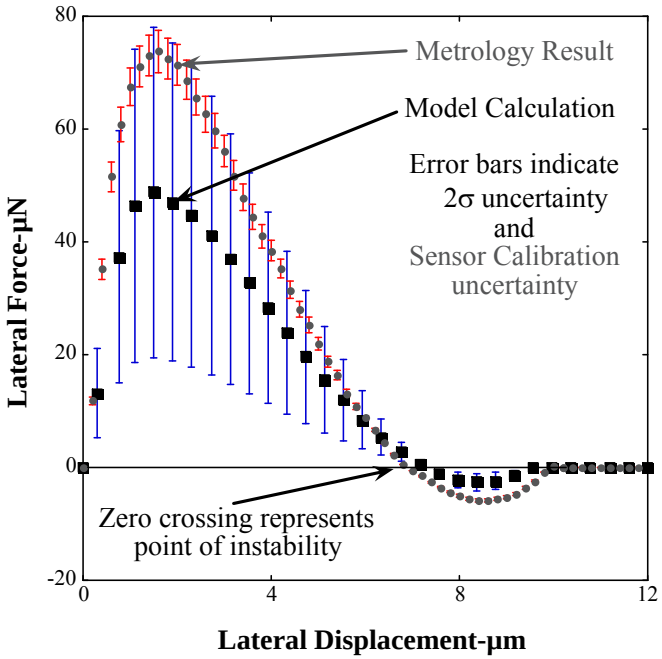

Figure 6-3. IFM and model results: force versus displacement measurement.

The error bars on modeling results indicate the 2σ confidence level for modeling parameters, while IFM error bars indicate the level of confidence in the IFM sensor calibration. Clearly, the general shape of the curves is very similar. However, even if the IFM results are scaled to fit the major peak in model results, the important instability point is still not coincident. The discrepancy is considered to be the result of residual stresses in the released die. However, it is clear that such a metrology tool could be very valuable in providing feedback to component designers.

In its present embodiment, the IFM is not ideally suited for these measurements. Accurate sensor calibration is difficult since no applicable force standards are currently available at the µN level. In addition, characterizing large numbers of components in order to develop statistically significant results for the design and fabrication verification is extremely tedious and time consuming. However, a significantly improved IFM design is now under development, offering the promise of being able to correct both of these shortcomings.

6.2 Advanced Instrument Development

An advanced IFM instrument is presently in the final stages of development. The sensor concept is basically the same, but the configuration is considerably simpler to fabricate and more reliable to operate. The most significant improvement is in the displacement detection scheme. In the older model, this was accomplished by an RF bridge arrangement which is simple but lacks sensitivity and stability. The older model is also very challenging to operate. The new system utilizes a double-laser interferometer design (US Patent No. 6,718,821) with the capacitor gaps as the two interference cavities. The sensor is schematically illustrated in Figure 6-4.

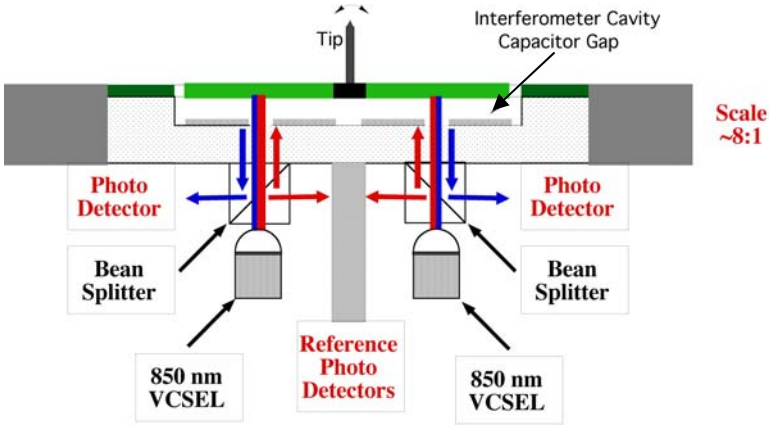

Figure 6-4. Independent 2D laser-interferometer IFM sensor schematic.

The two capacitor pads have small optical ports at their centers through which 850 nm light from two vertical-cavity surface-emitting lasers (VCSELs) is directed. Prior to arriving at the ports, a portion of each beam is directed to two photo detectors in order to record and compensate for changes in the VCSEL intensities. After passing through the laser ports the two beams interfere within the gap, reflect back through the ports and are split off to a set of signal photo detectors. As voltages are applied to the two capacitor pads, the two signal photo detectors record the interference patterns for the two cavities. The desired operating voltages are then chosen to be near points of inflection on the patterns in order to maximize the displacement sensitivities. At this point, the two independent PID controllers are activated and the sensor top plate is forced to remain in the chosen position regardless of forces applied to the tip.

The key advantage of this design is the fact that the normal and lateral forces are measured totally independently. This is achieved by taking the sum and differences of the PID voltages that must be applied to the two pads in order to achieve sensor balance.

6.3 Sensor Calibration

In the laser interferometer sensor, the common plate is suspended above two capacitor pads by springs that have both normal and torsional spring constants, k_n and k_t, respectively. The capacitor gaps constitute the cavities for the two independent interferometer systems. Placing a voltage on the capacitor pads causes an electrostatic attraction to develop between the pad and common plate. The force is given by the derivative of the resulting electrostatic energy, i.e.,

$$F_1 = -\frac{dE_1}{dz_1} = -\frac{d}{dz}\left(\frac{1}{2}C_1V^2\right) = \frac{\varepsilon_0 A V_1^2}{2\left(d_1\right)^2} = K_f^1 V_1^2, \tag{5}$$

where C_1 is the capacitance value for pad 1, ε_0 is the free-space permittivity, d_1 is the gap spacing, A is the pad area and the K term is the sensor force constant, the value of which is what is needed to calibrate the sensor. Since the same voltage is placed on both pads, a similar

equation applies to pad 2, although the parameters A and d_2 may be slightly different due to fabrication errors or an imbalance in the top-plate orientation.

Under operating conditions, the common bias voltage on both capacitor pads is necessary since electrostatic forces are always attractive. Thus, in order to be able to measure repulsive tip forces, the bias force working against k_n, must be reduced by decreasing the bias voltage on both pads. The repulsive normal force is then provided by the initial spring deformation. The magnitude of the bias-voltage reduction is such as to ensure that the position of the top plate remains unchanged. So, in this case, both interferometers show displacement signals in the same direction. In contrast, if a lateral force, i.e., torque, is placed on the tip along the length of the common plate (teeter totter), one interferometer sees a displacement in one direction and the other in the opposite direction, which creates the proper counter torque to balance the torque created by the applied lateral force.

The result is that normal forces are proportional to the sum of the voltage changes on the two pads, with the calibrated force constant for both pads in order to maintain balance. On the other hand, lateral forces are proportional to their difference and the two components are measured totally independently. Sensor calibration is the process of determining the quantitative relationship between the changes required in the bias voltages and the forces that they represent.

The electrostatic force created by the common bias voltage acting against k_n, reduces the gap and causes an increase in the capacitance. The balance of electrostatic and spring forces results in the relationship,

$$k_n \delta z_1 = \frac{\varepsilon_0 A V_1^2}{2\left(d_1 - \delta z_1\right)^2} = \frac{C_1}{2\left(1 - \frac{\delta z_1}{d_1}\right)^2} V_1^2 , \tag{6}$$

where k_n is the normal spring constant, V_1 is the voltage applied to pad 1, d_1 and C_1 are the natural gap spacing and capacitance values for capacitor number one, with zero applied voltage, and δz_1 is the change in the gap spacing under the influence of the voltage V_1. This is a third-order equation in δz_1 and rather tedious to solve in closed form. However, Equation 6 can be rearranged in order to V_1 and expressed as a function of δz_1, i.e.,

$$V_1 = \left[\frac{2 k_n \delta z_1}{C_1} \left(1 - \frac{\delta z_1}{d_1}\right)^2 \right]^{0.5} . \tag{7}$$

In Equation 5, the electrostatic force increases as the square of the gap separation while the counteracting spring force only increases linearly. The result is an instability which occurs precisely when $\delta z_1 = d_1/3$. Therefore, the sensor is stable for voltages less than that necessary to cause δz_1 to go beyond the deformation limit, i.e., $0 < \delta z_1 < d_1/3$. The behavior is illustrated in Figure 6-5; setting the various constants in Equation 7 to those found later in an actual sensor application and plotting V_1 as a function of the δz_1 terms, but graphing it with reversed axes.

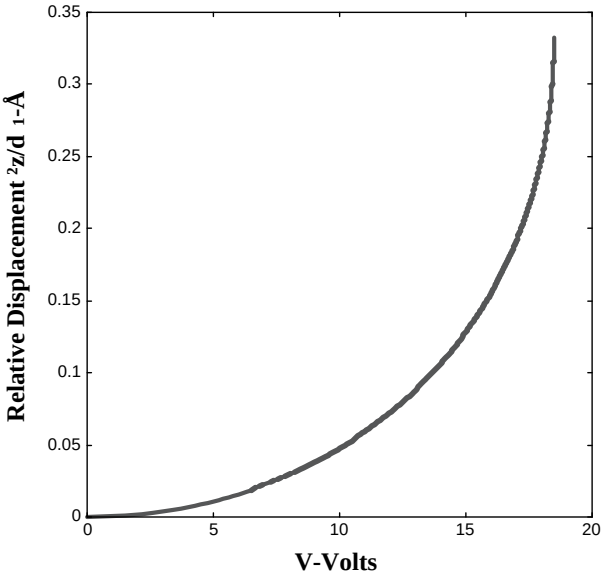

Figure 6-5. Relative top-plate displacement vs. the applied voltage.

Both pads have the same general behavior differing in scaling and the voltage at the instability point due to very slight differences in the value of gap separations d_1 and d_2. This figure illustrates that the instability allows the capacitance to vary only from its initial value of C_1 to 150% of that value as the gap varies from d_1 to $d_1/3$.

In terms of sensor calibration, what is needed is a measurement of the actual pad capacitance as a function of gap separation over a significant portion of its stable range. The slope of this curve, with respect to changes in the gap spacing, yields the force constant directly as a function of the range of possible operating voltages. The relationship of the gap separation and voltage is then determined through the interference pattern itself, as demonstrated below. This procedure allows the desired calibration plot to be accurately generated for both pads over the entire range of operating voltages. First, a measurement of the capacitor as a function of the applied voltage, V is needed. In order to accomplish this at the present prototype stage, two accurate constant-current sources are needed to drive the capacitor pads independently. From the basic formula relating the applied voltage to the resulting capacitance charge, i.e., Q=CV, the capacitance is measured by noting that, for the constant-current case,

$$C(V) = \frac{dQ}{dV} = i / \frac{dV}{dt} . \tag{8}$$

The procedure begins by collecting voltage data across the two pads and their interference intensity patterns as of function of time. The voltage-time plots are then modeled analytically in order to calculate the dV/dt slope at each value of voltage and obtain the capacitance values for the two pads as a function of applied voltage. The fact that the stable region of gap displacement covers only 2/3 of the original gap spacing means that the capacitance can increase only by 50% over its stable region. An initial value for C_1 is known but an accurate number for the area is missing. In order to arrive at the initial gap spacing, interference pattern data as a function of V (shown in Figure 6-6) is used. This function follows the relationship given in Equation 9, where

I_1^+ and I_1^- are the maximum and minimum intensity values (obtained directly from the experimental results), i.e., when the cosine has the values ±1, and λ is the wavelength of the laser light (in the VCSEL case, 0.850 μm).

$$I_1(\delta z_1) = I_1^+ + I_1^- \cos\left[4\pi \frac{d_1}{\lambda}\left(1 - \frac{\delta z_1}{d_1}\right)\right]. \tag{9}$$

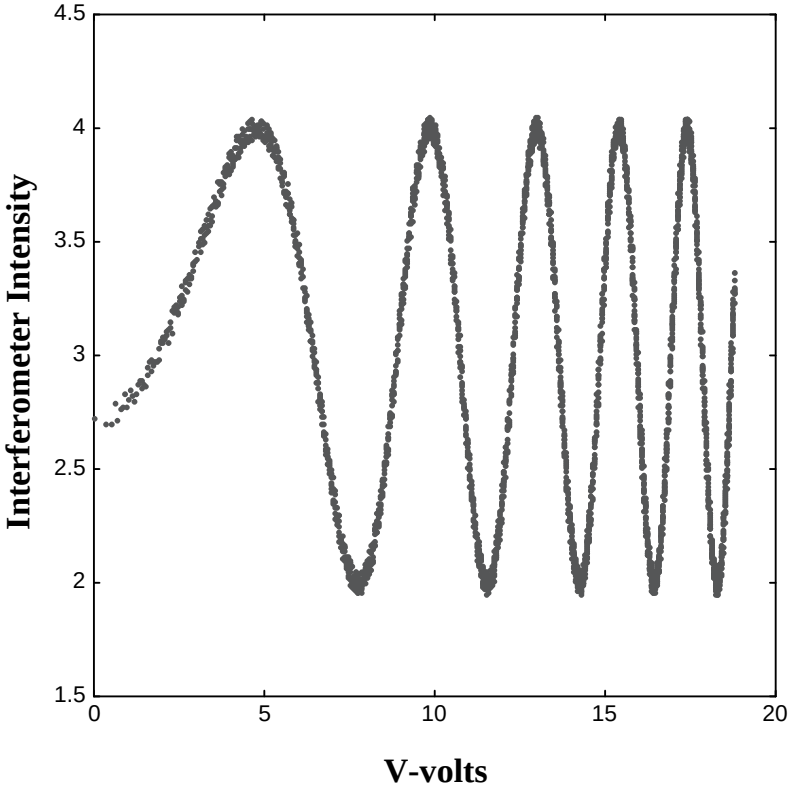

Figure 6-6. The interference pattern obtained experimentally by recording the pattern as the applied voltage is scanned to near the point of instability.

In turn, this pattern can be placed in terms of intensity as a function of the change in gap spacing by solving Equation 9 in terms of actual changes in gap spacing (d_1-δz_1). This relationship is given as,

$$d_1 - \delta z_1 = \frac{1}{2\pi}\left(\frac{\lambda}{2}\right)\cos^{-1}\left[\left(\frac{I_1(\delta z_1) - I_1^+}{I_1^-}\right)\right], \tag{10}$$

and a plot is shown in Figure 6-7. This data clearly shows, for this sensor, that the full range of stable voltage resulted in a top-plate displacement of 2.167 μm. However, it is known that the stable range involves a displacement of $1/3d_1$. Thus, d_1 is calculated to be 3 times the measured displacement from Figure 6-7 or a value of 6.5 μm. Therefore, the only unknowns left are the spring constant and the effective area of the capacitors.

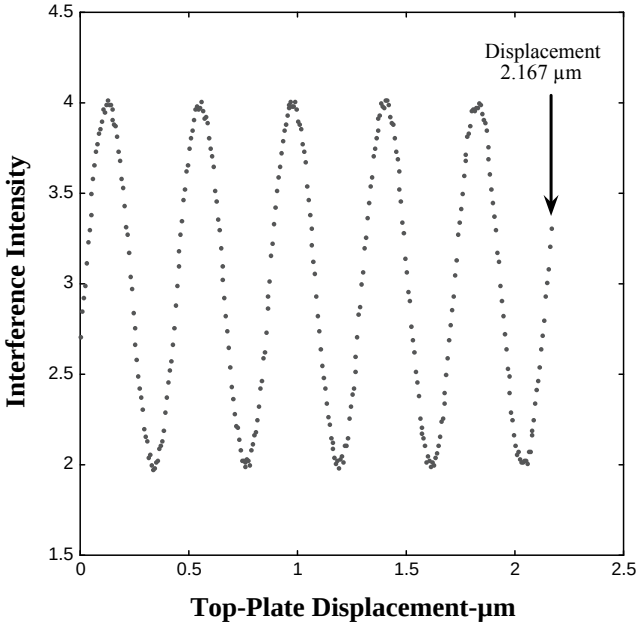

Figure 6-7. Result of Eq. (5) applied to the data of Figure 6-6, indicating the actual displacement during the voltage sweep.

As mentioned above, to obtain the area value at the present prototype stage, two accurate constant-current sources are used to independently drive the capacitor pads. From the basic formula relating the applied voltage to the resulting capacitance charge, i.e., Q=CV, we can measure the capacitance by noting that, for the constant-current case,

$$C(V) = \frac{dQ}{dV} = i / \frac{dV}{dt} . \tag{11}$$

The result for the measured capacitor voltage as a function of time under a constant current is shown in Figure 6-8, where the increase in slope at the higher voltages indicates that the capacitance increases towards its 50% limit over its stable region. The area value can now be calculated from the relationship,

$$C_1 = \frac{\varepsilon_0 A_1}{d_1}, \tag{12}$$

which leads to a value of 6×10^6 μm^2, very close to the design value of $6.4\text{x}10^6$ μm^2.

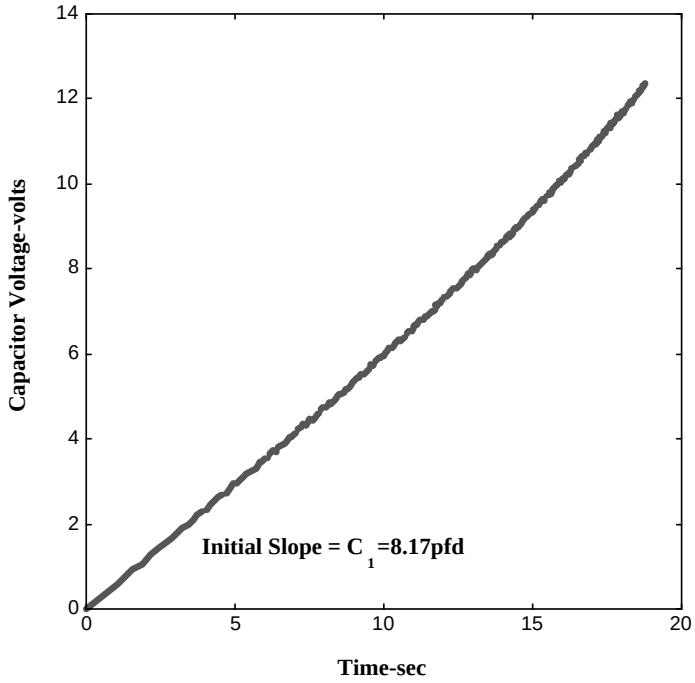

Figure 6-8. The voltage across one of the sensor capacitors as a function of time with the capacitor fed by a 70 pA constant-current circuit. The slope of this result measures the capacitance value at each time.

The procedure outlined above for the double laser-interferometer IFM system will be performed periodically. The procedure will be performed automatically prior to, and occasionally during, a particular set of experiments, thus giving rise to a totally self-calibrating sensor system.

6.4 MEMS Test Instrument: Prototype Development

In addition to these developments in sensor design and implementation, we are also accumulating components that allow the rapid and precise location of desired test points for individual components over a very broad lateral range. A photograph of the status of the system is illustrated in Figure 6-9, which shows the basic components. A 300× optical microscope provides coarse location of the desired point on the particular component to be analyzed. The IFM head is to the right of the scope and is separated by a known distance. This allows the sample to be translated by that distance for coarse-point tip alignment. The tip is then brought into near contact with the component and an adaptive x-y constant-force image is taken to locate the tip precisely at the desired diagnostic position. Once this point has been established, it will be possible, in conjunction with an engineering drawing of the die or wafer, to move to the next component under system computer control. The coarse and fine metrology tables allowing this operation are remarkably accurate over broad x-y-z ranges.

This capability will allow the rapid characterization of individual MEMS devices, e.g., shock-switch components, over an entire die or a significant portion of a full wafer containing the components. Such information is not now available for the characterization of the lateral forces and displacements in any MEMS device. This information provides feedback for verifying

design parameters, for qualifying MEMS components, and for locating failed sub-units in a MEMS device.

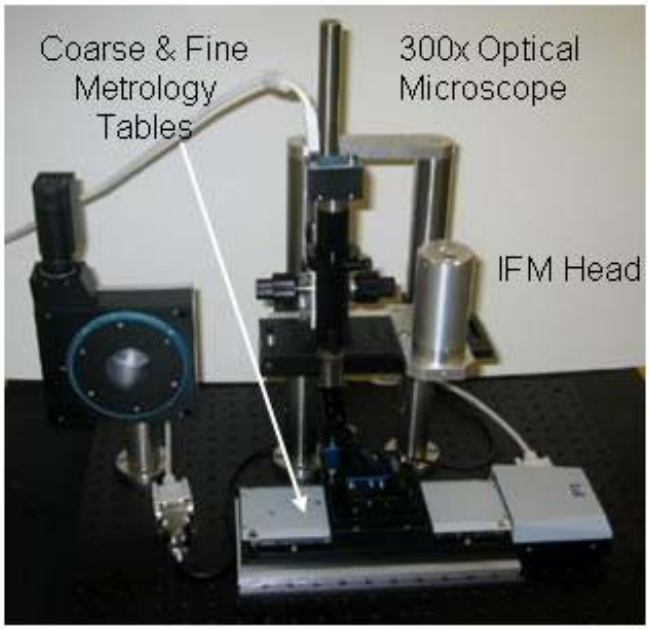

Figure 6-9. The basic units necessary for implementing IFM metrology over many individual components on a MEMS die or large portions of a full wafer.

The one remaining feature that is necessary for such lateral force or displacement metrology is a properly designed IFM tip that is strong enough to withstand the range of lateral forces encountered in MEMS components and is shaped appropriately to make lateral force measurements under tight confinement. Such a tip is illustrated in Figure 6-10. This tip begins with a conically ground diamond end form mounted on a small stainless-steel rod (commercially available). The tip is then FIB (focused ion beam) etched to the desired shape and mounted on the IFM sensor.

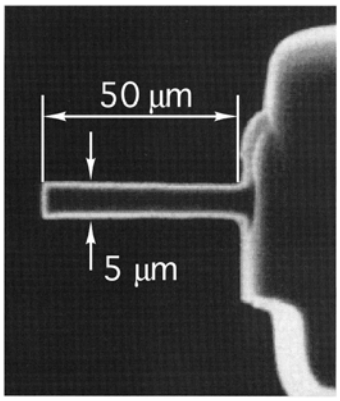

Figure 6-10. Illustration of a fib-shaped diamond tip for use in MEMS metrology applications.

7. PASSIVE SHOCK SENSOR FAILURE ANALYSIS

Failure analysis and device characterization were used to identify failure mechanisms found during packaging of the passive shock sensor switch (PSS). Analysis identified two types of failures. These were electrically shorted and electrically open. On packaged devices with electrical shorts, PSS devices were tested after packaging and lid sealing as well as after lid removal. Lid removal was performed to gain access to and structurally analyze the PSS devices. An example of the PSS component at the board and package levels is shown in Figure 7-1.

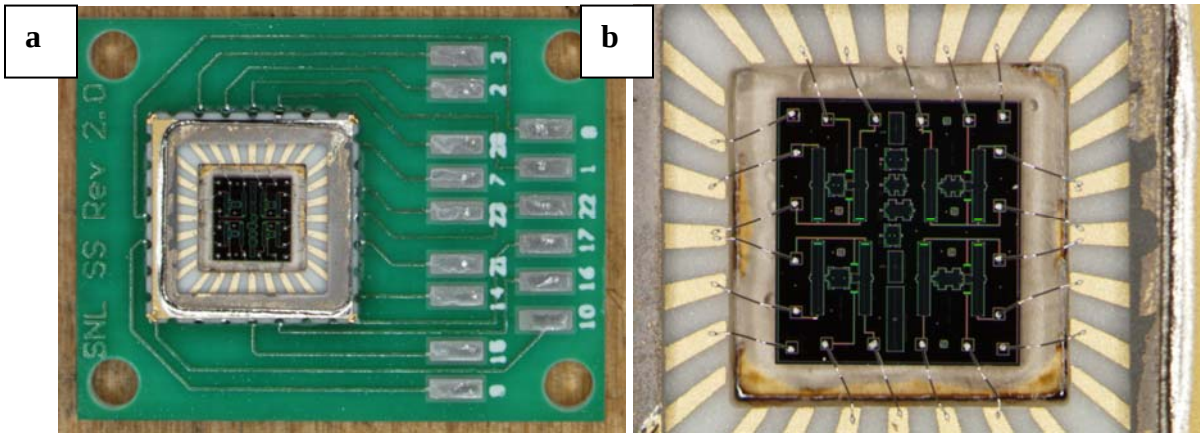

Figure 7-1. a) PSS device mounted on a board and b) LCC packaged PSS device.

7.1 Shorting Failures

Electrically shorted PSS components brought in for failure analysis were hermetically packaged in an LCC and were not mounted on a board. Two packages analyzed had ids S12 and S13. Optical inspection of the packages identified various particles on the power lines and bond pads. An example of particle contamination on a power line (package S12) and bond pad (package S13) are shown in Figure 7-2.

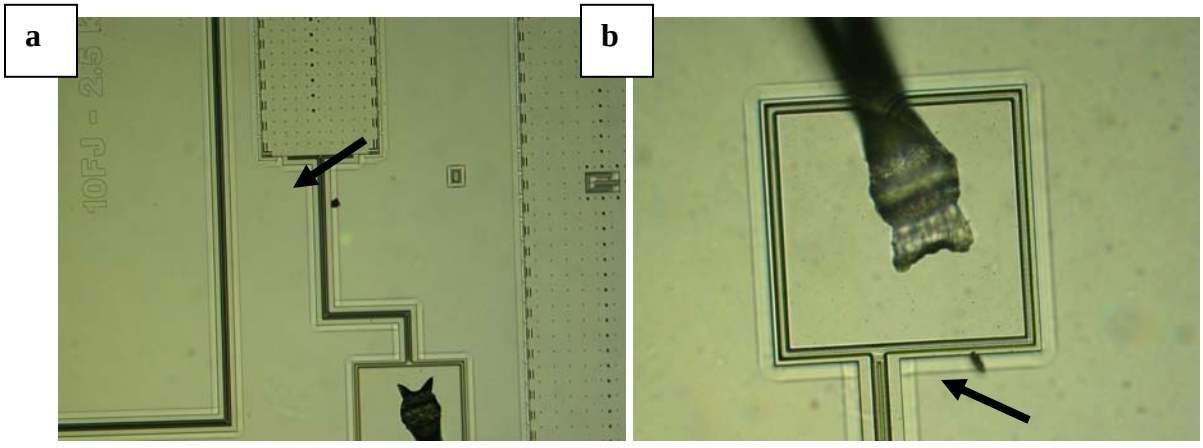

Figure 7-2. a) particle located on a power trace (package S12) and b) particle on a bond pad (package S13).

Thermally Induced Voltage Alteration (TIVA) analysis was performed on these devices to identify the location of electrical shorts. The physics of TIVA [9] for integrated-circuit (IC) examination employs the constant-current biasing method used in Charge-Induced Voltage Alteration (CIVA) [10] and Light-Induced Voltage Alteration (LIVA) [11]. The constant-current biasing approach provides an extremely sensitive method for detection of subtle changes in the IC or MEMS power demand. In TIVA, localized heating changes the resistance of a short, and the effects of this resistance change on the power demands of the entire IC are used to produce an image. Power consumption of a short will depend upon the resistance of the short and its location in the IC. For example, a V_{DD} (power) to V_{SS} (ground) short may dissipate more power than a short between two signal lines. If the short is of a metallic nature, the increase in temperature increases the resistance of the short, thereby reducing the power demands of the IC. The change in resistance of a short with heating from the scanned laser can be expressed by Equation 13 [12]:

$$\rho = \rho_0 (1 + \alpha(T-T_0)), \tag{13}$$

where ρ is the resistivity of the short, ρ_0 is the resistivity of the short at T_0, α is the temperature coefficient of resistivity, T is the temperature, and T_0 is the steady-state or reference temperature. When the region of interest is "heated", localized temperature variations of 5 – 50^{o}C are realized. MEMS components often get hotter than their IC counterparts (using the same laser power) due to their thermally isolated nature. MEMS structures are typically surrounded by silicon nitride, silicon oxide, or air. Therefore less laser power can be used when performing TIVA analysis on a MEMS component. A schematic of a TIVA setup is shown in Figure 7-3 where the device under test (DUT) is the MEMS component. For simple powering procedures, the switch matrix can be replaced with either probes or a switch box.

When localizing shorts in signal lines, the IC must be biased (statically) with sufficient potential to "activate" the short. For a 3-V IC, the constant current should be elevated to achieve a voltage of 2.5 to 3 V. The thermally-induced resistance changes alter the voltage of transistor gates driven by the shorted conductors, producing the same amplification effects seen in CIVA.

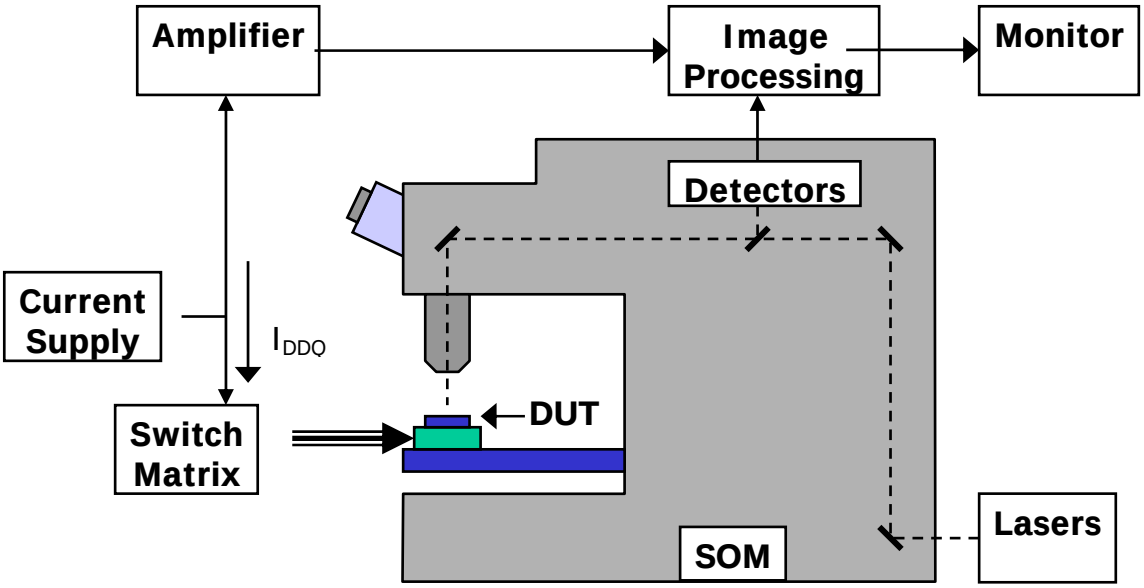

Figure 7-3. Schematic representation of a TIVA system using a scanning optical microscope (SOM).

If the short is between power buses, then only a minimal current (100 μA to 1 mA) is required through the short while imaging. The voltage obtained may be well below the normal operating potential. Under these conditions, there is no TIVA-like amplification by transistor gates, but neither is there any background power consumption due to biasing the entire IC that can mask weaker signals. The resulting sensitivity in detecting shorts is generally better for power-bus cases than signal lines, but specific cases vary in sensitivity. For some shorts, no applied current is necessary because the heated short produces its own bias via a thermocouple effect. Certainly the setup is much easier for "hard" shorts where no bias is applied. Also, because no bias is applied the risk of further damage through biasing is circumvented. A schematic illustrating the TIVA technique (using a 1064 nm laser) employed on a particle-induced short over two conductive lines is shown in Figure 7-4.

The resistance change with localized heating in TIVA is the basis of the optical-beam induced resistance change (OBIRCH) technique [13]. For OBIRCH, the change in IC power consumption is detected by an IC current change with constant-voltage biasing, yielding limited detection sensitivity. The constant-current biasing approach used in TIVA produces greater sensitivity in localizing shorts. OBIRCH using constant-current biasing was mentioned in a recent review article [14], which also indicated the improved sensitivity seen with the "IVA" techniques.

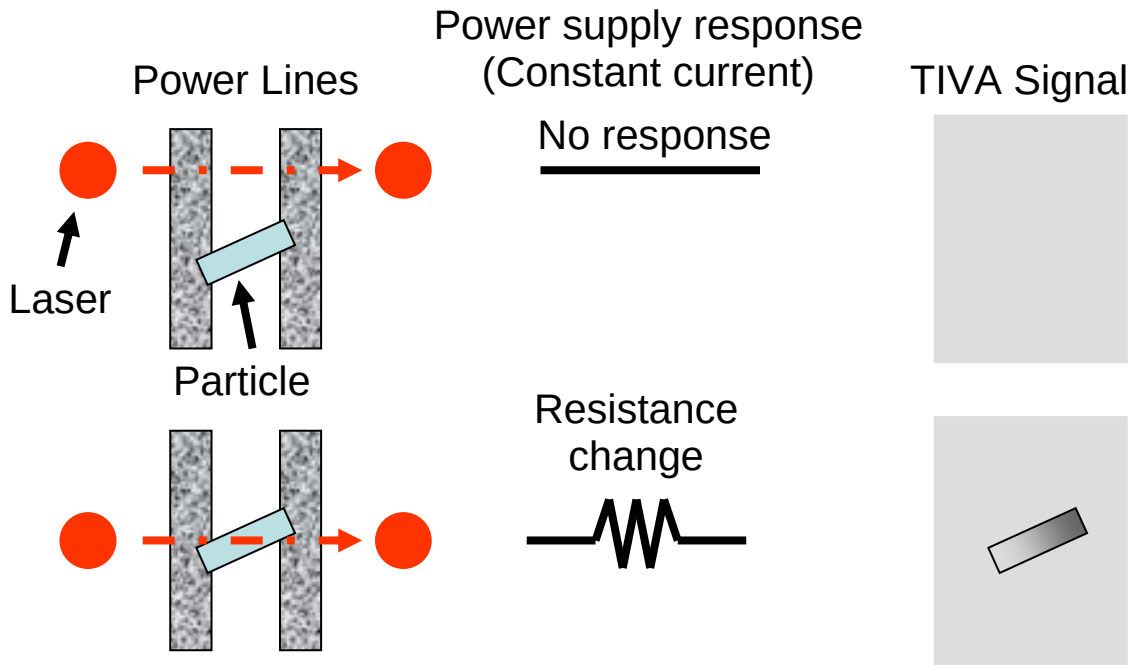

Figure 7-4. Schematic of the TIVA technique employed across two conductive lines. Note the response (lack thereof) of the laser scanned over power lines in the region outside of the particle versus the response of the laser scanned over the particle causing a short.

Application of TIVA to MEMS presents some special opportunities. Because some MEMS structures are thermally isolated from the substrate of the MEMS device, the structures can be heated easily with much lower power than when TIVA is applied to ICs [15]. In fact, some devices require care to avoid overheating and possible damage to the MEMS structure by high temperature alteration of the thermally isolated components. Additionally, a number of MEMS devices do not have active IC structures, i.e., Si diffusions. With these structures there is no concern of photocurrent effects swamping out the TIVA signals. Therefore, shorter-wavelength lasers with better spatial resolution can be used for TIVA images. The improved spatial resolution can also be seen in the reflected light images used for registration.

On the PSS component, we immediately identified regions of interest where particles were observed in proximity to power lines and performed the TIVA analysis in those regions. As shown in Figure 7-5, we found that the particle is conductive and responsible for the shorts across pins 7 and 8 on packaged PSS component S12. This short was identified rather quickly since the particle was identified via optical inspection. One shortcoming of this technique on MEMS structures in general is the inability to analyze mechanical structures underneath metalized polysilicon. In the PSS component, thermal actuators, latching mechanisms, and a proof mass are fabricated in poly layers 1, 2, and 3. The poly 4 layer is used as a cover plate and acts as a shadow mask to prevent deposition on these components. One way to remedy this is to perform TIVA (and structural analysis) through the bulk silicon substrate and die.

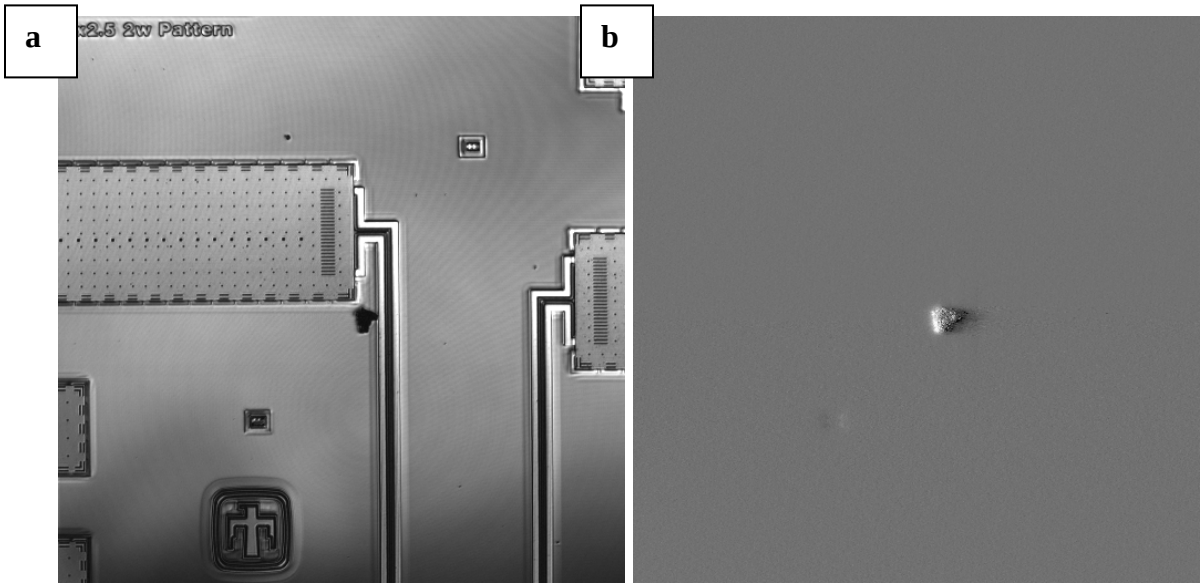

Figure 7-5. a) Reflected light image of a particle on a power line, b) TIVA image identifying the particle as the cause of shorting.

SEM analysis and inspection was performed to characterize the particles identified via optical inspection. Closer view of the particles clearly shows they are contacting powered portions of the die and ground. Although no elemental analysis was performed on the particle itself, it is evident that many of the particles are bridging the power lines to ground plane and bond pad to ground plane. SEM also identified fractured bond pads and broken traces which result in metal coated particles being dispersed throughout the die or package. It is not clear whether particles generated from fractured bond pads and/or traces is the origin of the particles, but they do pose a potential reliability concern in particle shift or movement either during packaging, assembly, testing, or field operation. Examples of damage and particles inducing shorts and more are shown in Figure 7-6.

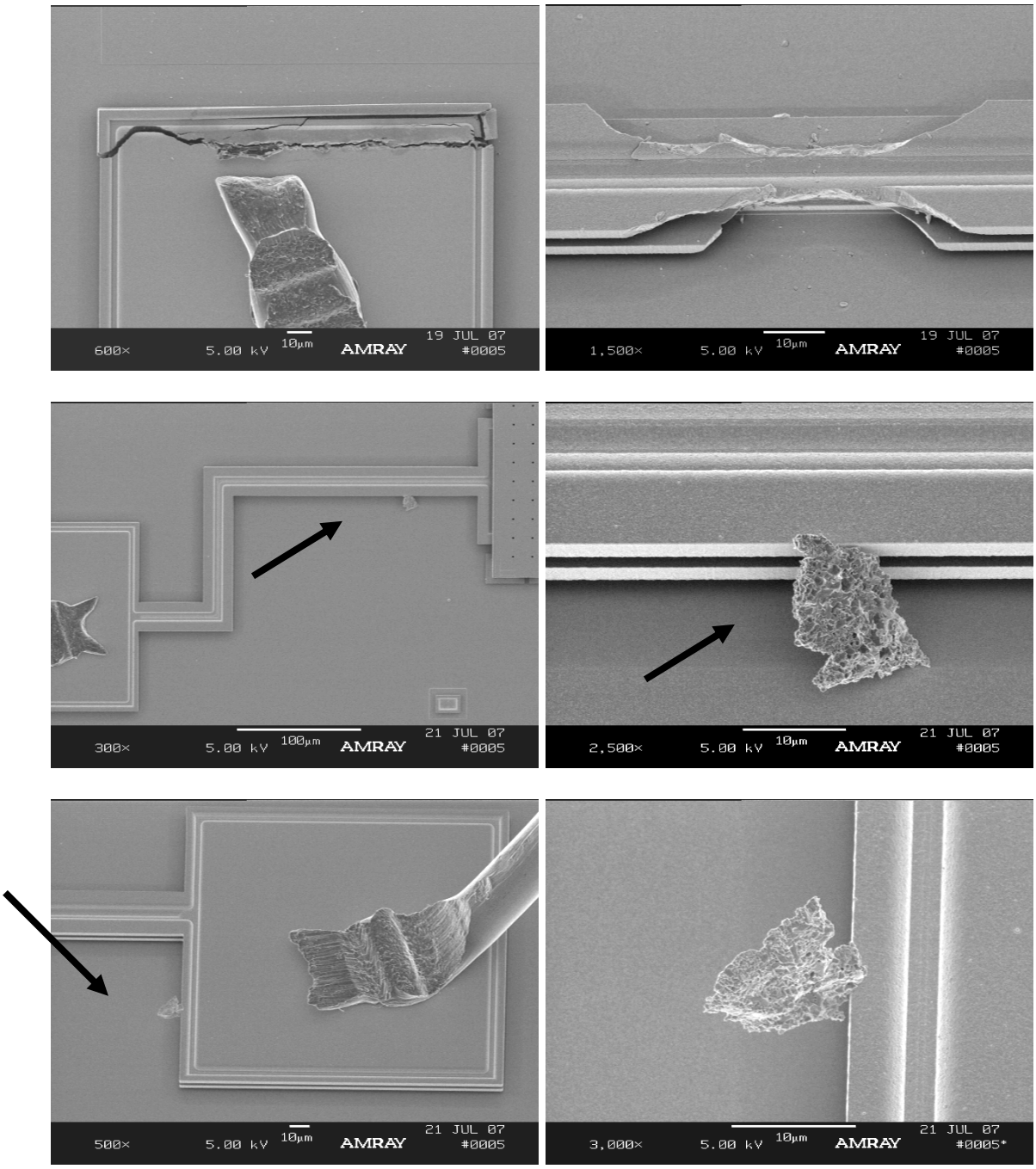

Figure 7-6. SEM images identifying bond pad and trace cracks/fractures and particle contamination along power lines and bond pads leading to shorts.

7.2 Open Failures

Open failures were identified after packaging using JM 7000 and a special thermoplastic compound (both cases are different approaches to die attach). JM 7000 was packaged using a 24-hour cure and 24-hour post bake. After the bake cycle, the parts were immediately lid sealed and tested 24 hours later. After testing, the parts were identified as failing via stuck open.

Optical inspection identified a spring pulled back further than its as-fabricated rest position. This feature was identified in both the JM 7000 packaged components (24-hour cure and 24-hour post bake) and the thermoplastic packaged sample. Examples of an open PSS component packaged using the thermoplastic material is shown in Figure 7-7. Optical inspection of the stuck JM 7000 packaged device has the same signature.

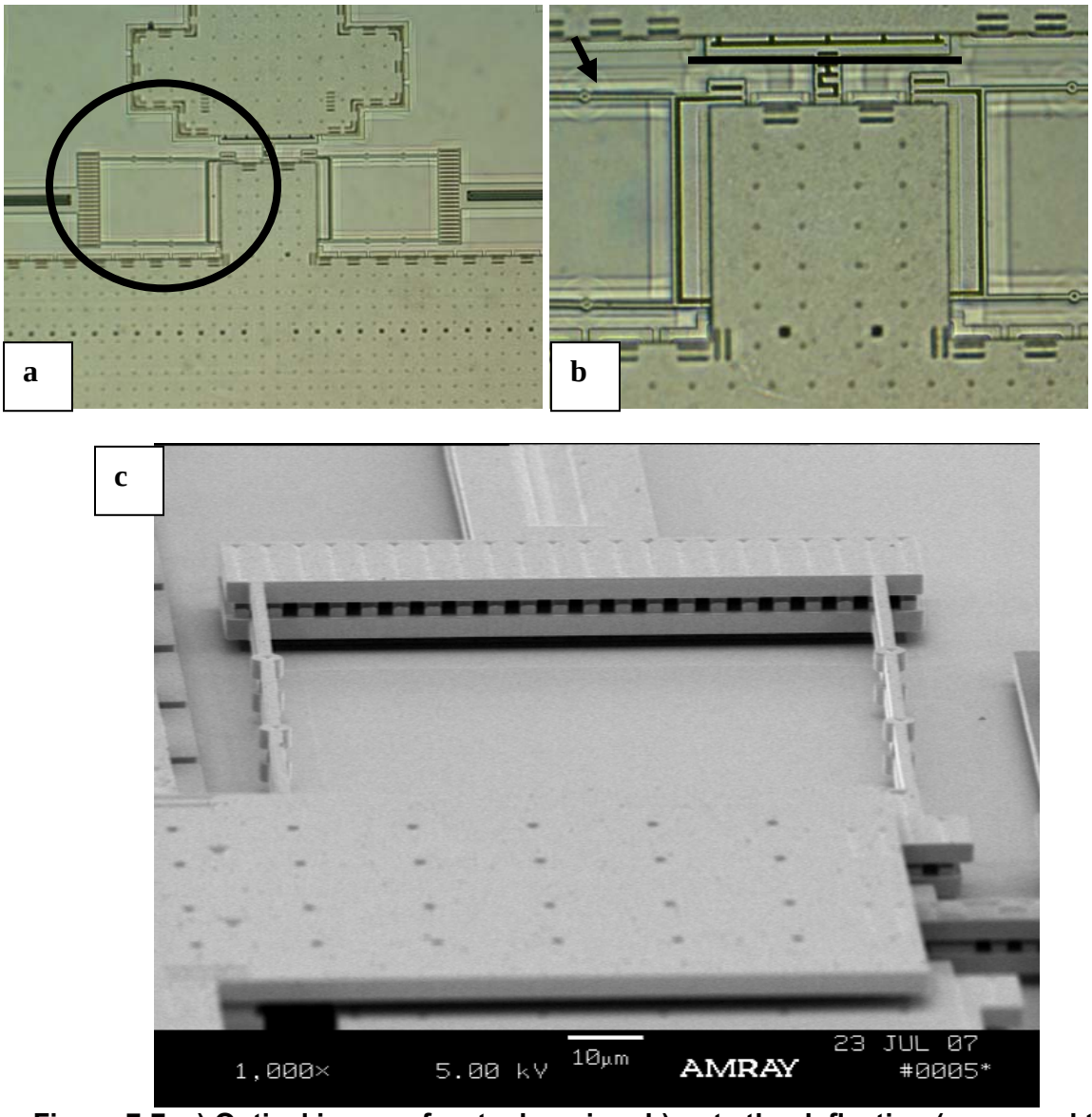

Figure 7-7. a) Optical image of a stuck spring; b) note the deflection (compared to the right spring) is not in the as-fabricated position; c) SEM image of the deflected spring.

Discussions of testing and actuation revealed potential paths to ground on the stuck spring. It was deduced that when the spring comes in contact with the thermal actuator, some current or voltage may leak into the spring and travel to ground resulting in a "resistive" short. As shown in Figure 7-8, if the device shorts during test, this may result in a weld between the spring and the thermal actuator. A laser-cutting tool was used to analyze that section of the device. The tool

was used to cut through strategic points along the poly 4 cap, and a probe with adhesive material was used to remove the laser cut portion.

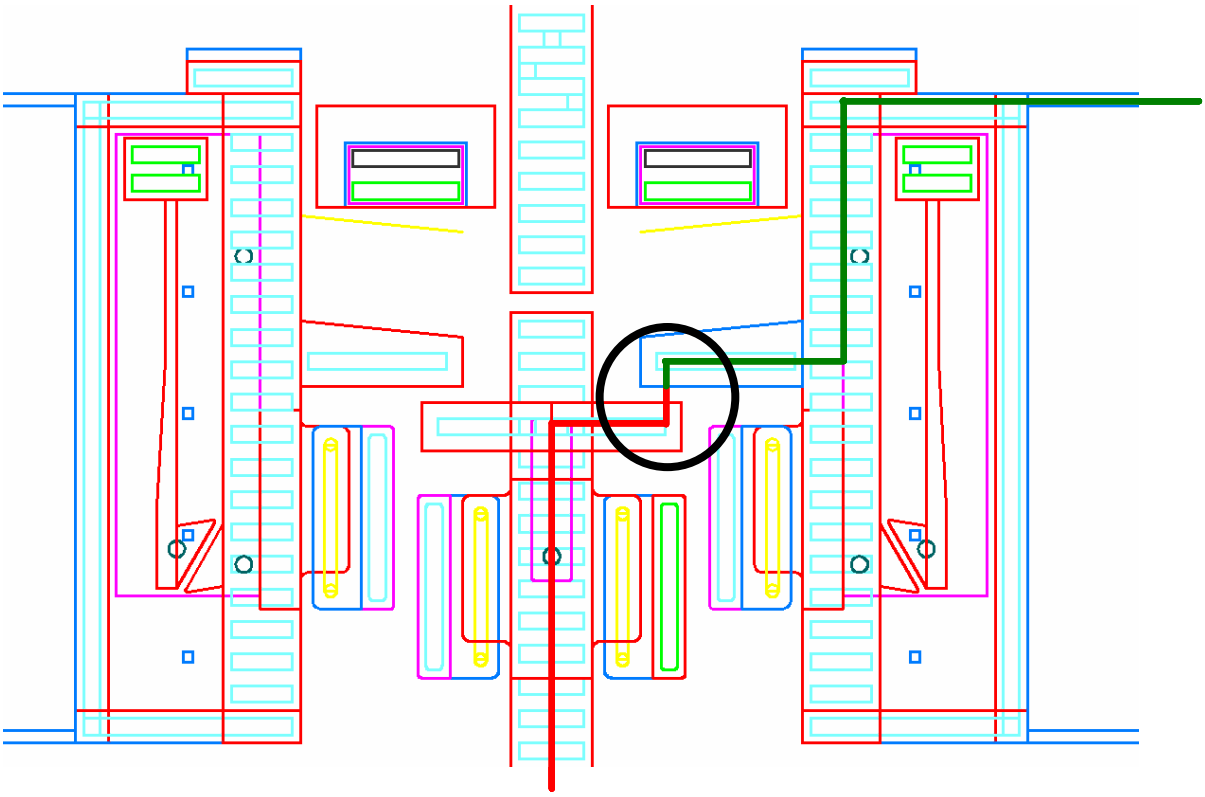

Figure 7-8. AutoCAD schematic illustrating contact between the thermal actuator and the spring (circle) can introduce a path to ground during testing. Path to ground shown in red and green lines.

After removal of the laser-cut portion of the poly 4 cap, SEM examinations of the thermal actuator and spring elements were performed. This analysis was performed on the JM 7000 packaged part and the thermoplastic packaged part. Analysis of the JM 7000 part did not reveal any stuck or welded structures. However, these parts were identified as having a "weak" adhesion between the spring and the thermal actuator. In many cases, when the lid was removed from the package the parts began to function properly. In the case of the thermoplastic, when the poly 4 cap was removed, it was possible to identify a weld site between the thermal actuator and the spring. As shown in Figure 7-9, a portion of the poly 1&2 layer of the thermal actuator is adhered to the spring. During removal of the poly 4 cap, the thermal actuator fractured but a significant portion of the thermal actuator was still adhered to the spring indicating strong adhesion between the two mechanical elements.

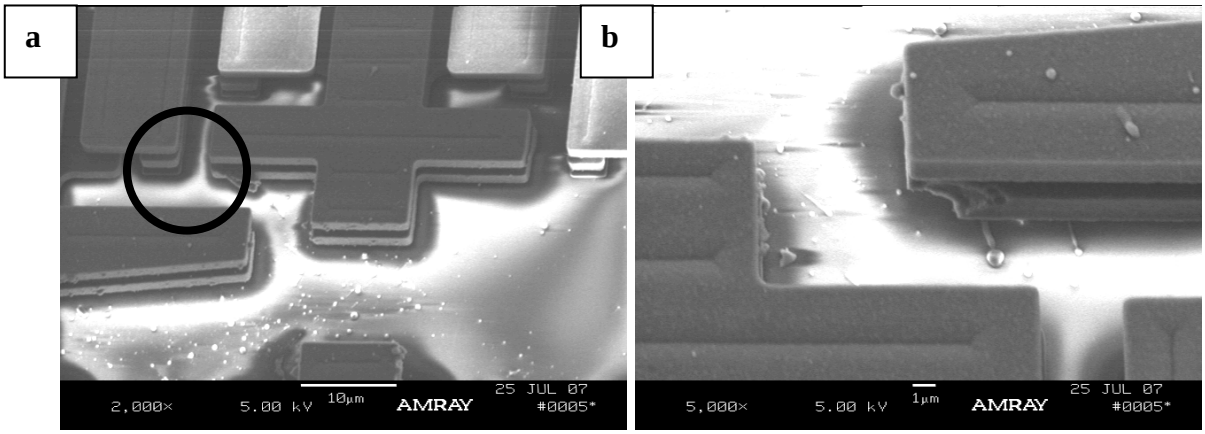

Figure 7-9. a) Removed poly 4 cap revealed a portion of the spring attached to the thermal actuator (circled region); b) Analysis of view from opposite side shows a fractured, missing portion of the thermal actuator.

Many devices that failed in an open state when packaged functioned properly when the lid was removed. Analysis of these packaged components did not identify any sticking sites along the springs. In these failures, slight overdriving of the thermal actuator would cause the device to latch and function properly. These results are indicative of sticking behavior between the thermal actuator and springs. If these elements stick during operation, retraction of the thermal actuator will retract the springs unless they are latched.

8. PACKAGING

8.1 Background and Motivations

This chapter of the report describes FY07 packaging activities. The focus here is on the following basic packaging steps:

- Hermetic packaging: selection of die or chip carrier, die attach, wire bonding, and lid seal
- System level or customer integration: housing design that facilitates customer integration and addresses how the customer will integrate the shock sensor, including mechanical and electrical integration.

First, a general overview will be given showing the package type selected, the PCB used, and the metal housing designs that were explored. Then a detailed process description will be provided for the final Revision 2 packaging and integration approach. A flow-chart outlining this process is shown in Figure 8-1; it will be explained in detail in Section 8.2.3.2.

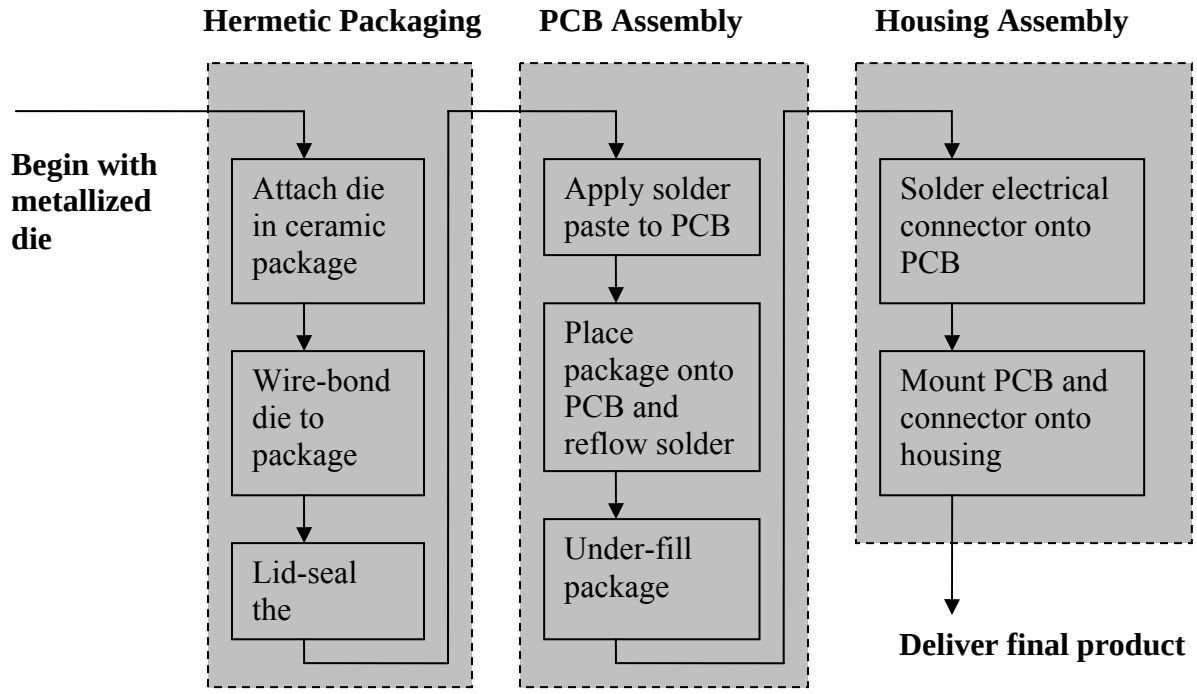

Figure 8-1. Flow-chart outlining the basic packaging steps.

For FY07, our packaging goals were to

- Package a sufficient number of devices in order to test, characterize, and verify customer-centric features (see Section 2.1).
- Explore and trade off packaging solutions for die-level hermetic packaging and system-level mechanical and electrical integration.

In order to meet the packaging goals outlined above, several requirements were outlined by the team for the packaged solution this year. The integrated package should

- Provide a clean hermetic environment for the MEMS die to ensure that the die is protected and to improve the contact performance and reliability.
- Have bolt holes for easy mechanical attachment to a test fixture or experiment.
- Use a connector for easy electrical interfacing. This would allow us to change pin-outs in a ceramic package or modify any mounting printed circuit boards, without affecting the customer interfacing electronics because the connector pin-outs could be held constant.
- Survive over-shock events up to 50,000 g's.
- Provide for transmission of shock to the MEMS die. Specifically, the methods used to attach the die inside a package, and to attach the package to the test fixture should not in and of themselves attenuate the incoming shock pulse to a large degree.
- Be able to be reasonably manufactured in a quantity of up to 100 parts this year.

To meet these requirements we have selected a general packaging and integration approach that utilizes a commercial off-the-shelf ceramic leadless chip carrier (LCC) to hermetically seal the MEMS die. This LCC is then soldered to a printed circuit board (PCB), which provides for an electrical interface to the LCC and for attachment of an electrical connector. The PCB is then attached to an aluminum housing which contains bolt holes for mechanical attachment to the test fixture and provides a way of securing the electrical connector. The variations of this general approach that were explored will be discussed.

8.2 Prototypes and Concepts

To identify trade-offs and challenges for the final integrated package, several different prototype packages were explored. These prototypes will be described in the following sections.

8.2.1 Hermetic Package Selection

Two different commercial off-the-shelf ceramic packages were selected. The first was chosen for any devices packaged using Revision 1 die, and the second was chosen for die Revision 2. The die size was reduced in Revision 2 compared to the Revision 1 design, and the LCC package was selected in each case to be as small as reasonable and still allow for the die size and necessary number of wires. In both cases the LCC selected was from Spectrum Semiconductors LLC (www.spectrum-semi.com). The Revision 1 package was model number SSM LCC02854and the Revision 2 package was model number SSM LCC02801. Key dimensions and parameters are listed in Table 8-1, with pictures of each package shown in Figure 8-2.

Table 8-1. List of Packages and Key Parameters

Parameter	SSM LCC02854	SSM LCC02801
Lead count	**28**	**28**
Cavity Size (W)	**0.190**	**0.163**
Cavity Size (L)	**0.361**	**0.163**
Package Size (L)	**0.550**	**0.325**
Package Size (W)	**0.358**	**0.325**
Cavity depth	**0.035**	**0.045**
Thickness w/o lid	**0.055**	**0.065**
Manufacturer Drawing No.	**PB-C89129**	**PB-44608**
Recommended lid	**CL-533302**	**CL-27501**

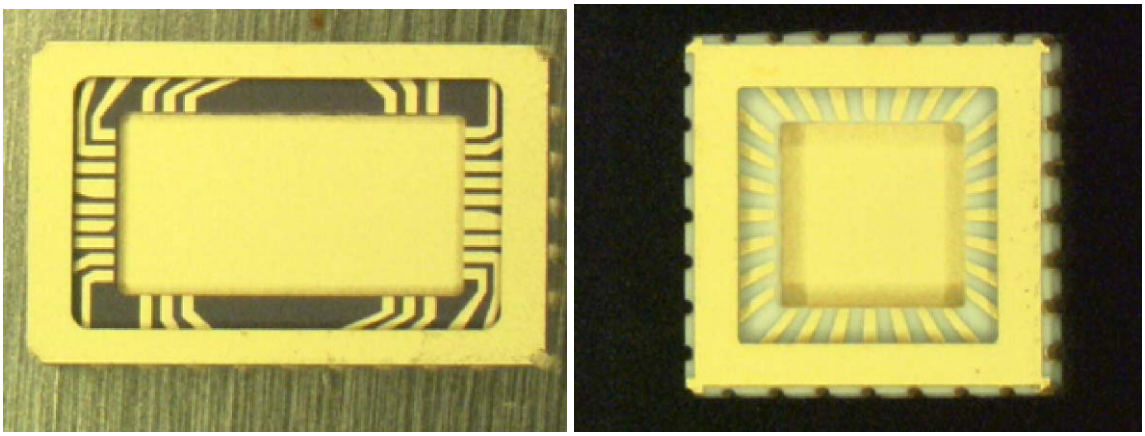

(a) **(b)**

Figure 8-2. A picture of the two ceramic leadless chip carriers used in FY07. (a) The larger package used for Revision 1 and (b) the smaller package used for Revision 2.

8.2.2 Printed Circuit Board Design

The printed-circuit board (PCB) serves two purposes. It is used to provide electrical connections between the LCC and the electrical connector, and it provides a means to mechanically attach the LCC onto the metal housing. A separate PCB was designed for each of the two packages. In each case it provides a solder pad for each required pin on the package, and solder points for the wires leading to the electrical connector. Examples are shown in Figure 8-3.

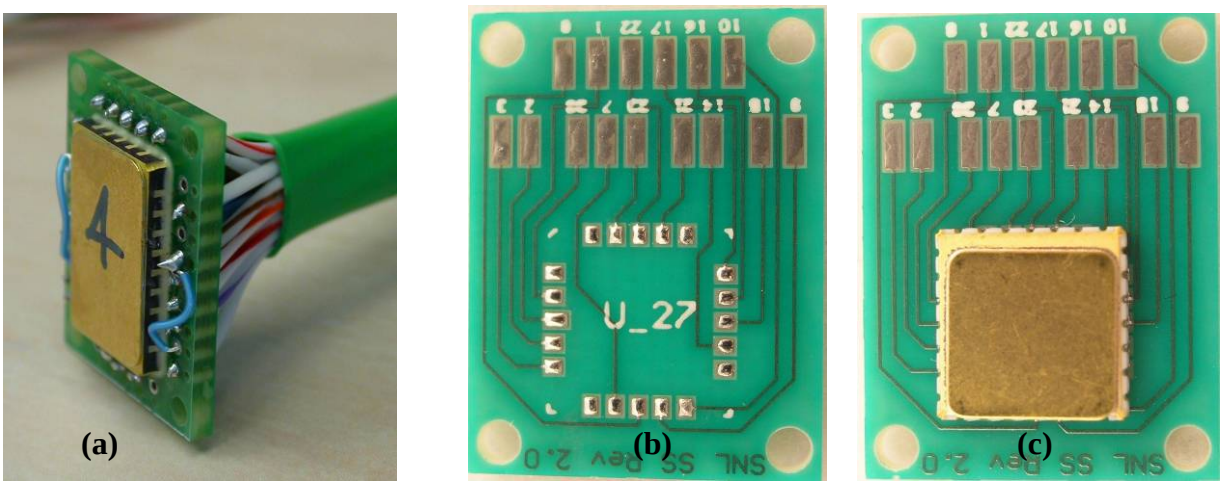

(a) **(b)** **(c)**

Figure 8-3. Pictures of the printed circuit board designs used in FY07: (a) Revision 1 design with attached LCC and wires, (b) Revision 2 design by itself, and (c) Revision 2 design with an attached LCC.

In the Revision 1 PCB design, the connector wires are soldered into thru-holes, as this was the method required for use with the Revision 1 housing. The Revision 2 housing required surface-

mount connections for the electrical connector wires, and includes thru-holes only for mechanically bolting the PCB onto the housing. This design trade-off will be made clear in Section 8.2.3.

8.2.3 Housing Designs

The most challenging aspect of the package design was the metal housing. It must provide a means for securing the PCB and electrical connector that can transmit shock events to the die with little attenuation, yet be robust to over-shock events of up to 50,000 g's. The metal housing must also include bolt holes for easy mounting to a test fixture.

8.2.3.1 Revision 1 Housing Designs

Two different housing designs were explored for the Revision 1 package. The first, referred to as the "block" is shown schematically in Figure 8-4, with a photo shown in Figure 8-5.

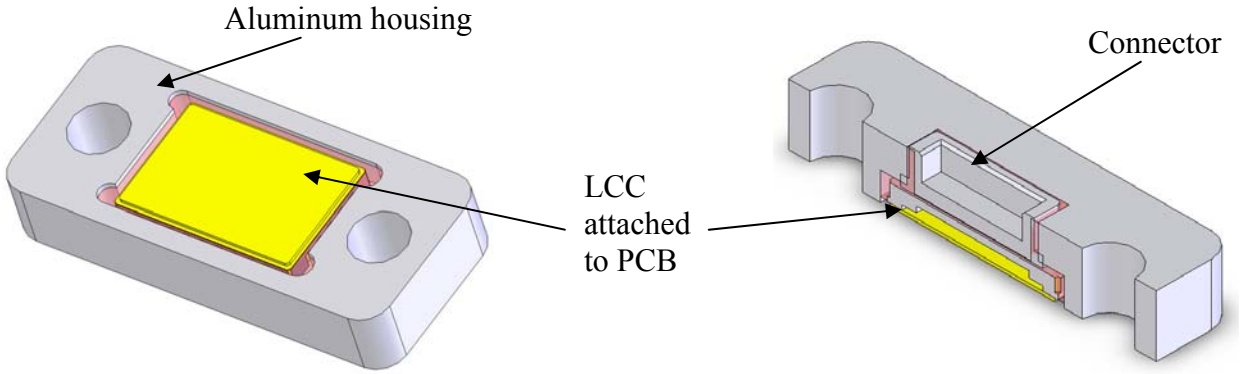

Figure 8-4. Drawing of Revision 1 "brick" packaging solution.

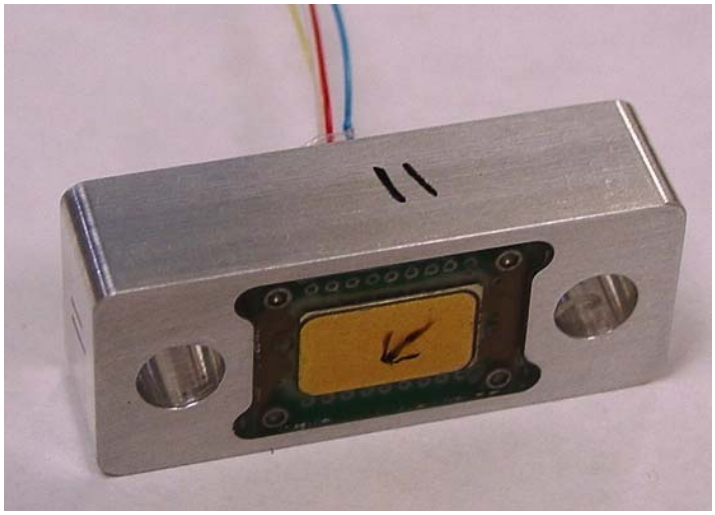

Figure 8-5. Picture of Revision 1 "brick" design.

The cavity inside the aluminum housing is machined so that the PCB can be bolted in and the wires attached to an electrical connector on the top side of the housing. The void with the wires, PCB, and LCC package is then filled with an epoxy such that the entire brick is solidly potted with no air voids. This allows for shock to transmit easily into the package and hardens the structure against over-shock. This packaging approach worked well; however, the housing design was expensive to machine and was difficult to assemble properly as there was little space for wiring the connector. It also proved challenging to pot the void without forming air pockets.

A second approach, called the "plank" is shown in Figure 8-6. In this approach, the printed circuit board with the LCC attached is simply glued onto a flat aluminum rectangle. The adhesive used is a high-peel strength two-part epoxy typically used in the Sandia shock lab for shock testing. This approach is simple and much less expensive. However, there is some concern about the epoxy attenuating the shock pulse, as it is somewhat flexible when cured. Also, this approach does not lend itself well to the use of an electrical connector.

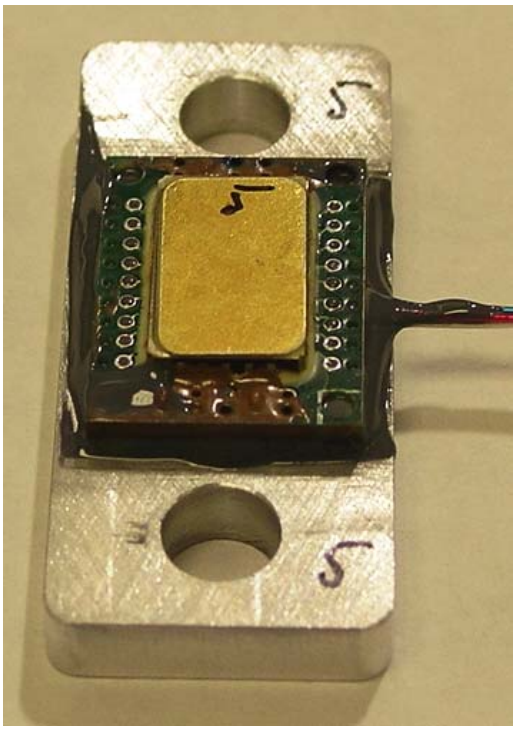

Figure 8-6. Picture of the "plank" approach for the rev 1 design.

Both of the packaging approaches were tested in shock up to 50,000 g's and showed no failure in the solder connections or wire-bond connections inside the LCC.

8.2.3.2 Revision 2 Housing Designs

For the Revision 2 device, a housing was designed that is an enhancement of the "plank" approach seen in Revision 1. The intent was to take advantage of the low cost and simplicity of using an epoxy to attach the PCB to the housing while also providing a means to secure an electrical connector to the housing. As an additional requirement, the housing needed to maintain the same footprint and bolt-hole spacings as the Revision 1 housings so that it would be interchangeable with existing test hardware.

Three designs were considered for the aluminum housing (see Figure 8-7). The final design was selected based on results from finite-element analysis (FEA) of the expected shock to the housing, and on housing manufacturability. Design (a) showed failure in the FEA shock modeling due to high stresses above yield. Designs (b) and (c) both showed acceptable stresses during high shock events in the FEA model. Design (b) is advantageous because it holds the connector in a vertical orientation for easier testing; however, design (c) was selected due to its lower cost of manufacturing and ease of assembly.

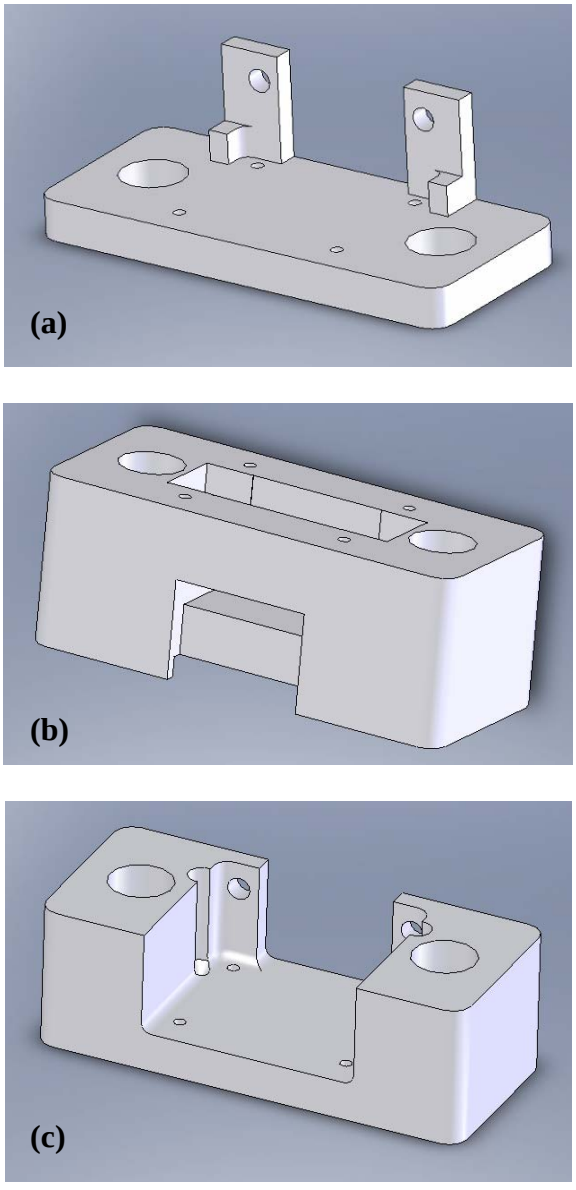

Figure 8-7. Three housing designs considered for Revision 2.

The housing was designed to work with a 15-pin metal mini D-sub connector, model ITT Cannon MDM 15PH006. The PCB is both bolted and glued (with epoxy) into the base of the

metal housing, and the connector is then bolted onto the mounting holes in the housing side. The final assembly is shown in Figure 8-8.

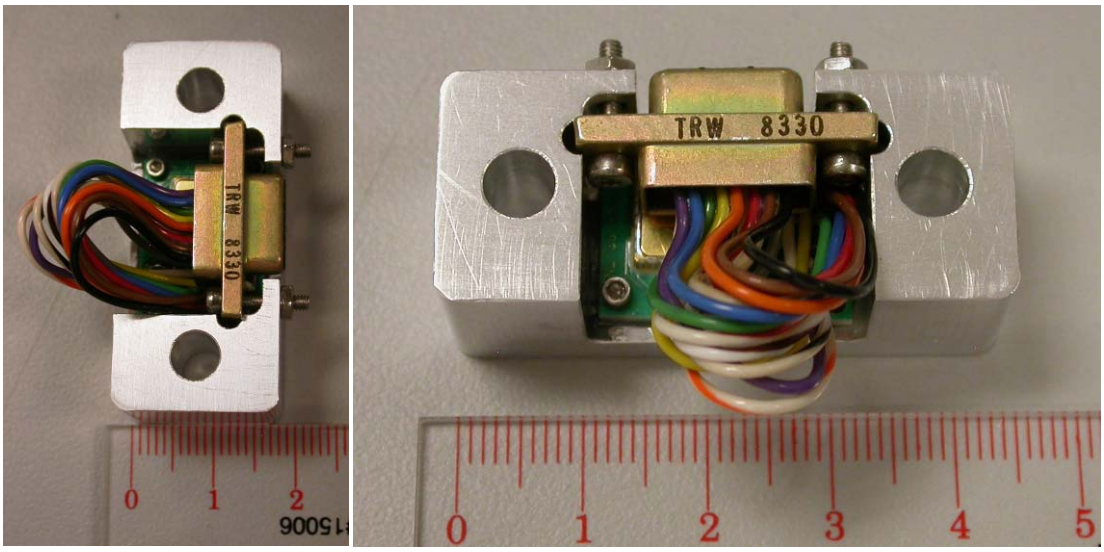

Figure 8-8. Final assembly of the Revision 2 device in the housing with the connector.

8.3 Final Revision 2 Package

The final package selected for delivery to customer demonstration test bed and for the series of functionality and environmental testing performed in FY07 is shown in Figure 8-8. It meets all of the requirements outlined in Section 8.1 and can be manufactured at a reasonable cost in the quantities required. The following sections will describe in detail the process used to prepare these packages from the hermetic die attach through final assembly. Much of the packaging steps could be considered standard practice in the industry, but are included in detail here for reference, and for the benefit of those readers not familiar with packaging technologies.

The complete packaging and assembly process can be broken down into the following steps:

- Hermetic packaging in leadless chip-carrier
  - Die Attach
  - Wire Bonding
  - Lid Seal
- LCC Assembly onto printed circuit board
  - Solder paste application
  - Package placement and solder reflow
  - Package under-fill
- Housing assembly
  - Electrical connector attachment
  - PCB attached to housing

These steps are described in detail in the following sections.

8.3.1 Hermetic Packaging in Leadless Chip-Carrier

The dice are received in the packaging lab after being metalized, and are stored in a Gel-Pak. When received, the batch of die is logged into a database used to track all packaging jobs, and a photograph is taken of each die to document the as-received condition.

8.3.1.1 Die Attach

The required number of empty LCC packages is removed from storage in a Nitrogen dry-box and placed on a ceramic plate for cleaning. To ensure good adhesion of the die-attach material to the package, all empty packages are cleaned in Argon plasma for 5 minutes at a power setting of 400 W. The Revision 2 LCC package is shown on this ceramic plate in Figure 8-9. During the plasma clean step any necessary epoxy die attach syringes are removed from the storage freezer to thaw before use.

Figure 8-9. Empty LCC packages on ceramic plate in preparation for plasma clean.

After the packages are cleaned, they are placed on a vacuum holding plate on the Palomar 3500-II, an automated pick-and-place tool with an epoxy dispense capability. The dice are then transferred using tweezers from the Gel-Pak to a waffle-pack in preparation for die placement inside the package. This is shown in Figure 8-10 and Figure 8-11, with labeling to identify the key parts of the Palomar tool. The Palomar is equipped with a vision system and pattern recognition software so it is able to automatically locate the die and packages, dispense epoxy into the packages if necessary, and place the die into the package (Figure 8-12). Epoxy is dispensed from a syringe controlled by the tool and the die are picked out of the waffle pack and placed in the packages using a vacuum pick-up tool (Figure 8-13). Exclusion areas on the die have been reserved for the vacuum pick-up tool so that it does not damage any structures fabricated on the die surface. Before real parts are operated on, a dry-run is always performed to ensure that the tool is functioning properly and that the correct program has been loaded.

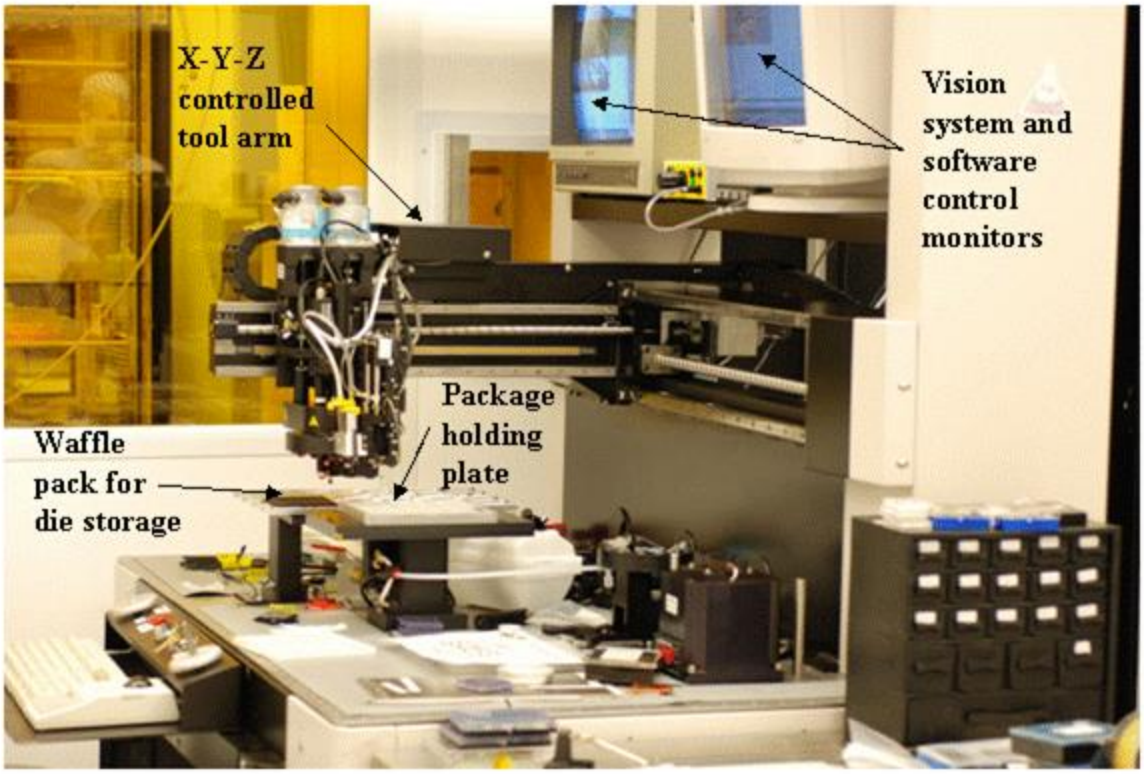

Figure 8-10. Palomar 3500-II epoxy dispense and pick-and-place tool.

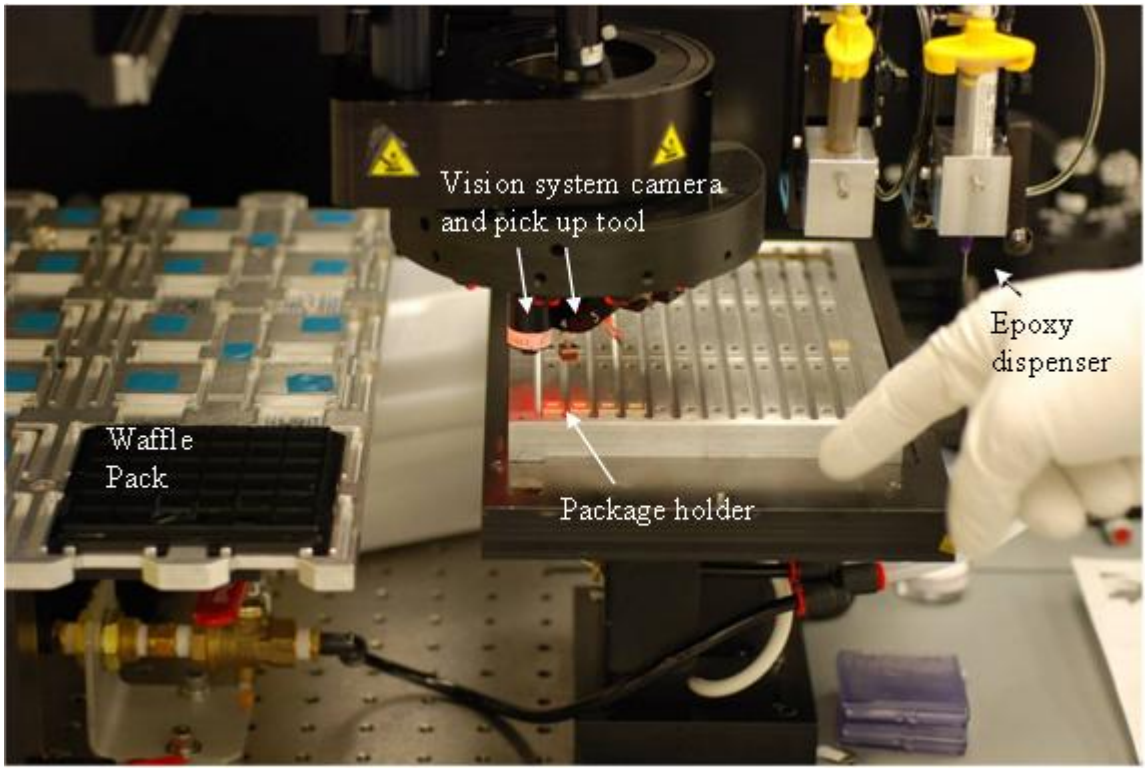

Figure 8-11. Zoomed-in view of tool head and work area.

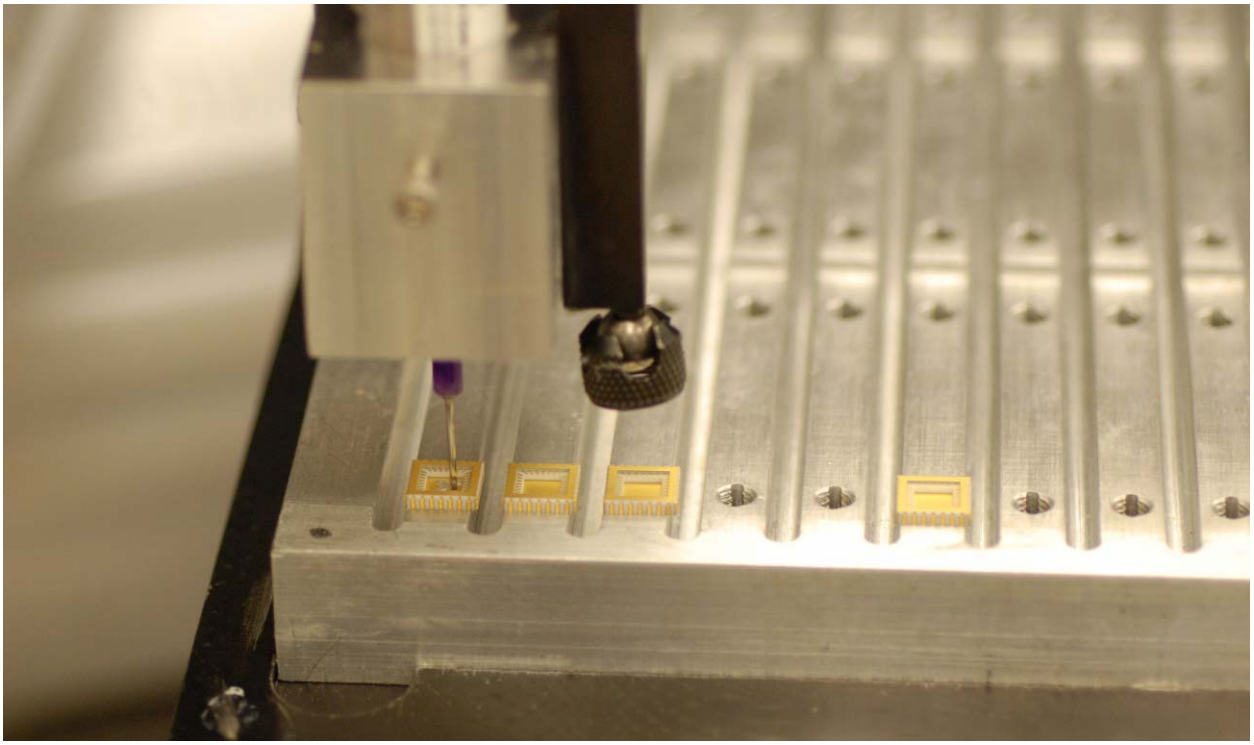

Figure 8-12. Photo showing Palomar tool dispensing epoxy into package.

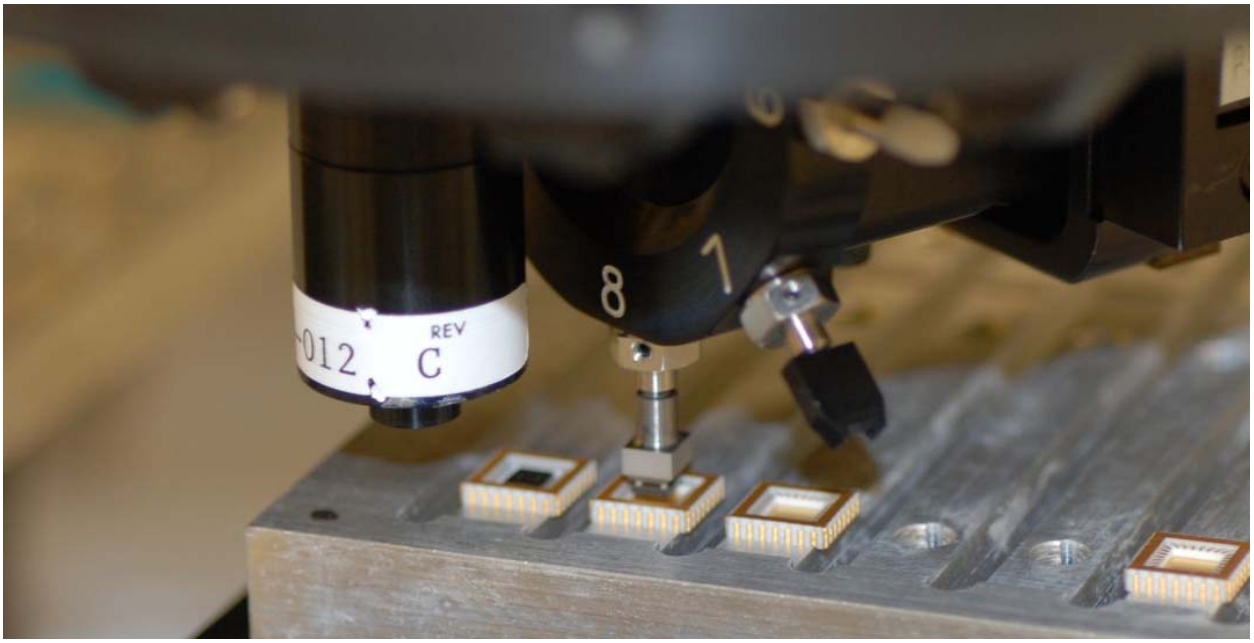

Figure 8-13. Photo showing Palomar tool placing die into package with vacuum pick-up tool.

After die placement in the Palomar, the packages are placed in the SST-1200 for epoxy cure. The SST is a tool made for vacuum bake-outs and solder-reflow, and is also commonly used for lid seals. In this case it is used as a high-temperature computer-controlled vacuum oven for curing the epoxy used in the die attach process. A photograph of the tool is shown in Figure

8-14. The dice are placed on a heated graphite fixture inside the tool chamber, with a thermocouple attached to the graphite plate for use by the temperature feedback controller. Three different die attach materials have been used in FY07: JM 7000, Diemat, and a gold-tin metal solder. All three are cured in the SST, but each requires a different cure schedule, described below. In each case, before running the tool with actual parts, a dry-run is performed as a cleaning process for the chamber and to verify proper operation.

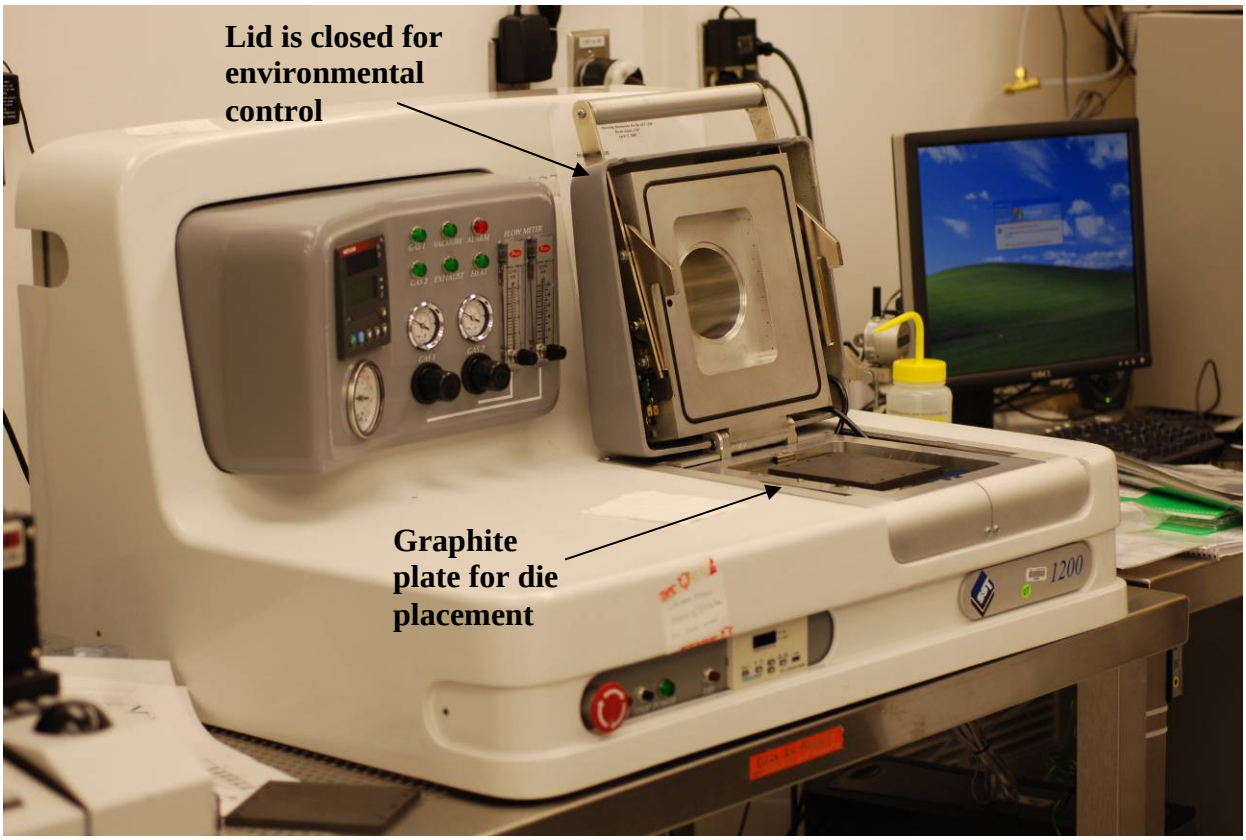

Figure 8-14. Photo of the SST-1200 vacuum bake-out and solder-reflow tool.

8.3.1.2 JM 7000 Cure Process

When JM 7000 is used, the epoxy is automatically dispensed using the Palomar. The silver-filled conductive version of JM 7000 has been used for all parts this FY, although conductivity of the die attach is not a requirement. It is cured in the SST oven using the following schedule:

1. Vacuum purge of chamber for 2 minutes
2. 5-minute ramp to 300 C with flowing nitrogen in chamber
3. 2-minute vacuum purge at 300 C
4. 10 minutes flowing nitrogen at 300 C
5. 23 hours and 48 minutes vacuum bake-out at 300 C
6. 12-minute cool-down with flowing nitrogen

The initial cure is performed in nitrogen to properly cure the epoxy and prevent bubble formation, and the extended vacuum bake-out is done to ensure a fully cured epoxy for a clean packaged environment.

8.3.1.3 Diemat Cure Process

The Diemat epoxy is also dispensed automatically using the Palomar. It is cured in the SST oven using the following schedule:

1. Vacuum purge of chamber for 2 minutes
2. The Diemat is pre-baked for 45 minutes at 100 C, and then cured for 15 minutes at 225 C.
3. Cooled

This is the manufacturer's recommended cure schedule.

8.3.1.4 Gold-tin Solder Die Attach

For the solder die-attach, a solder pre-form is manually placed inside the package. Using a pair of tweezers, the die is then manually placed on top of the pre-form. For this die-attach process, a metal film stack must be initially deposited on the back side of the die for proper adhesion. A stack of 200 Å Ti, 1000 Å Pt, and then 5000 Å Au was deposited in an evaporation chamber using standard metal deposition parameters. The dice are held in place by setting them on a wire mesh so that metal can be deposited on the bottom of the die without damaging the released structures on the top surface. This leaves a non-continuous waffle-pattern deposition, but has proven sufficient for this series of tests. The solder reflow is performed in the SST using the following schedule:

1. Pump the chamber down to vacuum and then back-fill with Nitrogen 3 times.
2. Ramp up to 150 C in 2:30 minutes in vacuum
3. Hold for 1 minute
4. Ramp to 215 C
5. Hold for 10 minutes
6. Purge with nitrogen to cool to room temperature

8.3.1.5 Wire Bonding

Once the dice are attached in the packages, the electrical connection needs to be made between the dice and the package. This is done using a Delvotek 6400 automated wire-bonding tool, shown in Figure 8-15.

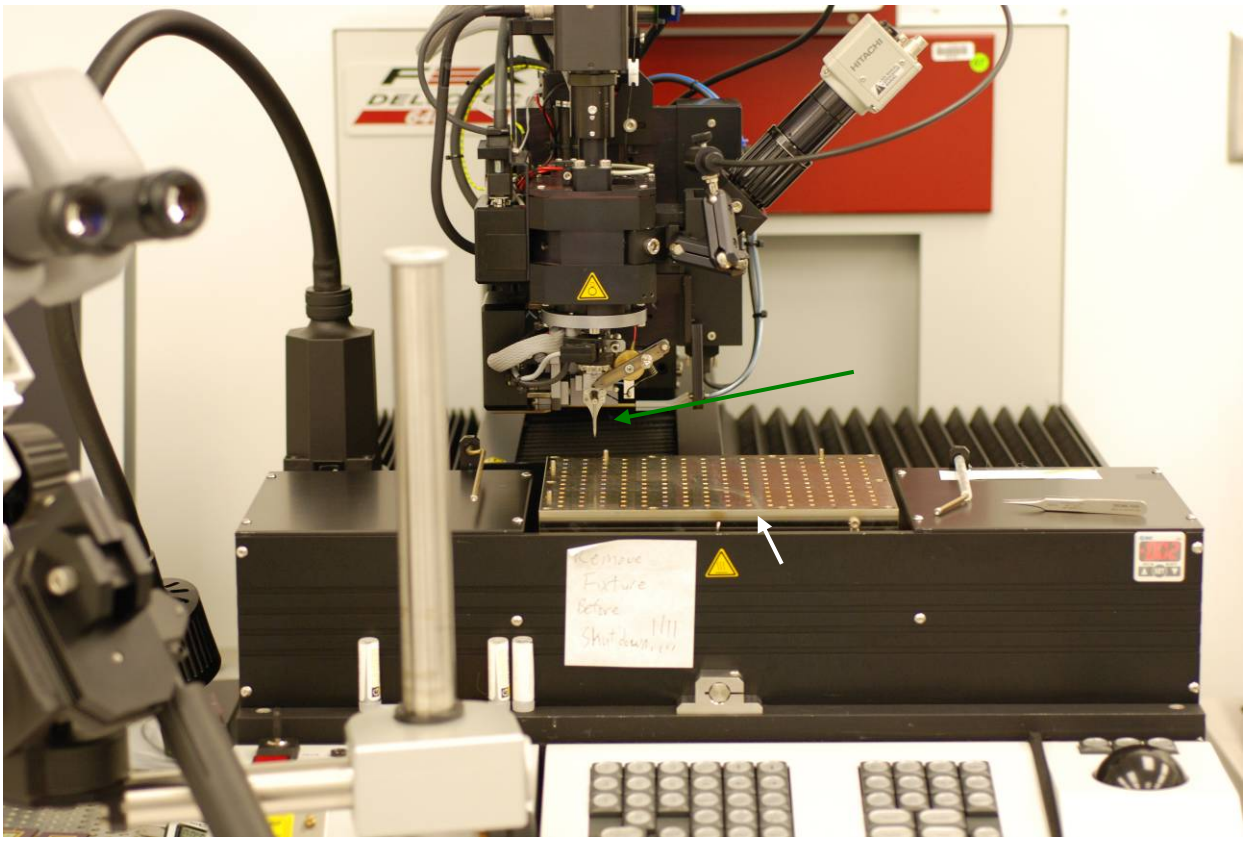

Figure 8-15. Delvotek 6400 Wire Bonding Tool.

The tool is computer-controlled and uses a vision system to ensure proper wire-bond placement. A 1-mil thick aluminum wire is used to create wedge bonds first on the die bond-pads and then on the package pads. A combination of force and ultrasonic power is used to create the bond between the wire and the platinum coated bond pads. While they are tool specific, the bond parameters used are listed in Table 8-2 for reference.

Table 8-2. Wire Bond Parameters

	Time	Ultrasonic Power	Force
Bond to Die	**20 ms**	**35 units**	**15 grams**
Bond to Package	**30 ms**	**30 units**	**30 grams**

A zoomed-in photo of the wire-bond needle approaching the die in a package is shown in Figure 8-16.

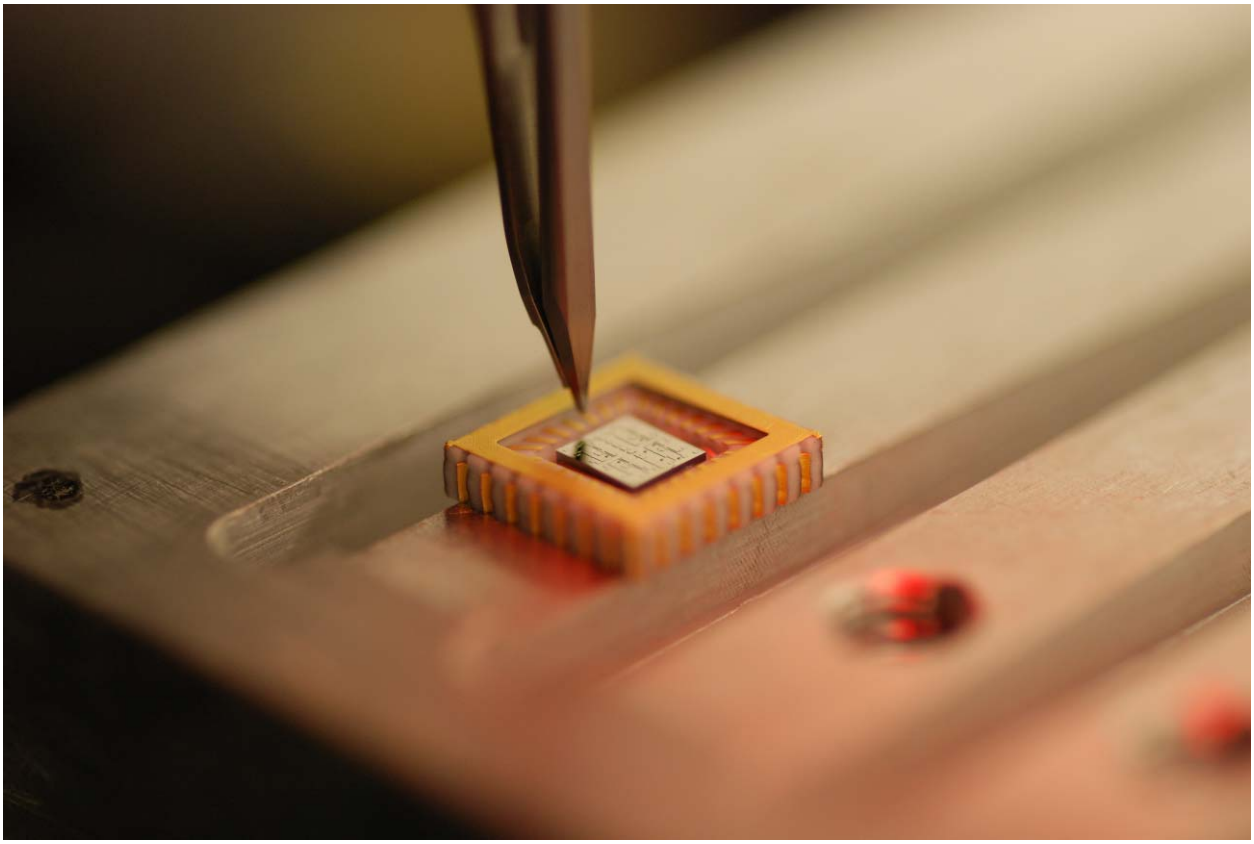

Figure 8-16. Wire-bond needle approaching the die on the Delvotek 6400 wire-bond tool.

8.3.1.6 Lid Seal

The final step in the hermetic packaging process is to seal the lid on the package. This step is done in the SST-1200 tool (Figure 8-14). Before implementing this step, lids are argon plasma cleaned for 5 minutes at 400 W to ensure that pre-formed solder rings on the lids are clean and free of oxidation. Then packages are oxygen plasma cleaned for 10 minutes, also at 400 W, to clean off any residual hydrocarbon contamination on device contact surfaces for improved electrical contact performance.

For the lid-seal process, a method is required to secure and position lids relative to the package. A custom graphite fixture has been designed for this purpose, with 15 wells machined into the top of a graphite plate, allowing 15 LCC packages to be sealed at a time. Each well has two different sized pockets, the deeper pocket sized for the lid and the second slightly larger and sized for the dimensions of the package. The lid is placed upside down in the lower pocket (Figure 8-17), and the package is then placed upside down on top of the lid (Figure 8-18). Proper machining of the fixture plate ensures that the lid is properly centered and aligned on the package.

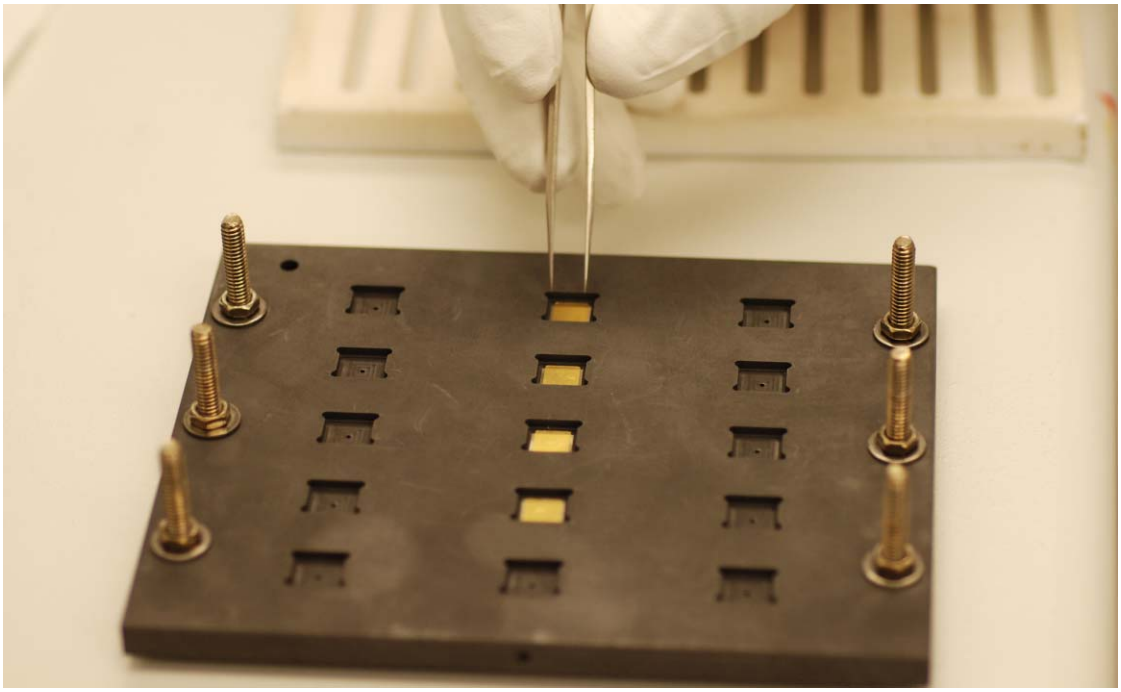

Figure 8-17. Custom graphite fixture showing lid placement in the lower machined pocket.

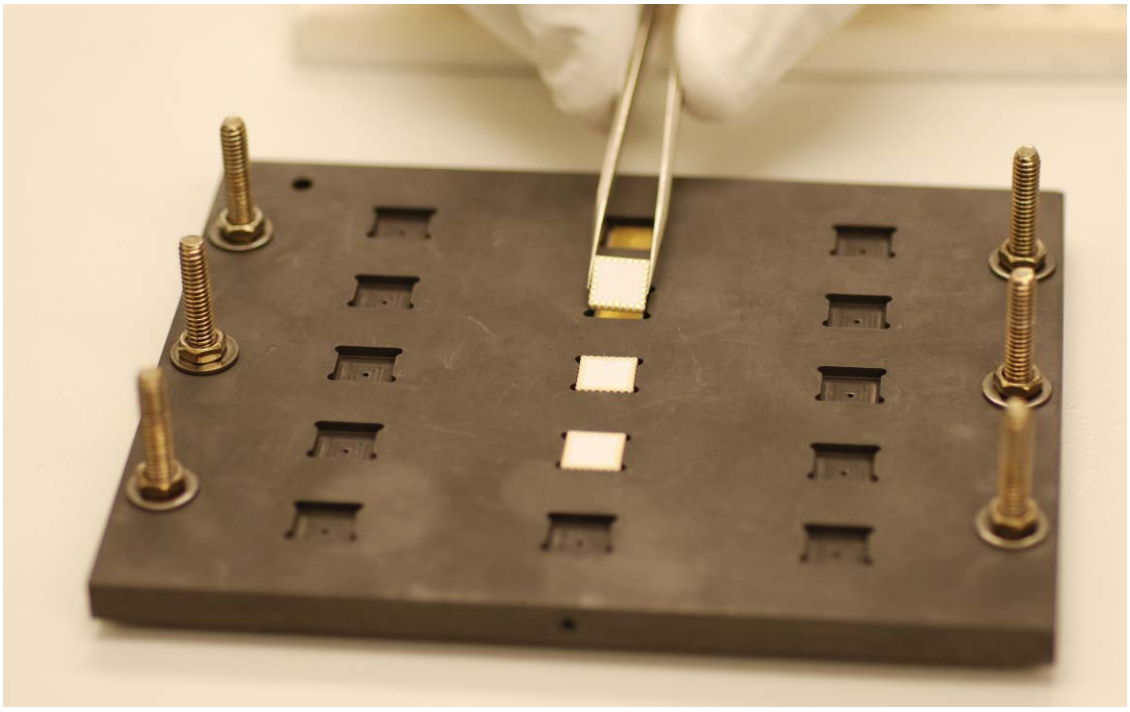

Figure 8-18. Packages being placed upside down on top of the lids.

The final preparation step for the lid seal operation is to attach a top plate to the fixture that contains 15 individual springs that press the packages down onto the lids with a controllable amount of force (Figure 8-19). Each spring is threaded into a hole directly above each of the

packages, with the force exerted by the spring onto the package controlled by threading the springs further into or out of the top plate.

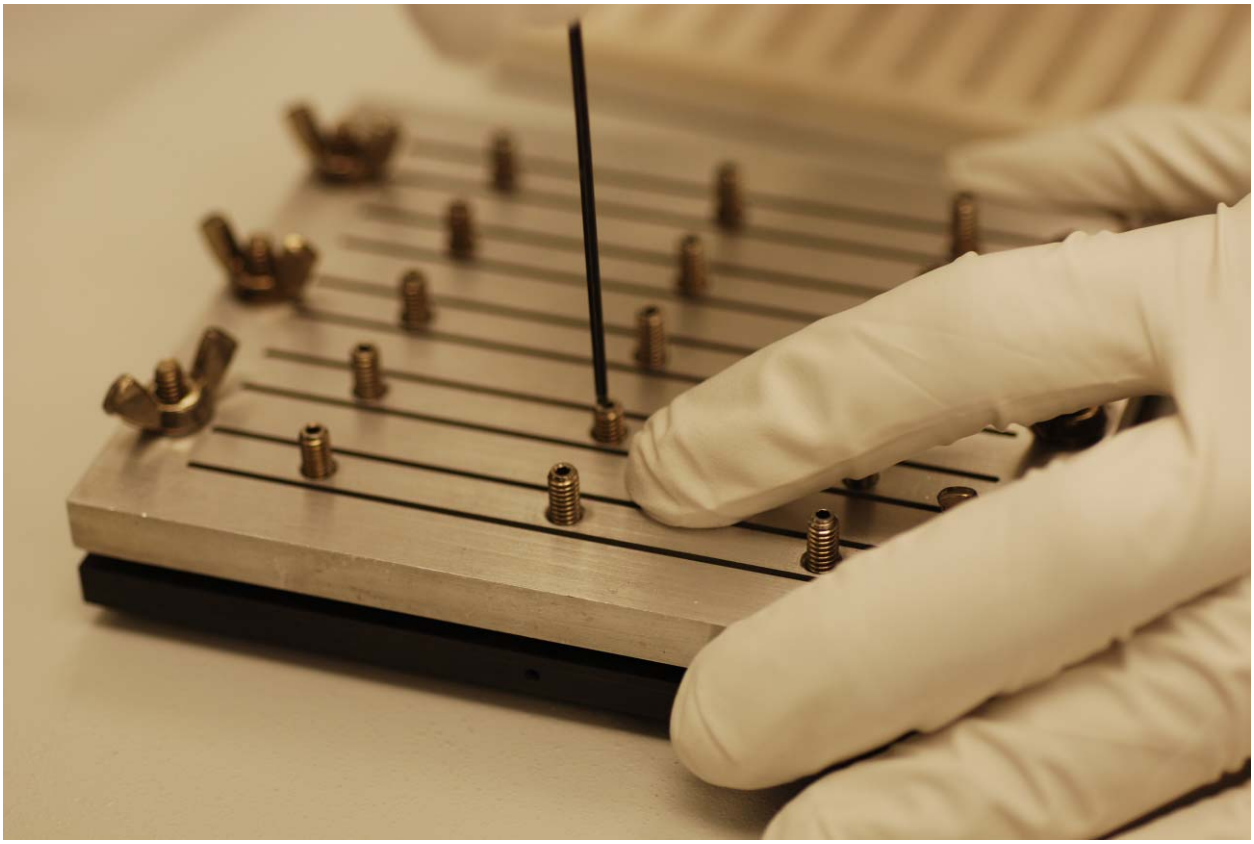

Figure 8-19. Fixture plate containing individual pogo-springs for applying force to package during lid-seal operation.

Once fully assembled, the graphite lid-seal fixture is placed into the SST chamber with an attached thermocouple. The thermal and vacuum cycling for proper lid seal is outlined below.

1. Pump the chamber down to vacuum and then back-fill with nitrogen three times.
2. Ramp the temperature up to 200 C in 1 minute.
3. While holding at 200 C, vacuum pump and nitrogen back-fill the chamber a fourth time.
4. Ramp the temperature up to 310 C over 1:30 minutes.
5. Hold at 310 C in a closed Nitrogen environment for 1 minute. This allows the lid solder to reflow and seal a clean environment in the package.
6. Cool down the chamber by flowing Nitrogen.

A design of experiments was conducted to determine the ideal time, temperature, and force for the LCC used in this work. Visual inspection of the lid-seal quality was used to determine ideal parameters. Gross and fine leak tests have not been performed on this package.

8.3.2 Leadless Chip Carrier Assembly onto Printed Circuit Board

8.3.2.1 Solder Paste Application

The first step in attaching the hermetic LCC package onto the printed circuit board is to apply a small dot of solder paste onto each of the metal pads on the LCC mounting location of the PCB. This is done using the automatic dispensing capability of the Palomar 3500-II. Figure 8-20 shows this tool being used to dispense the solder paste onto the PCB.

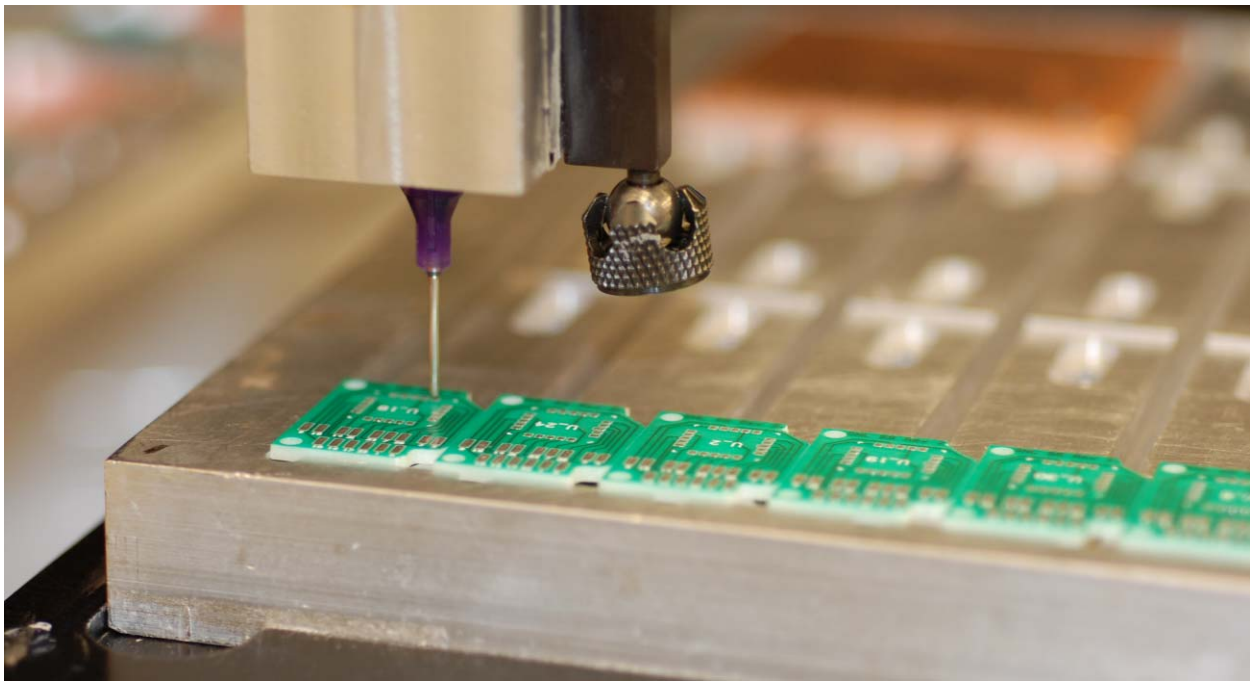

Figure 8-20. Palomar 3500-II used to dispense solder paste onto the package contact pads on the PCB.

8.3.2.2 Package Placement and Solder Reflow

The package is then placed onto the PCB using a Finetech flip-chip bonder tool, shown in Figure 8-21. This tool has a set of cameras oriented in such a way as to show both the top surface of the PCB and the bottom surface of the package at the same time. These images are overlaid on the computer screen to allow for precision manual alignment of the two parts, as shown in Figure 8-22. Once aligned, the tool places the package and the stage is heated to 260 C to re-flow the solder paste and complete the electrical connection of the package to the PCB, as shown in Figure 8-23.

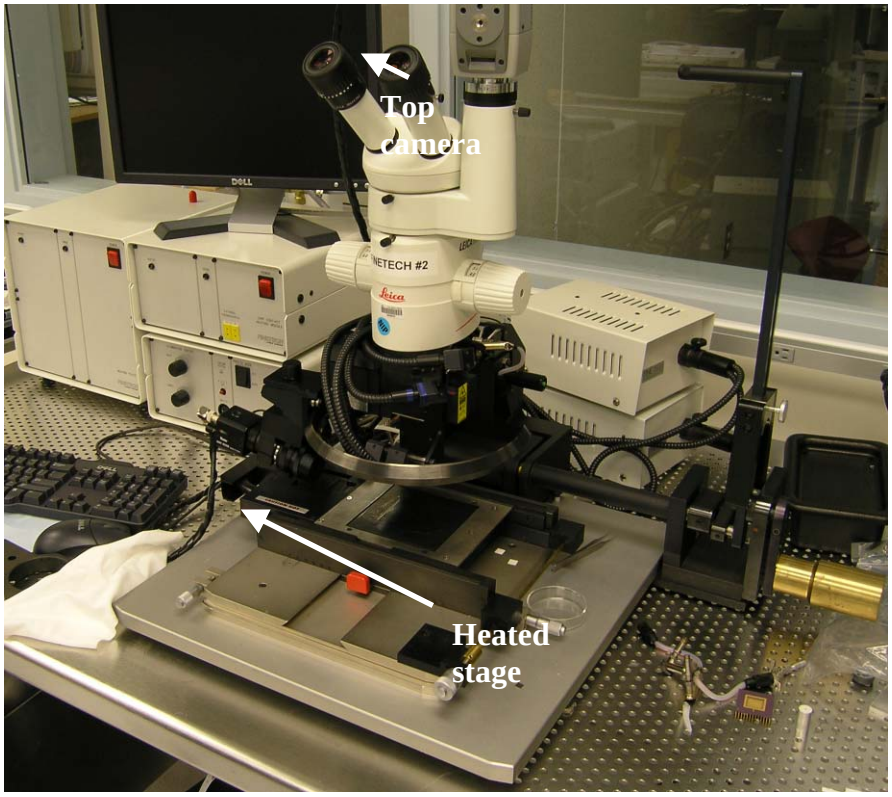

Figure 8-21. Finetech flip-chip bonder tool used to attach LCC onto PCB.

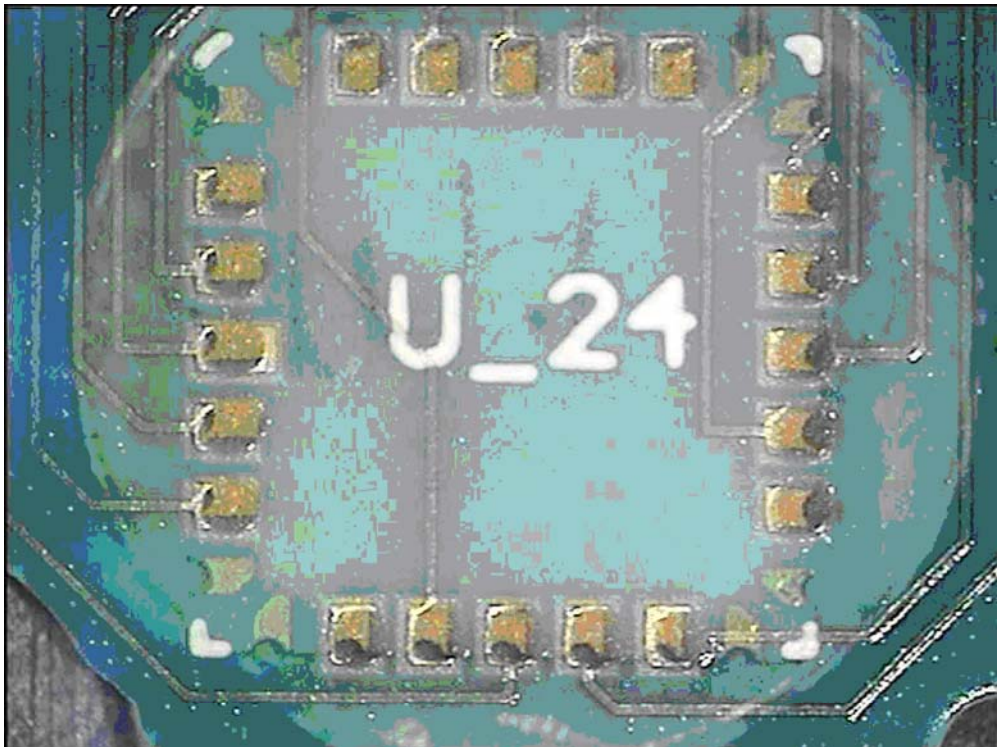

Figure 8-22. Image capture from the Finetech showing the alignment of the package and PCB before attaching.

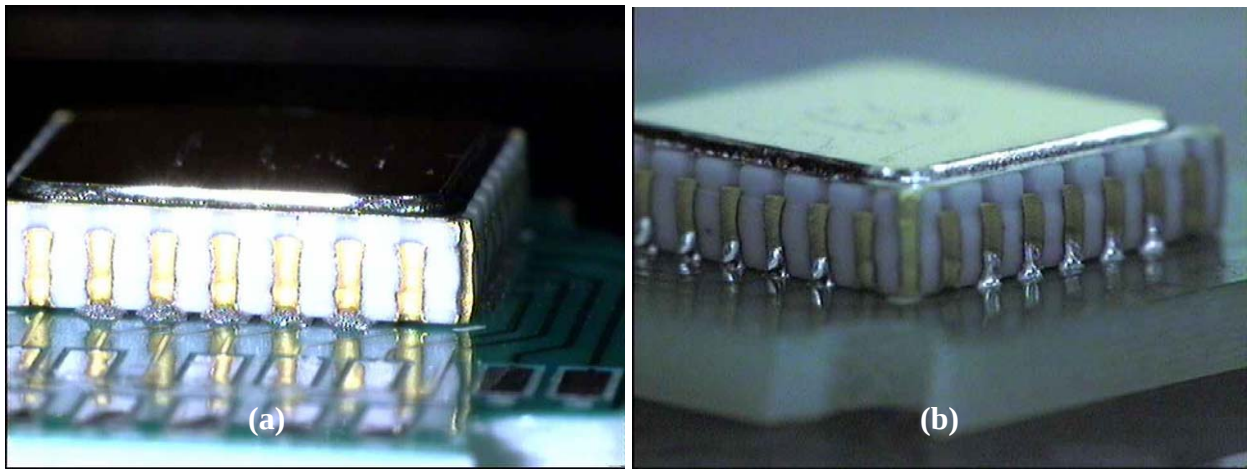

Figure 8-23. Images from Finetech showing the package placed on the PCB (a) before and (b) after solder re-flow.

8.3.2.3 Package Under-fill

The solder attachment of the LCC onto the PCB is for electrical connection only; it may not be an adequate mechanical connection, especially in the presence of large shock loads. For this reason, the package is under-filled with an epoxy to provide a secure mechanical connection of the LCC. LocTite Hysol FP4549-V20 fast-flow underfill epoxy is used for this task and is again dispensed using the automated Palomar 3500-II tool. To improve the wicking of the epoxy, the PCBs are heated on a hot-plate to 100 C before application. The epoxy is then dispensed along one edge of the package, as shown in Figure 8-24, and the low-viscosity allows it to wick completely underneath the package and form a uniform bond across the bottom and around all four edges of the package. It is then cured in an oven at 165 C for 30 minutes to set the under-fill epoxy.

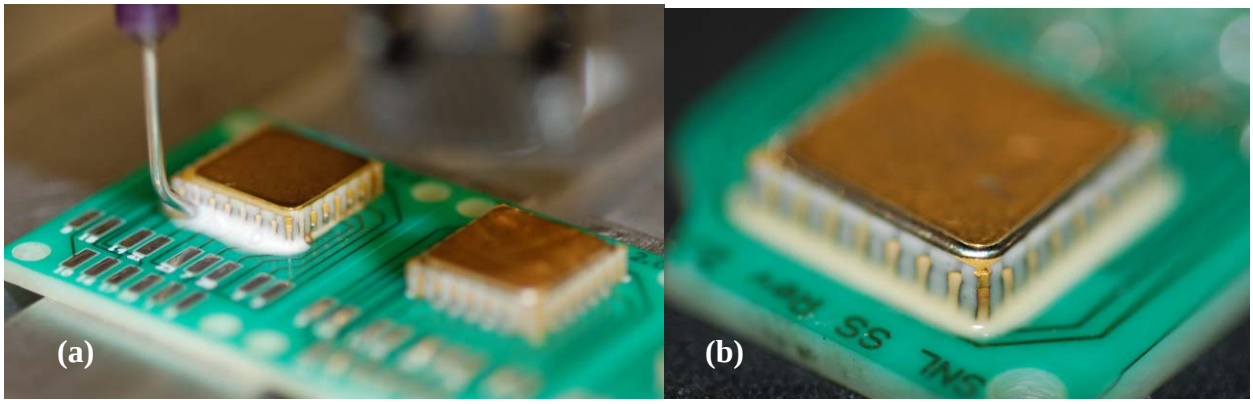

Figure 8-24. (a) Under-fill epoxy dispense using the Palomar 3500-II, and (b) final cured epoxy.

8.3.3 Housing Assembly

With the LCC now mechanically and electrically attached to the PCB, all that remains is to mount the electrical connector and attach everything to the metal housing.

8.3.3.1 Electrical Connector Attachment

In preparation for mounting the electrical connector, all the connector solder pads on the PCB are pre-tinned with solder using a manual soldering iron. The connector wires are trimmed and stripped and then soldered onto the PCB using a soldering iron, as shown in Figure 8-25.

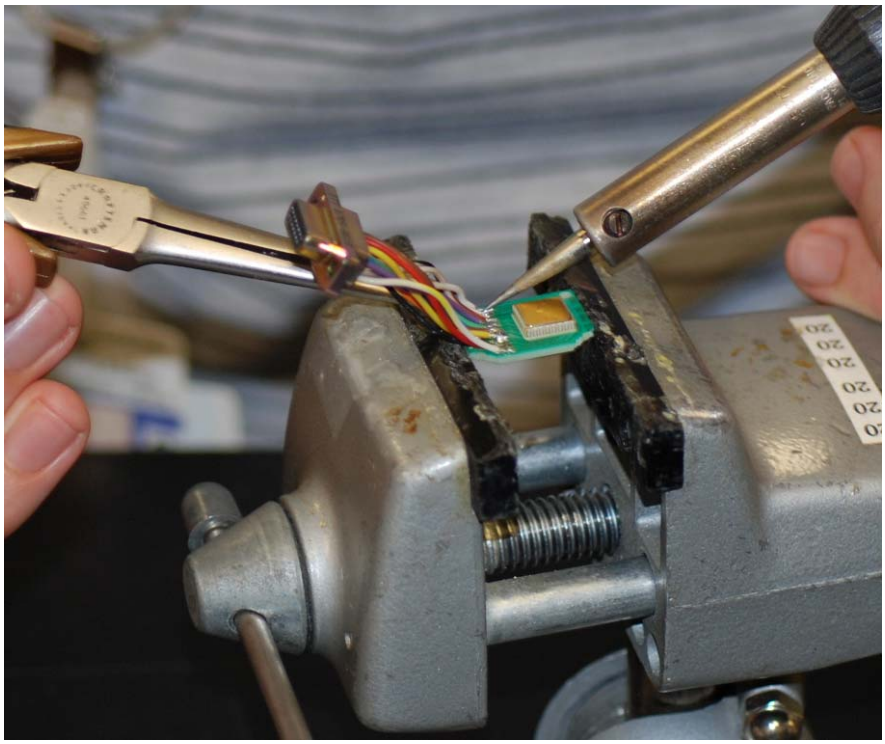

Figure 8-25. Soldering connector onto PCB.

The wiring diagram is listed in Table 8-3.

Table 8-3. Wiring Diagram

Device	Open	Close	Contact	Common
1	Black	Red	Brown	Orange
2	Blue	Yellow	Green	Orange
3	White	Violet	Grey	Blk/White
4	Brown/White	Orange/White	Red/White	Blk/White
Substrate	Yellow/White			

To provide some strain relief for the wires at the solder connection with the board, a fast setting 5-minute epoxy is applied to all the solder points. This also helps ensure that the wires do not flex and short during an applied acceleration.

8.3.3.2 PCB attached to housing

The final assembly step is to secure the PCB and connector in the metal housing. A two-part high-peel-strength epoxy is used to secure the board to the housing, and the board is also bolted down to the housing at each of its four corners. The final assembled part is placed in an oven at

66 C for 2 hours to cure and set the high-peel-strength epoxy (manufacturer's recommendations). The final assembly is shown in Figure 8-26.

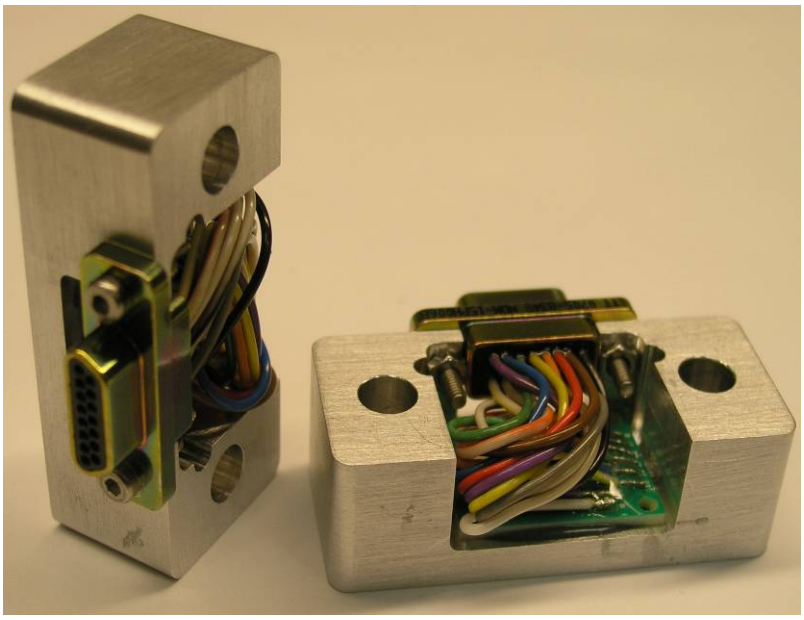

Figure 8-26. Final Rev 2 package assembly.

8.4 FY07 Packaging Challenges

Two major challenges identified with the above described packaging process. The first resulted in a large-scale investigation of the die-attach material used and the second lowered yield in the final product. Each will be described in the following sections.

8.4.1 JM 7000 Contamination

The initial packaging plan called for the exclusive use of JM 7000 as the die-attach material. JM 7000 was developed to be a low out-gassing epoxy and has been used extensively at Sandia. In our initial packaging experiments, a delayed failure mechanism was observed in which packages tested the day lid seal was completed were found to functioning normally. However, if tested the next day they were found to fail the self-test (open/close of contacts using thermal actuators). On occasion a device would open normally under self-test, and then some time after power was removed from the actuator it would self-close. This delayed self-close was observed with delays of seconds to tens of seconds after removal of power to the actuator.

Initial failure analysis involved removing the package lids to optically examine devices in search for an understanding of the failure. A strong odor was detected immediately upon removal of the lid, and a viscous fluid-like contamination was observed on the MEMS die that interfered with proper operation of the thermal actuators and sense mass. The viscous damping observed from this contamination explains the delayed self-close observed in testing.

Through further package examination, a correlation was found between the odor detected upon lid removal and the failure of a device. This suggests some kind of contamination present in the

package after lid-seal that interferes with the operation of the MEMS device. The contamination is clearly volatile, as indicated by its strong smell and because it evaporates within 24 hours of lid removal. A gas-chromatograph/mass-spectrometer (GCMS) analysis was performed on the package atmosphere to determine chemical composition and assist in determining the source of the contamination. Results from the initial experiment are shown in Figure 8-27.

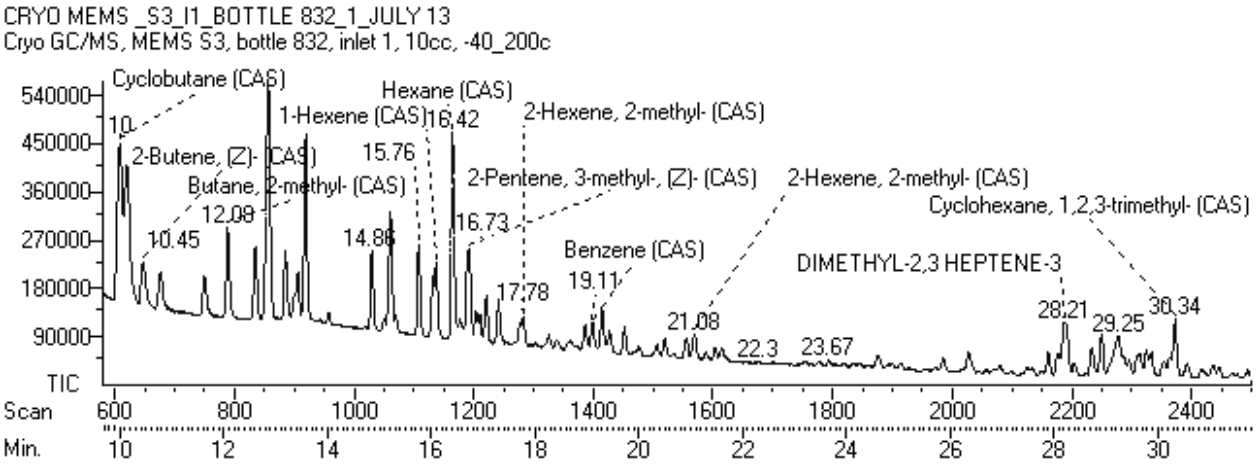

Figure 8-27. GCMS analysis results of package environment.

The results indicate the presence of several volatile organic compounds in the package environment. This "signature" of contamination was used for further testing to determine the source of the contamination. The initial experiment included a package containing only cured JM 7000 with no die in a lid-sealed package, an empty lid-sealed package to rule out tool contamination, and a package with only a platinum coated die and no die attach in a sealed package. The latter case was used to rule out metallization and release. It was determined from this series that the contamination was clearly coming from the JM 7000. All packages without the JM 7000 were completely clean with nothing detected beyond the Nitrogen inside the sealed package.

It was suspected that the JM 7000 cure schedule was insufficient to fully cure and ensure low out-gassing after lid seal. At the time of this problem, the standard cure schedule for JM 7000 was 300 C for only 30 minutes. An experiment was conducted in which samples were cured for either 30 minutes at 300 C, or for 24 hours at 300 C. The 24-hour cured samples were free from contamination while the 30 minute samples were contaminated as expected. This experiment seems to verify that the cure schedule for JM 7000 is critical for achieving a clean package after lid-seal, and that the standard practice used to that point was insufficient.

JM 7000 is purchased in batches as needed and has a shelf life of less than a year. It was considered a possibility that the current batch of material was somehow contaminated in a way not typical of the product. A new batch was ordered from the manufacturer and it was tested in the GCMS to address this possibility. This new batch also showed the same characteristic signature of contamination.

Based on these results it was determined that a 30 minute 300 C cure is insufficient. This led to the use of the 24 hour cure schedule described in section 8.3.1.1. It is expected that something less than 24 hours would be equally as effective, but there was no time for further experimentation to determine an optimal cure time, so 24 hours was used for all packages in FY07.

8.4.2 Cracked Bond Pads

The metallization step, as described in section 2.2.3.1 of the FY06 Shock Switch report [1], has the potential to short bond pads and electrical traces if they are not properly shadowed. (Note that a metallization process checklist is included in Appendix A.) The switch and actuators are shadowed by covering them in the uppermost poly-silicon layer (P4). However, it is desirable to have metal on all bond pads and traces to reduce their series resistance and therefore they are not protected by a P4 shadow mask layer. Instead, to prevent shorting from metallization, the traces and bond pads are self-shadowed by the inclusion of an overhang around the entire structure. This overhang prevents the metal from under-cutting enough to short the trace or bond pad to the substrate metal. A 2D cross section of a bond pad edge is shown in Figure 8-28 for clarification of this technique.

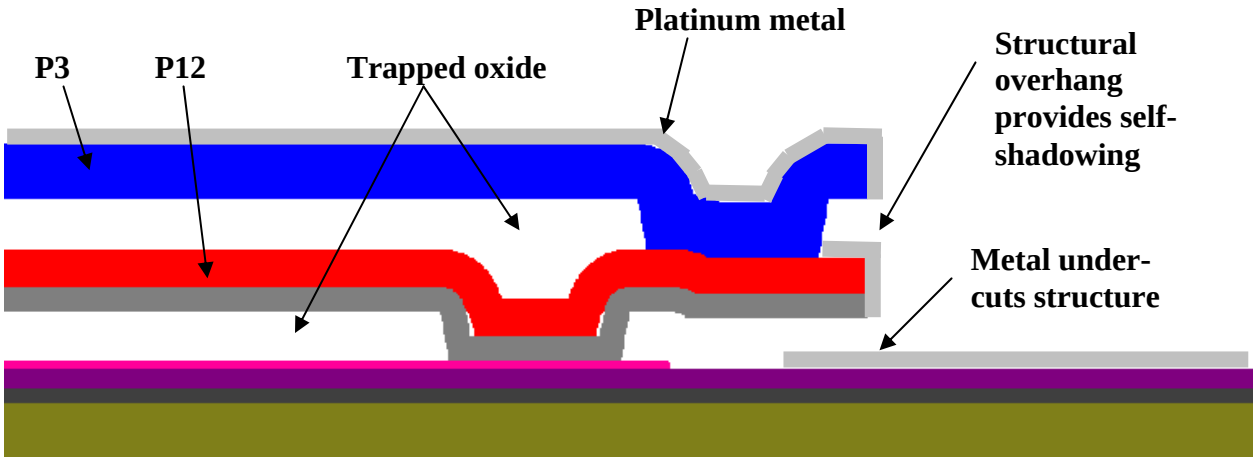

Figure 8-28, Cross-sectional view of bond pad edge showing overhang.

A problem occurred during the wire bonding step of packaging. Bond pads were cracking along the edges during the wire bonding step and thereby causing the bond pad to electrically short to the metal on the substrate. If two or more bond pads are cracked on a device, they short to each other across the substrate metal rendering the device inoperable. The cracked bond pad edge occurs when the wire bond tool is not properly centered in the bond pad. Figure 8-29 shows an example wire bond with the cracked area indicated.

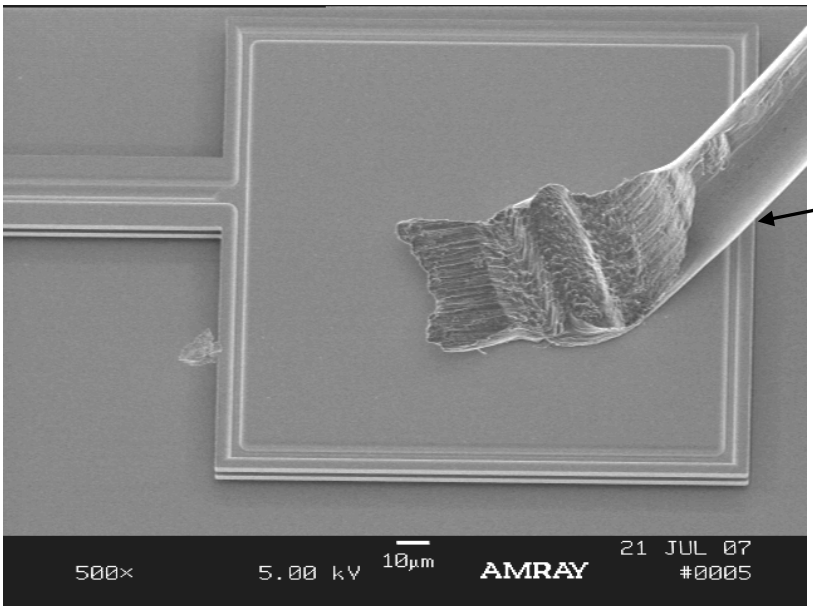

Figure 8-29. SEM image of a wire bond not properly centered on the bond pad.

Bond pad cracking is also more likely to happen when using a larger needle; the use of a smaller needle has greatly reduced the frequency of shorts.

8.5 Future Considerations

It is clear that packaging of the shock switch is a critical step for successful testing and delivery. The Revision 2 packaging solution outlined in this chapter is a testing solution, and is not intended to represent a final deliverable package for a customer. However, it does provide a necessary platform for interfacing with the device in a consistent manner. It is expected that each application will require a modification to this general approach to meet specific customer needs. This year's packaging activities have given us a strong foundation of understanding that can then be applied as specific customer needs are understood.

Specific future work in packaging must include a better characterization of the die-attach material used, and an understanding of how to properly cure or apply the die attach to ensure a clean and reliable package.

In addition, continued revisions of the metal housing and connector approach are required to reduce cost and schedule impacts when packaging the large quantities of devices that will be required for functional and environmental testing. As customer needs are better understood, this will become a more critical effort in order to ensure that the shock sensor can properly interface both electrically and mechanically in the intended applications.

Finally, an understanding of shock attenuation and its relationship to specific packaging designs is required for accurate sensing of a shock input. In particular, the die adhesive and adhesive used to attach the PCB onto the housing may attenuate shock before it reaches the die level sensor. This must be better understood.

9. EXPERIMENTAL MODEL VALIDATION

The chapter presents measured test data from fabricated parts for purposes of comparing it with results from computational models of those parts. Several tests were identified that looked at both thermal and mechanical properties of the devices. These tests were applied to Revision 1 parts in the first three quarters of the year and minimally to Revision 2 parts in the last quarter. Testing of Revision 2 parts focused on developing tests and capabilities that would advance the TRL of the shock switch; this testing is covered in Section 10.

9.1 Stable Equilibrium under Thermal Loading

Thermal cycling of the shock switches was conducted to determine whether Revision 1 designs would remain bi-stable and if thermal actuators would continue to function after exposure to both hot and cold temperature environments. Modeling predicted the devices would stay bi-stable. Data was also collected during this investigation to quantify the drift in the second stable point resulting from the thermal exposure.

9.1.1 Objectives and Approach

A Thermotron SE-300-2 environmental chamber was utilized for this investigation. The product temperature control (PTC) and temperature set-point deviation capabilities of the oven controller were used to make certain that die were soaked at the specified test temperature. The PTC thermocouple was securely attached to the 3"× 4"× 2" aluminum block that the die were placed on during the test cycle. The thermal cycle profile consisted of a ramp from room temperature (25ºC) to the test temperature, followed by a 30 minute soak to ensure all devices achieved thermal equilibrium before ramping back to room temperature. Each die was checked after each thermal cycle and the state or condition of each device recorded before proceeding to the next temperature cycle test. This test sequence was repeated for several temperatures; results and temperatures are presented below.

The test was broken into several smaller investigations in order the fully understand the source and mechanisms that impact the operation of the packaged device. Packaging processes such as die attach and lid seal include several high-temperature thermal cycles that can impact the device and cause the packaged product to function differently from the die itself. Metal layer deposition also impacts the residual stress due to the CTE mismatch between the metal and poly-Si. Thus, initial thermal testing began with unpackaged die to isolate the intrinsic device characteristics from any additional stress resulting from the packaging process and/or CTE mismatches between the package, evaporated metal, and Poly-Si materials. Both bare and metalized die were investigated to better understand and possibly quantify the effects of the metal-Poly-Si CT mismatch on the device operation after thermal exposure.

Initialization of all devices on each die was necessary to prepare the as-fabricated switches for testing. Each switch's contact mechanism had to be set in order to latch the contact points into their final position using the Set/Reset thermal actuator. Each switch was then cycled a couple times to verify functionality and that the switch was indeed bi-stable with a Self-Test/Reset sequence. For clarification, a Self-Test is where power is applied to the thermal actuator that

manually pushes the switch toward the contacts until is snaps closed. Reset is the opposite process that uses the Set/Reset thermal actuator to reset the device into the normal sense position with the contact open and proof mass in the second stable position. Switches with thermal actuators that were non-functional or had limited linear displacement were manually cycled through the sequence using probe tips to confirm bi-stable condition.

Each bi-stable switch was visually inspected after each thermal exposure to determine whether the switch had closed during the cycle or remained in the initial position. Following the visual inspection was an electrical functionality test on the thermal actuators to make certain they were still functional. Stability and reliability of these switches are of utmost importance since the switch would be subjected to various thermal environments throughout its useful lifetime and must remain stable and continue to function reliably. Data collection on bare die also included recording the second stable position of the un-protected process monitor switches that had verniers to determine whether the position was influenced by the thermal cycle. These test structures were not recorded on the metalized die because they were un-protected and completely covered with metal after metal deposition.

9.1.2 Results

Three bare die and three metalized die were used for testing. Switches could not be subjected to temperatures below freezing with the current configuration of the oven, which does not have de-humidification capability to prevent frosting and freezing. Several attempts were made to flow clean dry air (CDA) into the chamber for several hours to reduce the percent of relative humidity in chamber. Purging did lower the percent of relative humidity but the chamber still frosted during the ramp back to room temp.

All devices in this investigation remained bi-stable after each thermal cycle. Some devices were observed to close at lower temperatures, but remained in the open position at a higher temperature. This was theorized to be the result of rough handling during the transfer of the die from the Gel-Pak onto the aluminum block in the oven. Careful handling for the higher temperature cycle indicated that handling was indeed the reason for the previous switch closures.

None of the thermal actuators failed during testing except in one case where a probe tip accident destroyed one. Both the Set and Reset actuators continued to function following each test.

Tracking of drift in the second stable location could be accomplished only on devices that were not metalized. The test sequence described above was repeated for four temperatures: 85°F, 135°F, 185°F, and 235°F. At all four temperatures bi-stability was checked and both thermal actuators were checked for functionality. In all cases, devices remained bi-stable and functional. Locations of the second stable positions were only measured for the final two temperatures and they are shown in Table 9-1. There were only a few instances in which the second stable location changed.

Table 9-1. Position of the Second Stable Location After Thermal Cycling (± 0.0625 μm)

	Bare Die 1		Bare Die 2		Bare Die 3	
Temp (°F)	**185**	**235**	**185**	**235**	**185**	**235**
2F_103g	9.75	9.75	9.75	9.75	9.5	9.625
10F_519g	12.25	12.25	12.25	12.25	12.125	12.125
2F_50g	9.75	9.75	9.75	9.75	9.75	9.75
10F_2433g	12.25	12.25	12.25	12.25	12.25	12.25
5F_240g	10.75	10.75	10.75	10.75	10.75	10.75
20F_1033g	8.5	8.5	8.5	8.5	8.5	8.5
10F_105g	12.25	12.25	12.25	12.25	12.25	12.125
20F_4839g	8.5	8.5	8.5	8.5	8.5	8.5
10F_5925g	12.25	12.25	12.25	12.25	12.25	12.25
20F_11784g	8.375	8.375	8.375	8.375	8.25	8.375
5F_490g	10.75	10.75	10.75	10.75	10.75	10.75
20F_2450g	8.5	8.5	Broken	-----	8.5	8.5
5F_2741g	10.25	10.25	10.25	10.25	10.25	10.25
5F_968g	10.75	10.75	10.5	10.625	10.5	10.5

9.2 Modal Testing

9.2.1 Objectives and Approach

Modal information is typical used for model validation of linear systems. Since the shock switches have inherent geometric nonlinearities, the approach needs to be slightly modified. For model validation of the shock switches, modal data that is collected with very small motions around each of the stable equilibrium points will be used. This is similar to standard practice in that modal information is used, but it differs from the standard practice in that data will be available about two stable equilibrium conditions rather than the more typical single stable condition.

Experimental modal validation of dynamic models consists of two tests for each revision that collectively measure the in-plane and out-of-plane resonant frequencies of the various devices. A high-speed camera and feature-tracking method is used for in-plane measurements, and a commercial laser Doppler vibrometer (LDV) system is used for the out-of-plane measurements. All the measurements are taken with very small amplitude motions to estimate linear resonances at each of the two stable locations. For the in-plane test measurements the ring-down to the stable locations is used, and for the out-of-plane measurements base excitation is used. These tests were conducted for both Revision 1 and Revision 2 in FY07.

9.2.2 Testing and Results

9.2.2.1 Revision 1 In-Plane Modal Tests

The goal of this testing is to measure the approximate linear resonances in the actuation direction at both stable locations of the four designs used in Revision 1 of the passive shock switch. All

results described here are based on data derived from high-speed camera measurements of dynamic events. The devices tested are all un-metalized and do not have thermal actuators for set/reset capability. This was done solely because the devices with thermal actuators have a lid that makes it hard to watch the action of the mass from above. Also, as an offshoot of some other testing on the same devices, these devices were all super-glued to a block of aluminum. It is likely this changed the resonant frequencies somewhat due to changes in residual stress from the glue drying.

The camera image was calibrated using a calibration slide provided with another instrument that has an accuracy of 0.2 μm for the distance between the lines (with respect to the middle of the lines). The accuracy of the line diameter is 0.5 μm. Figure 9-1 shows the image taken of the calibration slide.

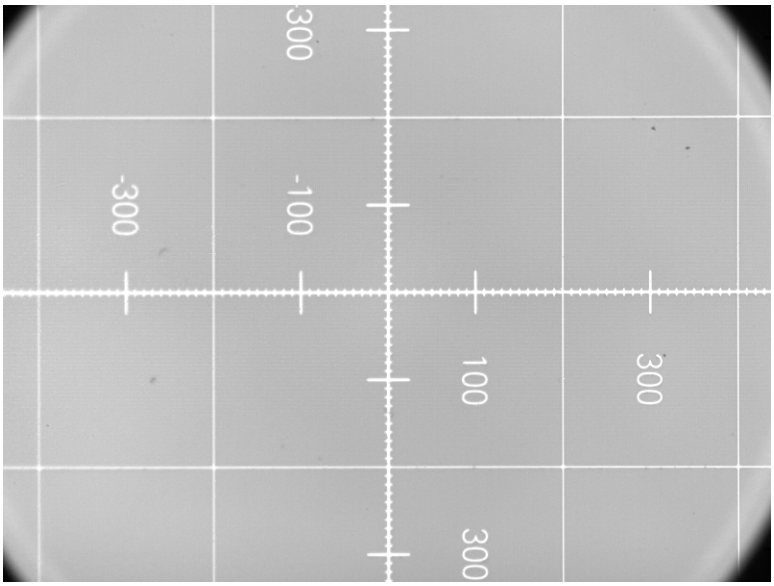

Figure 9-1. Calibration image taken with high-speed camera using all the optics used for the rest of the testing.

Prior to any test, the stable locations of the mass were measured using the vernier designed into the devices. A probe was then used to push the sense mass to the unstable equilibrium position, and the high speed camera captured the motion as the sense mass pulled away from the probe tip and snapped into one of the stable equilibrium positions. The camera was sampled at 117647 Hz with a shutter speed of 2 μs. For cases where aliasing was suspected in the results, the camera was sampled again at the higher rate of 153846 Hz and the same shutter speed. The comparison of peaks on the frequency spectrums of both sets of data allowed the unwrapping of the data. Figure 9-2 shows images taken from the movie recorded at the beginning and end of the two events.

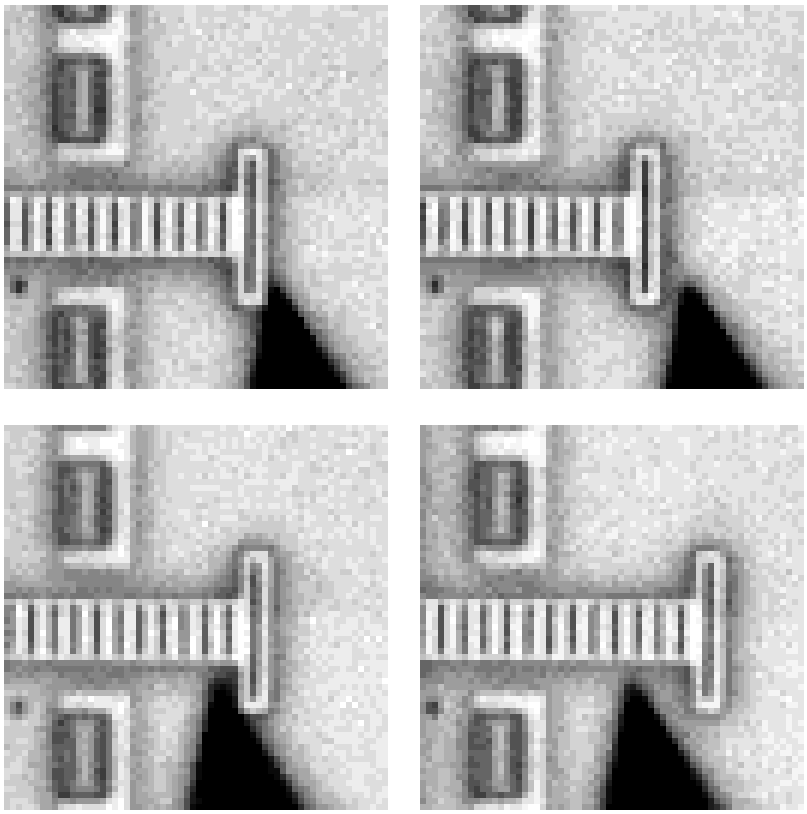

Figure 9-2. Pictures showing before and after snap-through for the open equilibrium position (top) and for the closed equilibrium position (bottom).

Triggering was provided by user input after the event. After the movie record was trimmed to just the snap-through event, it was analyzed using a Labview program utilizing National Instrument's feature tracking algorithms. This produced plots like the example shown in Figure 9-3.

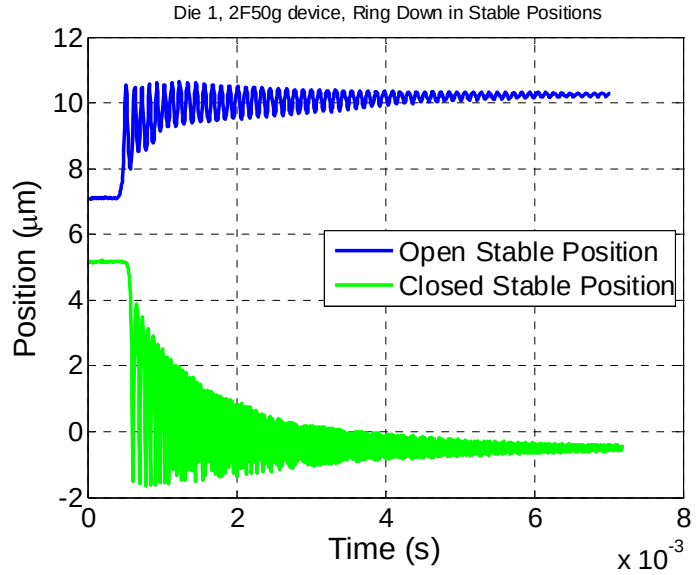

Figure 9-3. Positions extracted from feature tracking on high-speed camera images from ring-down to stable position events. Example from Die 1, 2F50g device.

It is interesting to note that the position where the sense mass pulled away from the probe is not the same for the two traces. This is likely due to adhesion of the mass to the probe tip. This effect would tend to produce a dead band around low force region of the unstable equilibrium location.

Once this data was collected an FFT was used on the late time ring-down oscillations to find the approximate linear resonant frequency. The amount of data to include in the FFT was arbitrarily decided based on a trade-off between the absence of harmonics in the results and the frequency resolution. This resulted in Figure 9-4. The peaks in the figure correspond with resonance at the equilibrium positions.

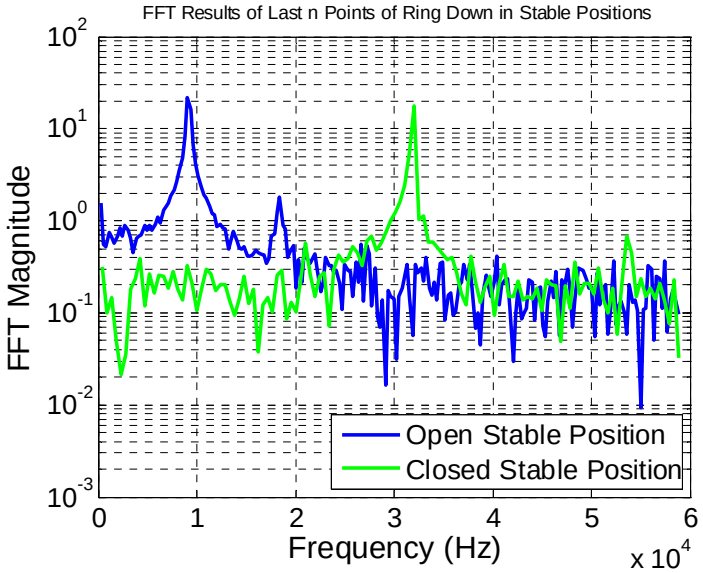

Figure 9-4. FFT of data in Figure 9-3.

Notice that even when a minimum number of late time points is used, there are still harmonics evident in the FFT results. These indicate that the response, even at small amplitudes towards the end of the time plots, is not completely linear. However, we tried to use only enough data so that the effect of this nonlinearity on the frequency results was less than the FFT frequency resolution.

Table 9-2 to Table 9-5 show the equilibrium position and frequency results for all die tested. The errors associated with these measurements are based on the scale readability directly. The smallest increment on the vernier is 0.25 μm. The frequency error is Δf/2 and varies with the number of points in the FFT; the number reported is the worst case in each position.

Table 9-2. 2F50g Device Results

Die	Open Position (± 0.125 □m*)	Closed Position (± 0.125 □m*)	Open Frequency (±181 Hz **)	Closed Frequency (± 239 Hz **)
1	10.25	-0.50	9071	32041
2	9.75	-0.25	7867	29962
3	10.75	-0.75	10465	34312

*This error is half of the smallest increment on the scale.
**This error is half of the Δf in the FFT. The largest value for the column is reported.

Table 9-3. 5F240g Device Results

Die	Open Position (± 0.125 □m*)	Closed Position (± 0.125 □m*)	Open Frequency (±181 Hz **)	Closed Frequency (± 239 Hz **)
1	11.25	-0.25	17734	65687
2	10.50	0.00	13926	60882
3	10.75	-0.25	15897	63672

Table 9-4. 10F519g Device Results

Die	Open Position (± 0.125 □m*)	Closed Position (± 0.125 □m*)	Open Frequency (±181 Hz **)	Closed Frequency (± 239 Hz **)
1	12.75	-0.25	18931	69273
2	12.00	0.00	15201	65397
3	12.75	-0.50	18809	68848

Table 9-5. 20F1033g Device Results

Die	Open Position (± 0.125 □m*)	Closed Position (± 0.125 □m*)	Open Frequency (±181 Hz **)	Closed Frequency (± 239 Hz **)
1	9.00	-0.50	27363	70878
2	8.25	0.00	19677	63830
3	8.75	-0.50	25640	69738

9.2.2.2 Revision 1 Out-of-Plane Modal Tests

The goal of this testing was to measure the approximate linear resonances normal to the plane of the devices at both stable locations of the four designs used in Revision 1. All the results described here are based on data measured with a Polytec MSA400 Micro System Analyzer and a base excitation. This system is a scanning LDV system with two lasers: one used for the measurement reference and the other for the device response. The devices were excited vertically with a piezo actuator, and the response of the device at various locations is measured with the LDV. The results are used to locate the resonant peaks and generate operational mode shapes. The devices tested were all un-metalized and did not have thermal actuators for set/reset capability.

The average response of the switch mass in the out-of-plane direction for the 20F-1033 device is shown in Figure 9-5. This is a typical result from the tests although the results for the closed position typically have peak frequencies that are significantly higher. Note that peaks correspond with resonant frequencies of the system. Operational mode shapes were generated for each of the tests and shapes that consistently appeared in all of the devices were identified. These shapes are shown in Figure 9-6. They are essentially the same for all of the switch designs.

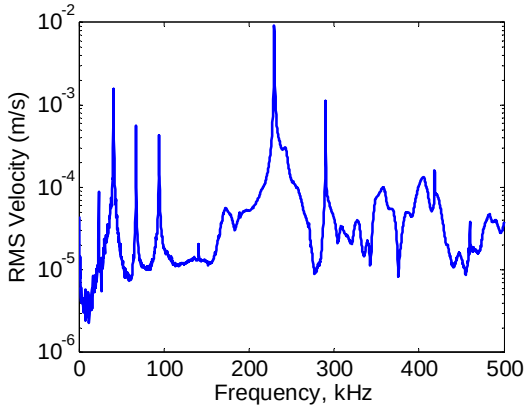

Figure 9-5. Revision 1—average response of the switch for the 20F1033 design.

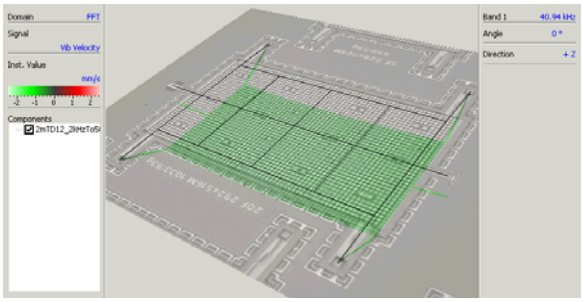

Z Translation

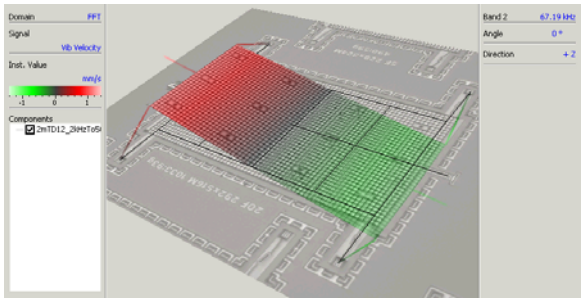

X Rotation

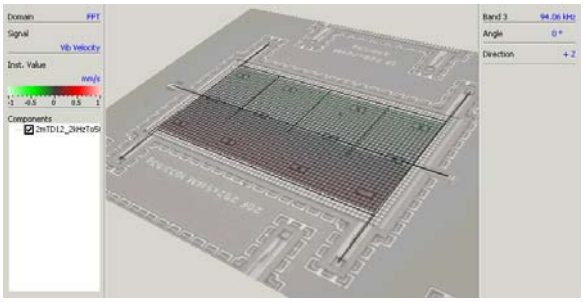

Y Rotation

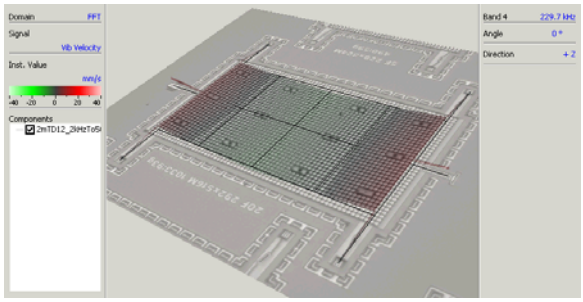

Plate Bending

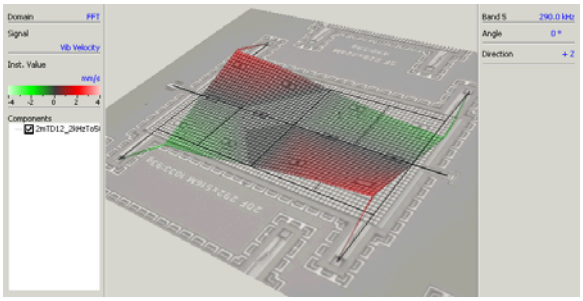

Plate Torsion

Figure 9-6. Revision 1—mode shapes identified from out-of-plane modal tests.

For each switch design, resonant mode shapes were identified and associated frequencies where they occur were recorded. These results are shown in Table 9-6.

Table 9-6. Revision 1: Out-of-Plane Resonant Frequencies Identified

	Z Translation		X Rotation		Y Rotation	
Part	**Open Frequencies (kHz ± 160 Hz)**	**Closed Frequencies (kHz ± 160 Hz)**	**Open Frequencies (kHz ± 160 Hz)**	**Closed Frequencies (kHz ± 160 Hz)**	**Open Frequencies (kHz ± 160 Hz)**	**Closed Frequencies (kHz ± 160 Hz)**
2F50	20.25	25.25	33.75	43.00	42.25	53.75
5F240	37.81	49.38	NA	83.13	84.69	112.50
10F519	32.81	42.19	53.44	69.69	78.44	100.30
20F1033	40.94	47.50	67.19	79.38	94.06	110.30

	Plate Bending		Plate Torsion	
Part	**Open Frequencies (kHz ± 160 Hz)**	**Closed Frequencies (kHz ± 160 Hz)**	**Open Frequencies (kHz ± 160 Hz)**	**Closed Frequencies (kHz ± 160 Hz)**
2F50	148.30	149.80	140.00	NA
5F240	227.50	233.40	NA	NA
10F519	226.60	230.30	278.80	294.40
20F1033	229.70	233.40	290.00	303.10

9.3 Residual Stress

The tests conducted for residual stress were aimed at identifying packaging step processes where the largest increases in residual stress occurred. Residual stress was initially identified as a concern by the modeling team. There were many variations in switch threshold performance at the end of FY06 [1] for Revision 1 devices. This was perplexing since Revision 1 designs were specifically optimized to reduce variation of the threshold force required to switch devices from the open state to the closed state. This optimization accounted for the documented process variability in the fabrication of the silicon die. However, after further study, the team realized and discovered that Revision 1 devices were in fact very sensitive to residual stress changes on the die. The hypothesis created was that processing of the dice into packaged parts changed the residual stress on the dice enough to affect changes in the switch threshold that were observed in FY06. Several tests were designed to verify this hypothesis and, together with more modeling, allow future designs to account for the residual stress. In parallel to this, a modified design was in progress for Revision 2 that theoretically would reduce the switch sensitivity to residual stress – see .Section 3.2 for details.

9.3.1 Objectives and Approach

Revision 1 testing in FY06 revealed a variability that was not predicted by models [1]. There was also a bias from the model results to the mean result of the experimental results. Since the

hypothesis is that residual stress changes are producing both of these effects, either one could potentially be used as a metric to compare with measured residual stress throughout the testing. For the purposes of the experimental examination of residual stress, the variability of the data will be used as a metric.

Two methods were used to check and track residual stress on die at various stages of packaging. The first was to examine and note the two stable locations at the die level. Since the bi-stable mechanism is based on geometric bi-stability, any change in the stiffness or axial loading of the springs in the device affects the force deflection curve. This in turn changes the stable locations. Changes in residual stress of the substrate act to move the anchor locations for the switch relative to each other. This changes the axial loading on the springs and thus the force deflection curve. So, one way to measure the residual stress effects indirectly is to measure the stable locations under a microscope. If these positions change, it can be surmised that the switch threshold has changed as well. The drawback of this method is that the vernier devices on the switches have a limited sensitivity, and since the residual stress affects the stable locations only indirectly, the changes may to too small.

Another way to measure the residual stress is to include test structures on the die that are specifically designed to measure residual stress. For Revision 2 parts these devices were included. The residual stress measurement devices are designed with two bent beams, fixed at each end. There are indicators on these devices that show how much the bent beams move when the anchors are affected by residual stress changes in the substrate. See Section 4.2 for additional design details. Images of the devices were taken under a high magnification microscope at various stages in the processing. Image processing was used to analyze the changes in position of the residual stress test devices. Two styles of indicators were used in the design with the intention to compare their suitability for this type of analysis. Figure 9-7 shows example images of the two types of indicators. In these images, most of the devices are covered in a Poly 4 lid that keeps them from being damaged in the metallization process.

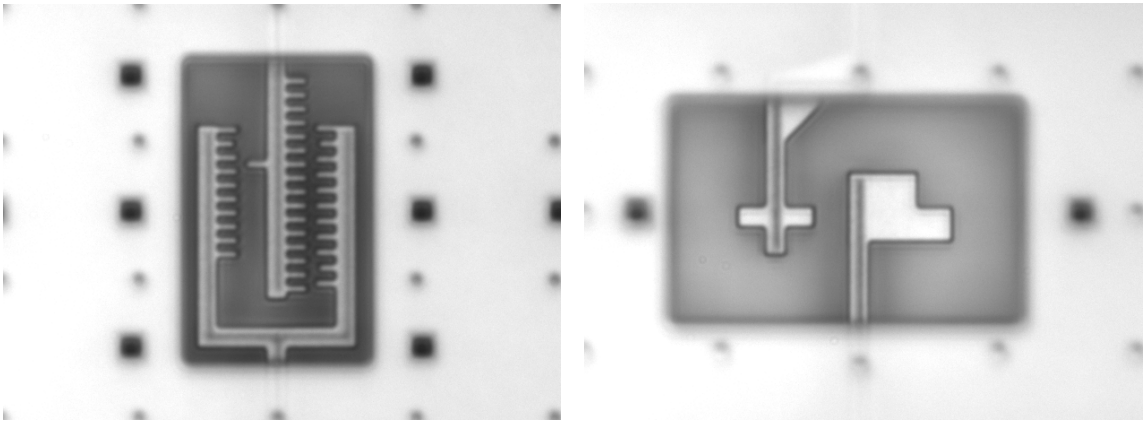

Vernier Style **Block Style**

Figure 9-7. Two styles of indicator used on Revision 1 residual stress measurement devices.

For the first iteration of these measurements a 50× objective was used. The resulting data did not have desirable uncertainty bounds so a 100× objective was used for all subsequent images. The camera image was calibrated using a calibration slide provided with another instrument that had an accuracy of 0.2 μm for the distance between the lines (with respect to the middle of the lines). The accuracy of the line diameter is 0.5 μm. Figure 9-8 shows the image taken of the calibration slide. This calibration resulted in scale factors of 0.1295±0.0005 μm/pixel for the 50× and 0.06475±0.00026 μm/pixel for the 100×.

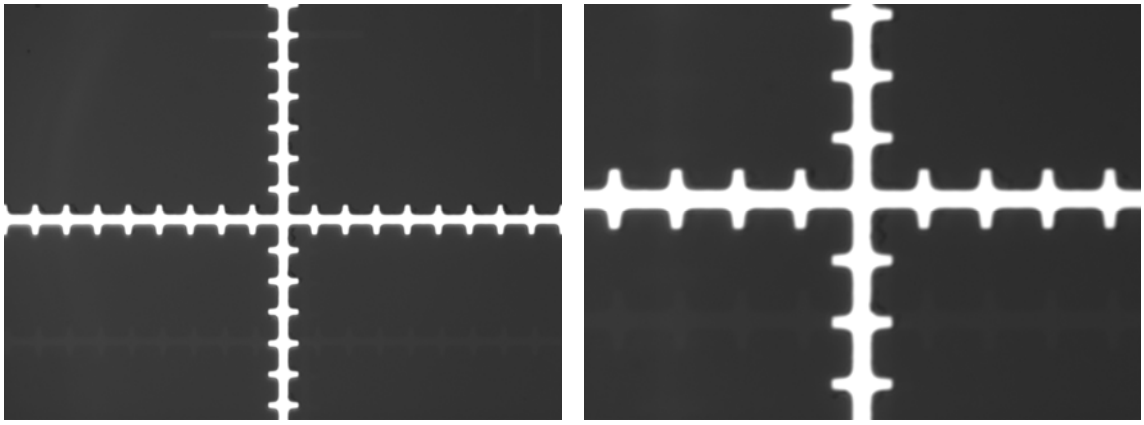

Figure 9-8. Calibration images taken with the camera using all the optics used for the rest of the testing and a 50× or 100× objective (respectively). Each tick mark is 10 μm.

Two styles of image processing were used to analyze images; the type of image process used depended on which style of indicator was imaged (vernier or block). The errors generated by the pattern matching algorithms used were quantified for each set of images using information on features with fixed distances that would not be affected by changes in the residual stress. This error accounted for feature distortions due to poor lighting, poor focus, rotation of subsequent images, etc. To reduce the image quality errors several steps were taken. First, the lighting was adjusted to give unsaturated images with intensity values that covered as broad a range as possible. Second, a focus indicator was used that allowed the operator to optimize the contrast across edges in a region of interest of the image while manually focusing the microscope. Finally, fixed features in the images were used to rotate the images so that the indicator action was vertical. This last step was critical as errors in rotation of the images seemed to give the most error in measurements.

The first type of image processing was used on the vernier style of indicator. The course reading of the vernier gives 2 μm spacing and was read for the gross motion. For instance, in the image example the gross motion of the vernier from zero (shorter tab) is about 2.5 μm. The first step in the image processing is to get two image intensity lines from the overall image, one through each of the two 2 μm spaced tab verniers. Figure 9-9 shows this for one of the images taken of a bare Revision 2 die just after it was released.

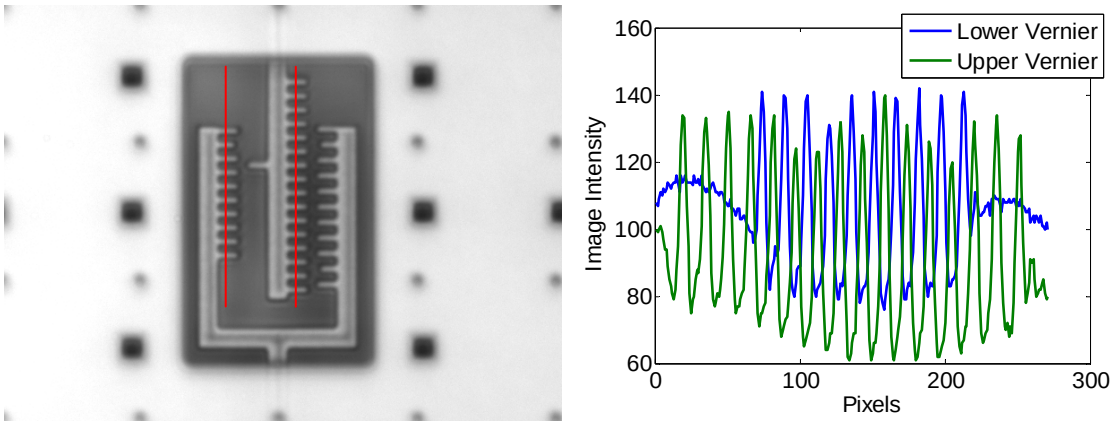

Figure 9-9. Image showing two image intensity lines used for processing and the image intensity plotted relative to first pixel in line.

The correlation between the two intensity lines is then calculated. Since both lines have peaks at 2 μm spacing, there should be a peak in the correlation every 2 μm. This result is shown in Figure 9-10. A negative value for delta pixels moves the vernier towards zero. The resulting correlation was then interpolated to improve the peak picking algorithm that determined the spacing between peaks and the distance from zero to the current location.

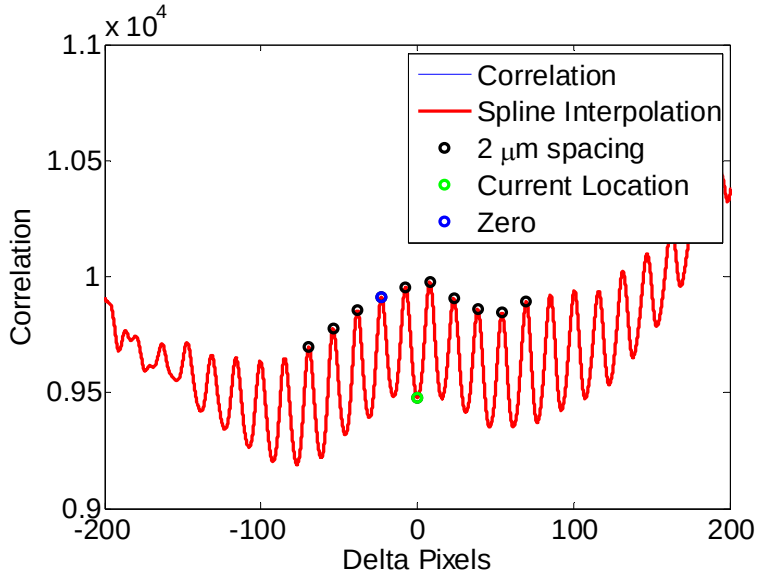

Figure 9-10. Correlation between the two intensity lines.

Ten iterations of the 2 μm spacing were collected and used to estimate the process error. The mean spacing was calculated along with the standard deviation. The bias of the mean from 2 μm was insignificant so did not contribute to the error estimates. The standard deviation of the measurements was used to calculate the 95% confidence interval. Since this error was calculated for every image, the error reported with the data changes slightly from image to image. However, the average 95% confidence error with the 50× objective was ±36 nm and with the 100× objective was ±16 nm.

The second type of image processing was used on the block style of indicator. This image processing relied on commercial feature tracking algorithms built into LabView. The devices with the block style indicators do not have an indication of the zero stress state as the vernier style do. To find the zero stress state, gages that did not respond to changes in residual stress were included close to the block style indicators to show the zero stress state. To find the stress level in the block style devices, we need to know the distance between the T and L sections in the actual device and also the distance between the same features for the gage. The difference between these values gives the displacement of the residual stress measurement device from zero. Figure 9-11 shows one such block style indicator with its gage that is located close to the device. Indicated on the images are the features selected for tracking with LabView for both the stress result and the uncertainty analysis. The vertical distance between these features in the indicator less the distance between these features in the gage gives the result for change in position from zero.

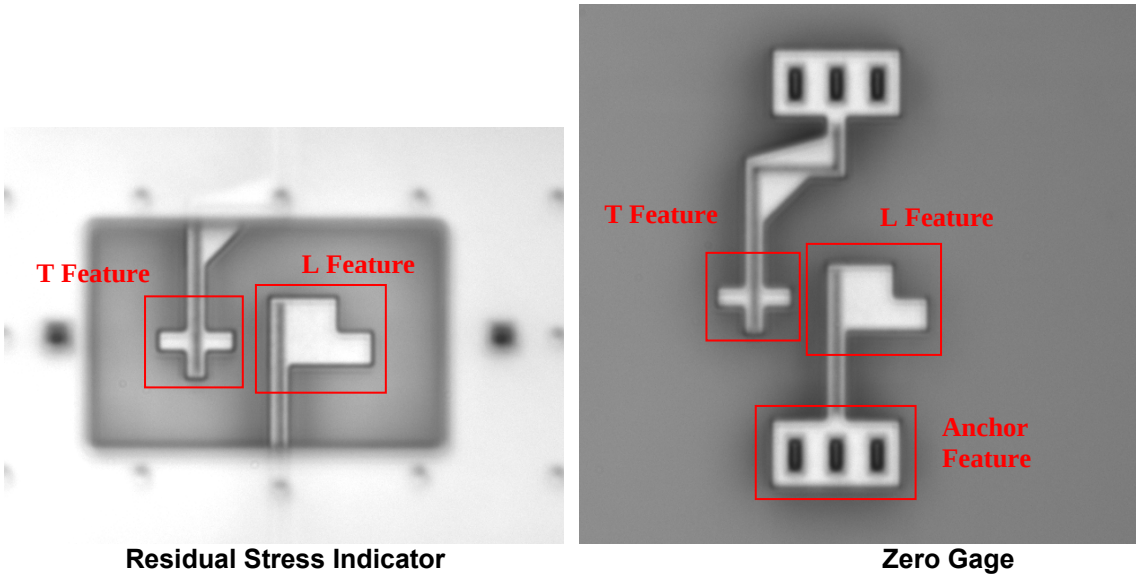

Figure 9-11. Block style residual stress indicator and its zero gage showing features selected for position tracking.

Quantification of uncertainty in the case of the block style indicators relies on the gage image. Since measurements were always made on more than one indicator and gage pair, two features with a fixed distance can be used for the series of gage images to quantify uncertainty in a similar manner to what was done on one image for the vernier style indicator. The distance from the gage L feature to the anchor for the L feature was measured in multiple gage images. As for the vernier style indicator, the variation in this measurement across the set of devices was used to find a 95% confidence interval. Since this calculation was across all devices, it will be a conservative estimate of the error in any one result and will not vary from image to image as it did with the vernier style indicator.

Once the displacements of the residual stress devices were measured, the residual stress could be calculated using the results in Section 4.2. These are the results provided below.

9.3.2 Testing and Results

Packaged device performance measurements from FY06 [1] showed a larger than expected variation. These were the initial results that prompted the investigation into residual stress which was theorized to be the reason for the variability in results. Centrifuge measurements showed a standard deviation up to 32% of the measured mean switch threshold. This was for the lowest threshold devices, and the standard deviation did decrease for the higher threshold devices. For drop-table functionality tests standard deviations between 15% and 40% of the measured mean switch threshold were found. Both of these results were for sample sizes between 4 and 10 parts.

For comparison, the stable locations on devices from 10 bare Revision 1 die were measured. The results indicated that the standard deviation in both stable locations measured was less then the measurement error. The measurement error was approximately 1% of the open stable location for most devices. Modeling efforts indicated that the likelihood that devices with such small variation in their stable locations would produce up to 40% standard deviation in their switch thresholds was very unlikely. This led to the theory that residual stress in the die is changing during packaging of the die.

The initial batch of devices for residual stress testing consisted of 8 low-threshold Revision 2 die and 8 high-threshold Revision 2 die. Although the switch thresholds were different on the low-g and high-g die, the residual stress devices were not. The use of the two kinds of Revision 2 die allowed a correlation between the residual stress measurements and any changes in the stable locations for a broader range of switch devices. The residual stress and stable locations were recorded for all parts at only the bare die stage and the metalized stage. The initial plan was to continue through all of the packaging steps but issues with the packaging process delayed the project to the point where time ran out.

Figure 9-12 shows the locations of the residual stress measurement devices and the gages. The device labeled 1 is the device with the vernier style readout and the rest are devices and gages for the block style readout. Locations 3 and 5 are the gages for devices 2 and 4 respectively. This image is a ribbon that cuts the Revision 2 die into top and bottom. The actual shock switches are not shown, but two are above the image shown and two are below. The reason more than one residual stress device was put on the die was to test the theory that the residual stress would change depending on location on the die.

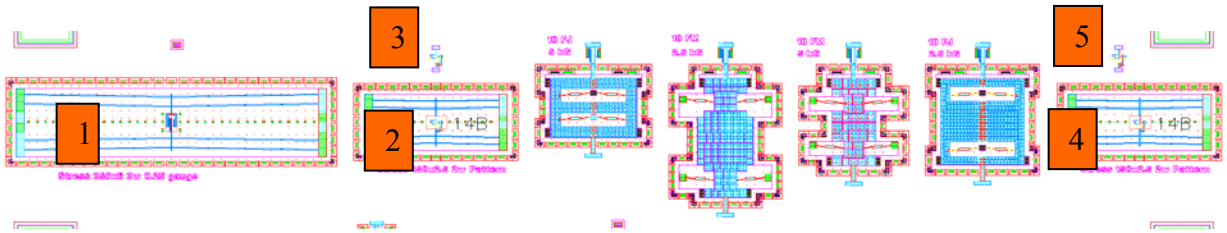

Figure 9-12. Devices located across Revision 2 die about half way up the die.

Table 9-7 shows results from the first lot of devices for which the residual stress was tracked. The negative values for average residual stress indicate compressive stress on the die. The 50×

objective was used for the results on bare die and the 100× was used for the post metallization results. There was also a significant effort to eliminate sources of error between the two stages which resulted in the improved error estimates. There are several interesting things to note from these results. First and as expected, all of the stresses measured were compressive. Also, results from device 2 were consistently higher than the results from device 4, which in turn were consistently higher than the results from device 1. This seems to indicate that the residual stress might vary across the die. Next, the change in residual stress from the metallization process is significantly smaller than the residual stress generated during the manufacturing of the die. Finally, the standard deviation in the residual stress from any of the devices tested is not enough to account for the types of variability seen from Revision 1 device performance tests. Unfortunately, delays in finalizing the packaging process precluded further testing before the authoring of this report. When the process is finalized this lot of test devices will continue to be tracked through packaging.

Table 9-7. Results from First Lot of Devices Tracked for Residual Stress

Process Stage	Device Location	Average Stress Device Displacement (□m)	95% Confidence Displacement Error (±□m)	Average Residual Stress (MPa)	Residual Stress Standard Deviation (MPa)
Bare Die	1	2.929	0.036	-15.34	0.60
	2	1.40	0.13	-19.68	0.54
	4	1.29	0.13	-17.91	0.40
Post Metallization	1	3.081	0.016	-16.23	0.56
	2	1.508	0.024	-21.24	0.84
	4	1.296	0.024	-19.28	0.97

A metal solder process was used to die attach a second lot of 6 dice; no lids were attached. Residual stress test structures were used to analyze residual stresses in the die in order to relate that to the metal die attach (Table 9-8). The metal die attach was viewed previously as not viable because of the suspicion that it would create large residual stress changes on the die. Note that comparison between the metalized residual stress results from the first batch of die and the post die attach results from this batch is somewhat suspect because they are different parts that were processed in separate runs of metallization. We do not have any data that indicates the variability of the metallization stress changes from run to run. Several comparisons can be made, however. First, in-plane locations of highest and lowest stress was the same for these dice after metal die attach as it was for the other lot of bare dice and metalized dice. The stresses shown for any process step and all of the stages do not really vary significantly from the stress of the bare die tested. The most interesting thing to note is that the variation of the residual stress after the metal die attach is much higher in some cases than the variation seen in the process steps for lot 1. This at least hints that there might be some validity to the theory that the process steps to package the die are main contributors to any variation in threshold seen during final testing of packaged parts.

Table 9-8. Results from First Lot of Devices Tested for Residual Stress

Process Stage	Device Location	Average Stress Device Displacement (□m)	95% Confidence Displacement Error (±□m)	Average Residual Stress (MPa)	Residual Stress Standard Deviation (MPa)
Post Metal Die Attach	1	2.345	0.017	-12.03	1.63
	2	0.965	0.034	-13.27	3.77
	4	1.121	0.034	-15.50	0.96

10. APPROACHING TRL 5 AND 6

The purpose of testing summarized here was to help mature the MEMS passive shock sensor; the ultimate goal is to mature the MEMS passive shock sensor to TRL 6. It was estimated that the shock switch was at TRL 4 at the end of FY06, and specific design revisions and test programs were designed to move the switch TRL 6. This involved both improvements in packaging and a redesign of the shock switch. Testing included a short test series evaluating the robustness of the proposed packaging and a long test series late in FY07 to evaluate the shock switch functionality [16] in relevant environments and survivability in normal environments. The packaging tests went very smoothly and we showed that the packages were robust to the environment envelope developed for Revision 2 of the shock switch. However, due to packaging issues and un-modeled consequences of design changes from FY06, test results showed that Revision 2 of the shock switches was not functional.

10.1 Package Survivability

Two prototype package concepts were subjected to 2× over-shocks and extreme thermal loading to determine their viability as package options for Revision 2 shock switches. The Revision 2 shock switches that were to be packaged late in FY07 had a maximum shock switch threshold of 25 kG so the packages were tested to levels of 50 kG. The worst thermal case from normal environments was a 24-cycle thermal shock between the two temperature extremes so the packages were also subjected to this environment. If they passed these two tests with no problems, then they were deemed to be a viable package option for Revision 2 of the shock switches.

10.1.1 Objectives and Approach

Two package concepts were provided for testing and they are shown in Figure 10-1 and Figure 10-2. Also see the packaging chapter of this report and specifically Section 8.2 for additional details on these particular concepts. These packages were to be shock tested at levels up to 2× the expected highest switch threshold and thermally cycled according to the worst-case normal environment. In addition, the epoxy connection in prototype package 1 was evaluated for its transmissibility in this application.

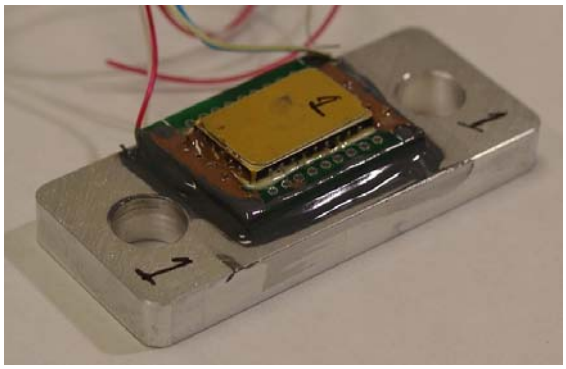

Figure 10-1. Prototype package 1.

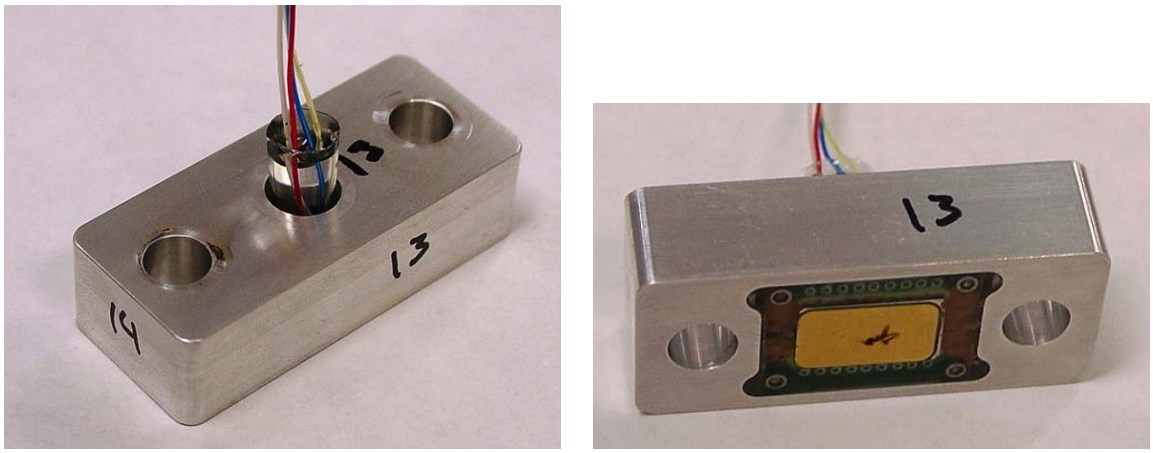

Figure 10-2. Prototype package 2.

The over-shock tests were performed on a Hopkinson bar with one device in each direction (X, Y, Z simultaneously).
Figure 10-3 shows the fixture for the Hopkinson bar loaded with prototype parts.
Figure 10-4 shows the Hopkinson bar apparatus with a vacuum chuck on the end to hold the fly-away fixture shown in
Figure 10-3. The parts were rotated so that each part got hit once in each direction. The shock level tested was increased incrementally up to the full level (50 kG) and visual inspections were performed to verify integrity. Each of the silicon wafers in the parts has been metalized and has a lead connected at each of four corners. This allows for a continuity check indicating potential cracks in the silicon or failures in the wire bonding or PCB connections. If there were no failures, each part was shocked three times at each of four levels up to the maximum. Two types of parts were tested (essentially two package designs) so the tests were repeated for the second type of part.

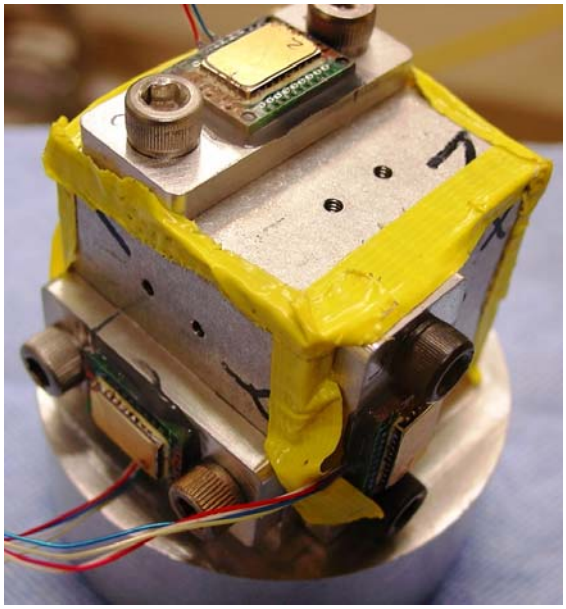

Figure 10-3. Hopkinson Bar Fixture with prototype package 1 parts in each direction.

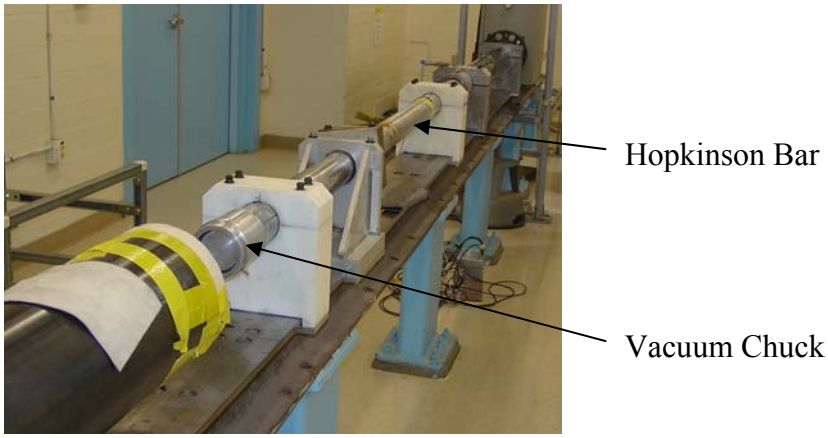

Figure 10-4. Hopkinson Bar showing vacuum chuck for holding fixture.

The normal environment thermal cycling was based on the worst case thermal shock specification in the normal environment envelope. Table 10-1 shows the thermal specification. A Thermotron SE-300-2 environmental chamber was used to apply these thermal loads to a set of parts. As in the shock tests, the continuity across the four wires bonded to the silicon chip in the package were checked after the test to determine any silicon cracking, wire-bond damage, or PCB connection failures.

Table 10-1. Normal Environment Device Temperature Cycle Profile

Step	Temperature (1)
1	Ramp from room temperature to +165ºF at ≥10ºF/minute
2	Dwell at 165ºF for 1 hour or until equilibrium is achieved (whichever comes first)
3	Ramp from +165ºF to -65ºF at ≥10ºF/minute
4	Dwell at -65ºF for 1 hour or until equilibrium is achieved (whichever comes first)
5	Ramp from -65ºF to room temperature at ≥10ºF/minute
Repeat steps 1-5 twenty-four (24) more times	
7	Dwell at room temperature for 1 hour or until equilibrium is achieved (whichever comes first)

Note for Table 10-1:
A dwell needs to last long enough for the test item to equilibrate with the chamber temperature. For purposes of this test plan, equilibrium is defined as the point where the internal (core) temperature of the test item is within 5ºF of the desired temperature.

10.1.2 Testing and Results

Three units of each of the two prototype package designs were subjected to 25 kG shocks in the X, Y, and Z directions and 50 kG shocks in the X, Y, and Z directions. Visual inspections were conducted after each test along with continuity checks for the wiring connected to the silicon chip inside the packages. Only one failure was noted for the shock testing. After a 50 kG shock in the Z direction, one wire on one of the prototype package 1 parts showed no connection to the other wires. This indicates that either the wire-bond or the PCB wiring connection failed after that shock. No visual damage was ever detected on any of the parts through the over-shock portion of the testing.-

After shock testing, the same parts were placed in the Thermotron chamber (Figure 10-5) and thermally cycled. The Thermotron was not able to reproduce the normal environment thermal cycles exactly, but it did well enough for the test to have merit. No failures were found after the thermal cycling.

Figure 10-5. Thermotron thermal chamber used to apply normal environment thermal shocks to prototype packages.

10.2 Package Epoxy Transmissibility

Initially, there was some concern about the transmissibility of the epoxy used between the aluminum block and the PCB in prototype package 1 (
Figure 10-1), so a small test was devised to measure this. A representative epoxy joint was tested to determine the transmissibility through the joint used in our application in the sense direction of the device. Two tests were used. In the first, a prototype part from previous tests was used on a fixture, also from previous tests. The results from this test were distorted enough by the dynamics of the system that a simpler test was constructed. The second test used a smaller and more simplified joint. The conclusion of these tests was that the transmissibility through this epoxy joint deviated from 1 by up to 60% depending on frequency.

10.2.1 Objectives and Approach

For both tests a B&K shaker and amplifier were used with a force rating of 10 lbs and a frequency bandwidth up to 20 kHz. Data was collected as velocities with Polytec laser Doppler velocimiters (LDVs) and a Polytec Data Management System.

The first case evaluated used a prototype package that had been used in previous testing. The epoxy joint in this case was thicker and had wires running through it. This, along with a fixture, also from a previous test, were attached to the B&K shaker with superglue. This case is illustrated in Figure 10-6.

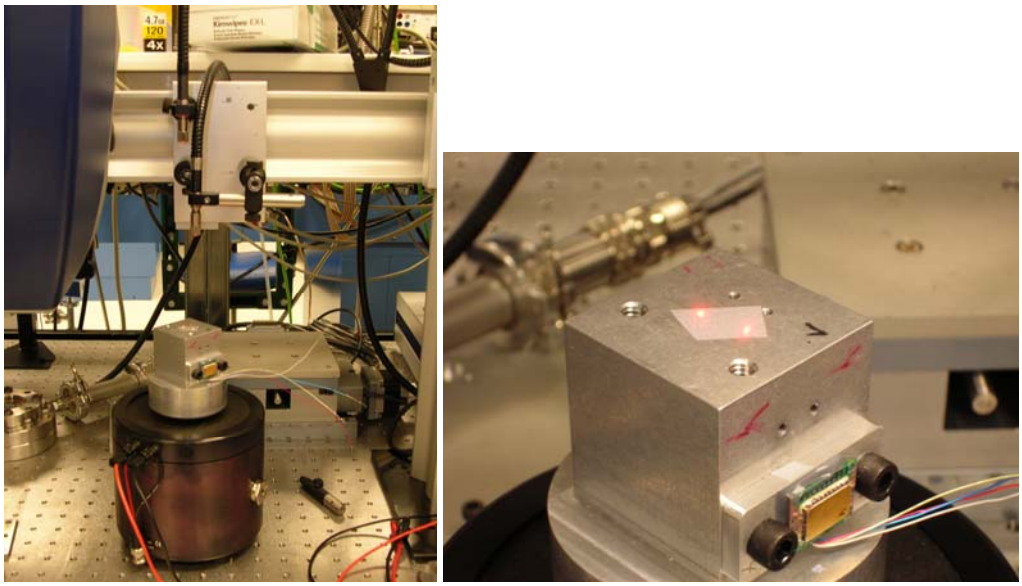

Figure 10-6. Test using prototype package and fixture used in previous test.

The second case used a simplified system that did not include the bolted joint and was significantly smaller overall. In this case the epoxy joint was much thinner than the previous joint with no wires running through it. The PCB with chip carrier was glued to the aluminum block with the epoxy being evaluated. The block was then bolted to the shaker.

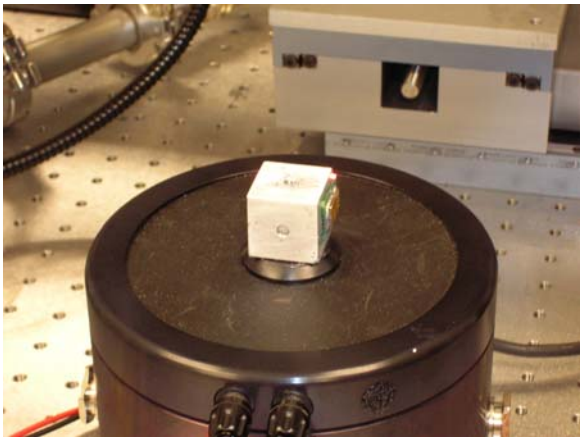

Figure 10-7. Test using simplified package approximation.

In either case, the information we were looking for was the transmissibility across the glue joint between the PCB and the metallic substrate.

10.2.2 Testing and Results

The measured transmissibilities from a close point on the metallic substrate to a corner of the PCB in the orientations shown in the photos above are shown in Figure 10-8 and Figure 10-9. Notice that the result for the first case deviates significantly from an ideal of 1 at higher frequencies. This could be due to many factors. Two of the most obvious possibilities are that the dynamics of the heavier, larger fixture and bolted joint contributed to the deviation. Also, the epoxy joint in case 1 is much thicker than in case 2.

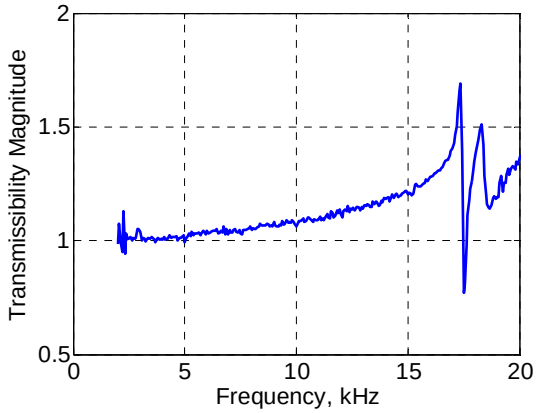

Figure 10-8. Results from case 1.

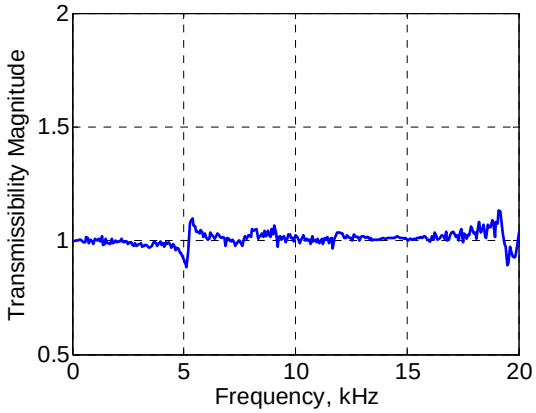

Figure 10-9. Results from case 2.

The epoxy joints in all cases exhibit amplification/attenuation that deviates <50% or so from the ideal of 1.

Due to the limited data collected, specific quantifiable conclusions are difficult to make. However, qualitatively, the transmissibility through the epoxy proposed for the packaging is no worse than that for the JM 7000 which will be used for die attach. It was noted during testing that dynamics of the rest of the package, i.e., the bolted connection, and the structure that the

device is bolted to, significantly affected test results. It seems unlikely that changes in the epoxy will make significant improvements in the system response.

10.3 Functional Testing of Packaged Parts

The functional testing of packaged shock switches is intended to do two things: 1) progress the device towards the goal of TRL 6; 2) close the loop on the design cycle for these devices. To achieve these goals a large test series was scheduled to start as soon as Revision 2 parts were available. This test series would include exercising key functionality before, during, and after exposure to thermal and vibration environments in order to conceptually meet environmental requirements for TRL 6. Unfortunately, due to packaging issues and functionality problems, most of the test series was cancelled and very little data was generated. For completeness, the test planning is documented here along with a short summary of the conclusions.

10.3.1 Objectives and Approach

Progressing the switch towards TRL 6 was the main goal of this testing. Fortunately, closing the design cycle would be accomplished along the way to showing TRL 6 for the device. The key to TRL 6 is successful "functional testing in relevant environments." For testing here, that is interpreted to mean that the key functionality of the shock sensor is exercised before, during, and after exposure to thermal and vibration environments.

The key functionality to assess includes:

- *Passive shock detection*: When the switch is exposed to shock within the expected range of applicability (shock magnitude and pulse width), the switch shall close a set of contacts. Further, the contacts shall remain closed until they are reset using the onboard thermal actuators.
- *State detection*: The contact resistance and electrical properties of the MEMS die shall remain constant and operable before and after shock events in order to facilitate switch state detection via continuity checks across the switch contacts.
- *Self-check using the on board thermal actuators*: It shall be possible to operate the on board actuators for purposes of opening and closing the contacts both before and after exposure to shock events. A self-check will be defined as a series of steps where the switches are opened, a pause is taken, the switches are closed, a pause is taken, and the switches are opened again. The switch will pass this self-check if the open/close conditions are achieved and maintained for the pause duration.

The first goal of testing is to verify that packaged parts function as expected before exposure to environments -- at room temperature. Then functionality parts will be tested under normal/during thermal extremes (prior to application of normal environments). The statistical results from these tests will be compared to analytical predictions of device models.

Contrary to similar tests for Revision 1 that were done partially on a centrifuge, these tests will all have to be shock tests in order to verify/exercise functionality. For testing below ~30 kG, a drop table will be used with multiple parts tested simultaneously. For testing above these levels, Hopkinson bar testing will have to be employed and parts will likely be tested singly or in pairs.

The analytically predicted switching threshold will be used as a starting point in the testing. The levels will be increased/decreased for subsequent tests to find a bracket for each switching threshold. For reference, see the FY06 report [1] for similar testing on Revision 1. This will be repeated for each of the four switch threshold values. Once the switching threshold brackets are established at room temperature, the tests will be repeated at 165 F and -65 F for a selected number of shock levels. The results will be correlated to the results at room temperature and compared to the analytical predictions for thermal sensitivity.

A minimum of 20 parts will be available for the 2.5 kG and 5 kG devices. A similar number of parts will be available for the unit with 10 kG and 25 kG devices. There is potential for up to 40 parts of each to be available. It is desired that as many parts be tested as possible.

The next step in the test series is to expose packaged Revision 2 switch parts to normal environments. These environments will be agreed upon with the environments group in department 1520; environments selected will be from representative systems for which the shock switch may be included in future development.

The normal environment specification includes transportation and handling environments through captive carry. They include thermal shock, vibration, and mechanical shock specifications. Parts that functioned successfully in the previous test series for functionality of pristine parts will be exposed to all of these environments in series. Monitoring of the switch states and periodic self-checks will be performed throughout the application of the normal environments. It is expected that the normal environments will have no effect on the switch state or health.

The third step in the test series is to verify that the packaged Revision 2 parts function as expected after being exposed to normal environments. The results will be compared to similar functionality data taken prior to exposure to normal environments. This testing is the same as the testing done with parts prior to application of the normal environments.

The final step in the test series is to perform margin tests on a limited number of shock switches. This will allow the definition of a survivable over-shock specification for the devices. To do this test the shock level applied to the switches will simply be incrementally increased until the switches reach a 50% failure condition. That is when 50% of the switches being tested have failed in any of the key functionality tests. Figure 10-10 shows the overall test flow.

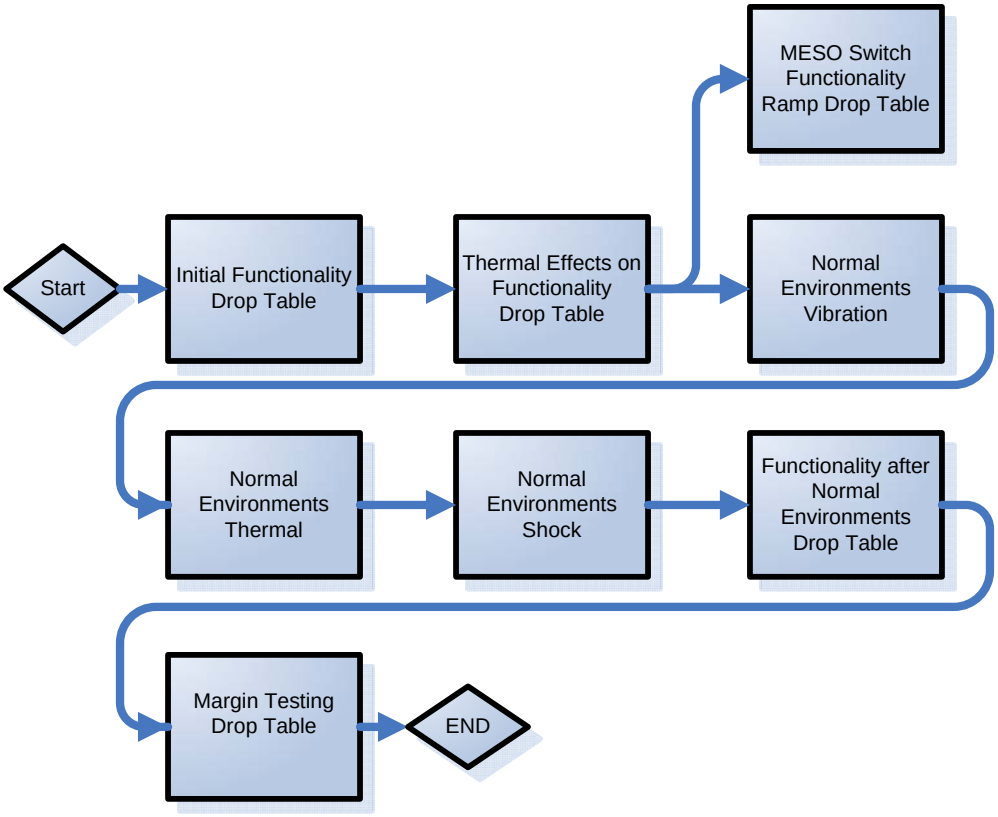

Figure 10-10. Test Flow Diagram.

A software program and PCB were developed by engineers in SNL/CA to check query the switch state and exercise the onboard open/close functionality switch contacts. The software allows one to check the current state of the switch, perform a self-check, and open/close any switch independently. The pause duration for the self-check along with the open/close voltage, open/close current limit, and open/close voltage application time are all adjustable. The software also allows one to save any of the state and self-check data along with a part serial number for data collection. Figure 10-11 shows the electronics diagram for the diagnostic system and Figure 10-12 shows the diagnostic software interface.

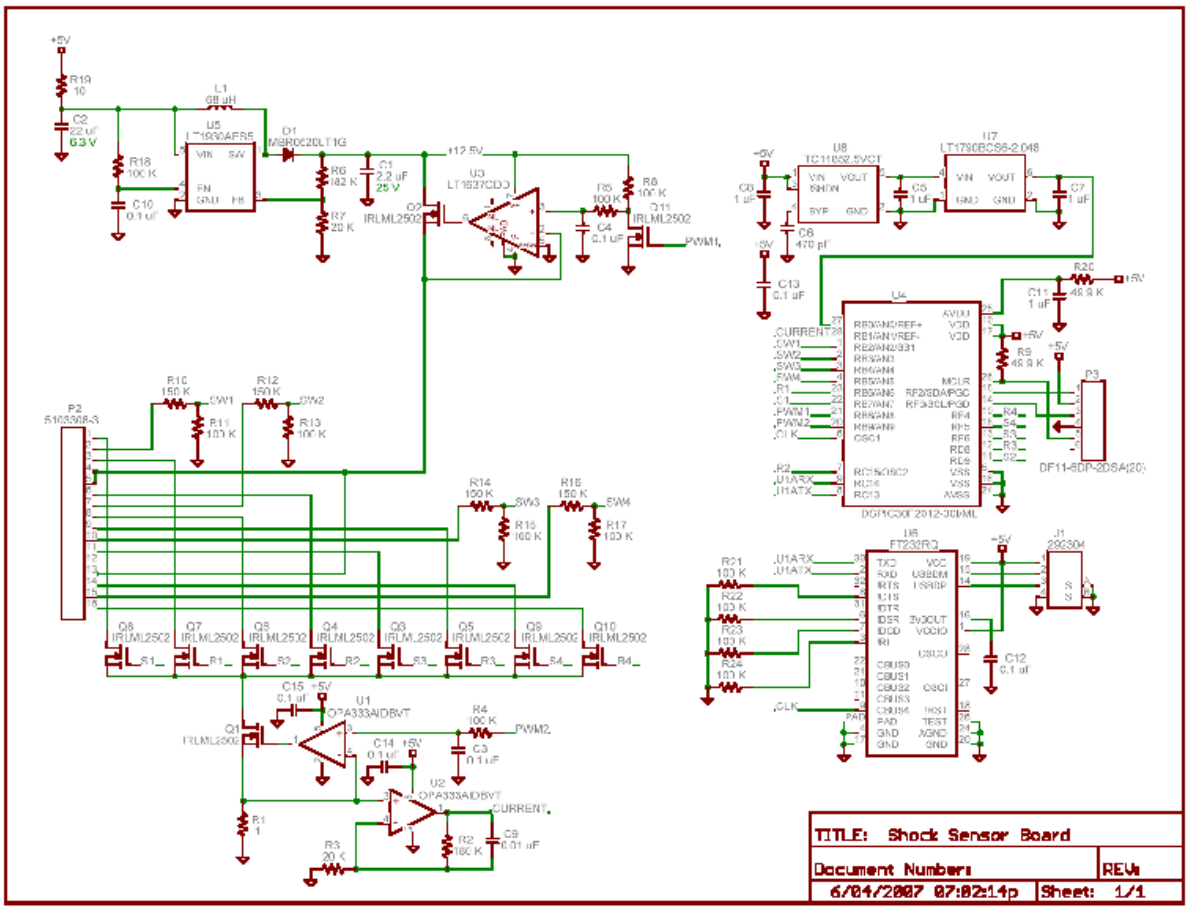

Figure 10-11. Schematic of shock sensor diagnostic electronics.

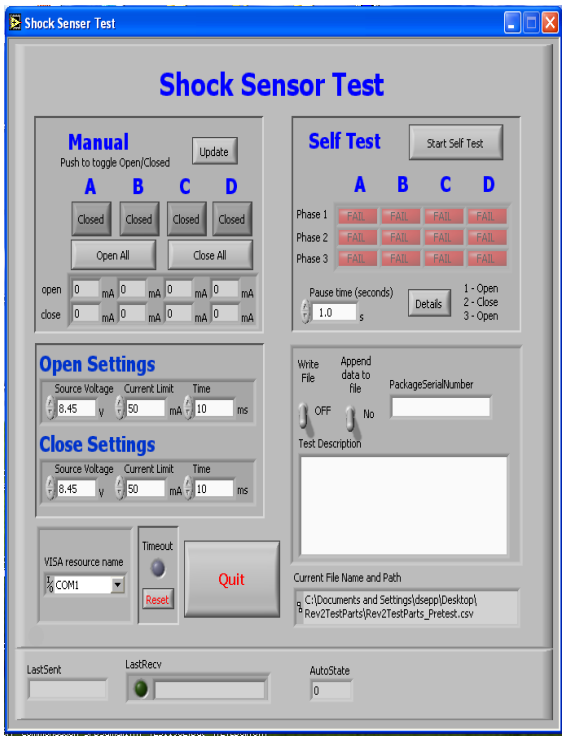

Figure 10-12. Screenshot of diagnostic software.

The fixture used for shock table testing is a 5.25” cube that can have up to six units on each of three faces. Five of these fixtures are available. Four will be assembled with units and the fifth will be used for calibration of the drop tables. These fixtures allow up to 6 axes of shock input to any one of the units depending on how they are mounted. Shock switch packages are mounted on three faces. This fixture is very convenient because it allows for simultaneously testing of switches along all three principal axes of the switch. In one test, switches with their sense axis aligned along drop table axis will receive shock along their sense axis while switches that are mounted on other faces will experience off-axis shock.
Figure 10-13 shows a solid model of the fixture as it will be used.

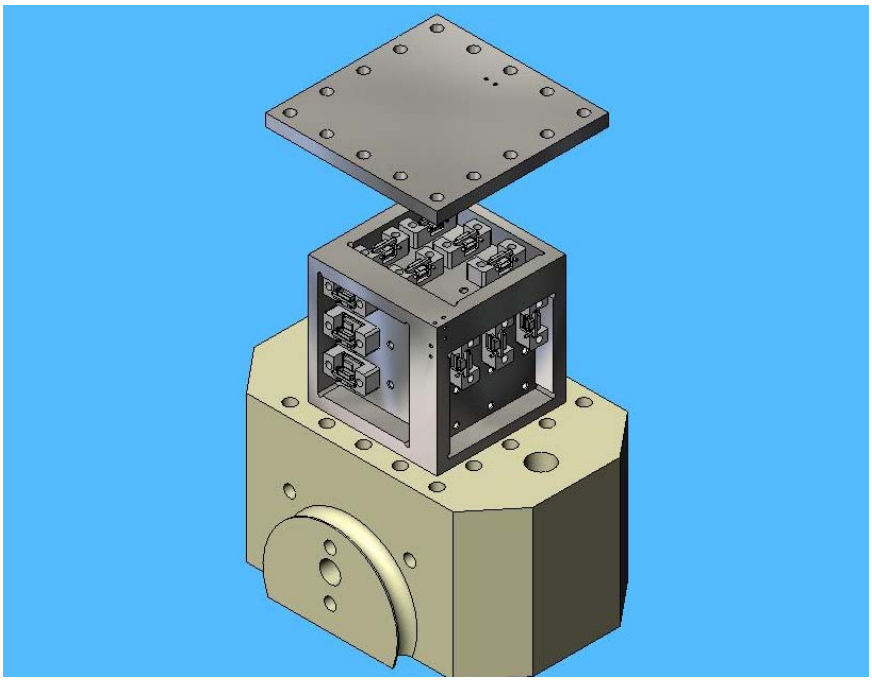

Figure 10-13. View of the MEMS unit fixture showing drop table carriage, fixture block, and clamp plate.

10.3.2 Testing and Results

The initial portion of the testing focused on switch functionality for the lower level switches at room temperature conditions. The 64 packaged parts delivered for testing contained die with M2A, M2B, J2A, and J2B devices on them. These devices had nominal switch thresholds based on models of 2486 G, 4985 G, 3294 G, and 5168 G, respectively. The initial tests were done on a drop table shock machine that allowed for shocks up to ~25 kG with a duration of ~0.3ms. Testing started with the switch nominal values and the plan was to find brackets for the switch thresholds. Unfortunately, only a few switches ever closed during testing of shocks up to 20 kG, and there were no discernable patterns in the switch closures. Table 10-2, Table 10-3, and Table 10-4 show some representative results from a few of the tests. Note that as testing proceeded some parts were removed for failure analysis and shock levels above 10 kG were applied to only a subset of the original parts. The tables indicate "broken" if the parts failed either the self-check before the test or the one after the test or both. The tables indicate "open" if the switches passed both self-checks and did not switch states. The tables indicate "closed if the switches passed both self-checks and switched states.

Table 10-2. Revision 2—First Shock Test. 2500 G in the Y1 Direction

Orientation	SerialNum	J2A	J2B	M2A	M2B
Y1	S88	open	broken	broken	open
	S95	broken	open	closed	open
	S81	broken	broken	open	open
	S80	open	closed	open	broken
	S94	open	open	open	open
	S93	open	broken	broken	broken
Y2	S99	open	broken	closed	closed
	S85A	open	broken	broken	open
	S86	open	broken	broken	broken
	S100	open	broken	broken	open
Y3	S101	open	broken	broken	broken
	S98	open	broken	broken	closed
	S85	open	closed	broken	open
	S97	open	open	closed	open
	S84	open	open	open	open
	S96	open	open	open	open
Y1	S129	open	broken	broken	broken
	S103	open	broken	broken	closed
	S128	open	open	broken	broken
	S105	broken	broken	broken	broken
	S127	broken	broken	broken	broken
	S110	closed	closed	broken	broken
Y2	S113	open	open	broken	broken
	S111	open	broken	broken	broken
	S114	open	broken	broken	broken
	S116	broken	broken	broken	broken
Y3	S79	closed	closed	closed	closed
	S92	broken	broken	open	open
	U	closed	closed	broken	broken
	S120	open	open	closed	broken
	S123	open	broken	broken	broken
	S125	open	broken	broken	broken
Y1	S135	open	broken	closed	closed
	S138	broken	broken	open	open
	S134	closed	closed	open	open
	S139	open	open	open	open
	S133	broken	open	broken	open
	S137	closed	broken	closed	open
Y2	S75	broken	open	broken	open
	S76	open	broken	broken	open
	S87	broken	broken	closed	open
	S89	open	broken	open	open
Y3	S77	broken	broken	open	open
	S130	broken	open	open	open
	S78	broken	open	open	open
	S131	closed	open	open	open
	S91	open	open	open	open
	S132	open	open	open	open
Y1	S69	broken	broken	open	open
	S59	open	open	open	open
	S70	open	open	open	open
	S60	open	open	open	open
	S72	open	open	open	open
	S65	broken	open	broken	open
Y2	S140	open	open	closed	open
	S147	open	open	open	open
	S145	open	open	open	open
	S58	broken	open	open	open
Y3	S50	broken	open	open	open
	S47	broken	open	open	open
	S53	open	broken	open	open
	S49	open	broken	broken	open
	S45	broken	open	closed	open
	S46	broken	broken	open	open

Table 10-3. Revision 2—23rd Shock Test. 6000 G in the Y3 Direction

Orientation	SerialNum	J2A	J2B	M2A	M2B
Y1	S88	open	broken	broken	open
	S80	open	closed	broken	broken
	S94	broken	broken	broken	open
	S93	closed	closed	closed	open
Y2	S99	open	broken	open	broken
	S85A	open	broken	broken	open
	S86	open	broken	closed	broken
	S100	open	open	open	open
Y3	S101	open	broken	open	broken
	S98	broken	open	open	open
	S85	closed	open	open	open
	S97	open	broken	open	open
	S84	open	open	open	open
	S96	open	open	open	open
Y1	S129	open	open	broken	open
	S103	open	broken	broken	broken
	S105	broken	open	broken	closed
	S127	open	open	closed	broken
	S110	open	open	broken	closed
Y2	S113	open	open	open	broken
	S114	open	open	broken	broken
	S116	open	open	broken	broken
Y3	S79	open	open	closed	open
	S92	open	open	open	open
	U	open	open	broken	open
	S120	open	open	closed	open
	S123	open	open	open	broken
	S125	open	broken	broken	open
Y1	S135	open	open	closed	open
	S138	open	open	open	open
	S134	open	open	open	open
	S139	open	open	open	open
	S133	broken	open	broken	open
	S137	closed	open	closed	open
Y2	S75	open	open	open	open
	S76	broken	broken	broken	open
	S87	closed	broken	closed	open
	S89	broken	closed	broken	open
Y3	S77	closed	open	open	open
	S130	open	open	open	open
	S78	broken	open	open	open
	S131	closed	open	open	open
	S91	open	open	open	open
	S132	open	open	open	open
Y1	S69	broken	broken	open	open
	S59	open	open	open	open
	S70	broken	open	open	open
	S60	open	open	open	open
	S72	broken	open	open	open
	S65	broken	open	broken	open
Y2	S140	open	open	closed	open
	S147	open	open	open	open
	S145	open	open	open	open
	S58	broken	open	open	open
Y3	S50	broken	open	open	open
	S47	broken	open	open	open
	S53	open	open	open	open
	S45	broken	open	open	open

Table 10-4. Revision 2—31st Shock Test. 20kG in the Y1 Direction.

Orientation	SerialNum	J2A	J2B	M2A	M2B
Y1	S69	broken	broken	open	open
	S59	open	open	open	open
	S70	broken	open	open	open
	S60	closed	open	open	open
	S72	broken	open	open	open
	S123	open	open	open	broken
Y2	S125	broken	broken	broken	closed
	S147	closed	open	closed	open
	S145	open	open	open	open
	S58	broken	open	open	open
Y3	S50	broken	closed	closed	closed
	S47	broken	open	open	open
	S53	broken	open	open	open
	S85	open	open	open	open
	S45	broken	open	open	open
	S97	open	broken	open	open

Test results indicate a random closure of switches that does not seem to correlate with shock level or direction. A test was conducted in which all the switches were run through a self-check, left for 15 minutes with no shock inputs, and checked for state changes. The results of this small test indicate that there is a problem with spontaneous closure of the switches. In fact, based on these results, the closures seen in the tables above are likely spontaneous with no relation to the shock input.

Another interesting observation from the tables above is that the devices seem to repair themselves after being shocked multiple times. This can be seen clearly in Table 10-2 and Table 10-3 since there are significantly fewer "broken" indications in the second table.

All of this data seems to indicate that the parts are completely non-functional in a shock environment.

11. CONCLUSIONS

11.1 FY07: Summary and Significant Findings

The MEMS passive shock sensor team worked to mature the MEMS shock sensor and this report details many of the associated activities. In FY07, the team designed and submitted for fabrication three revisions of the MEMS passive shock sensors, delivered packaged prototypes to three potential customers, matured packaging solutions, conducted tests and validation studies, and discovered several important modes of failure for the MEMS passive shock sensor. Modes of failure included packaging processes and MEMS die level design issues. For each mode of failure, the team developed plans for a path forward and for success.

The modes of failure for the MEMS passive shock sensor and the planned path forward in FY08 are

- JM7000 contamination (processing issue) – path forward: use correct oven, temperatures, cure schedule and vacuum bake-out
- Particles (processing issue) – reduce handling as much as possible; design new metallization fixture
- cracked/broken bond pads (processing issue) – center wire bonding tool tip over bond pad; conduct pull tests develop process of determining force required to place bond
- silicon welding– float contacts and develop new process for isolation nitride layers placed appropriately
- friction: mass/lid, mass/substrate– remove dimples on and around mass; develop and understanding of why mass is deflected

12. REFERENCES

[1] J.A. Mitchell, J.W. Wittwer, M.S. Baker, N. Spencer, K.P. Pohl, R.C Clemens, D.S. Epp, J.C. Gilkey, L.M. Phinney, W. Wilbanks, W.Y. Lu, *On the Design, Packaging and Testing of Micro- and Meso-scale Inertial G-Relays*, SAND2006-5806. Sandia National Laboratories, Albuquerque, NM, 2006.

[2] J.A. Mitchell and B.R. Bailey, On the Integration of Technology Readiness Levels at Sandia National Laboratories, SAND2006-5754, Sandia National Laboratories, Albuquerque, NM, September 2006.

[3] J.A. Mitchell, "Technology Readiness and Assessment," Sandia National Laboratories Internal Restricted Network, http://www-irn.sandia.gov/trl, 2007.

[4] M.S. Baker, R.A. Plass, T.J. Headley, and J.A. Walraven, *Final Report: Compliant Thermo-Mechanical MEMS Actuators LDRD #52553*, SAND2004-6635. Sandia National Laboratories, Albuquerque, NM, December 2004.

[5] J.W. Wittwer, M.S. Baker, and L.H. Howell, Robust Design and Model Validation of Nonlinear Compliant Micromechanisms, in *Journal of Microelectromechanical Systems*, Transactions of the IEEE and ASME, Vol. 15, No. 1, pp. 33-41, February 2006.

[6] J.J. Sniegowski and M.P. de Boer, IC-Compatible Polysilicon Surface Micromachining, in *Annu. Rev. Mater. Sci*., Vol. 30, pp. 299-333, 2000.

[7] B.D. Jensen, M.B. Parkinson, K. Kurabayashi, L.L. Howell, and M.S. Baker, Design Optimization of a Fully-Compliant Bistable Micro-Mechanism, in *Proceedings of IMECE 2001*, ASME International Mechanical Engineering Congress & Exposition, New York., Nov. 11-16, 2001.

[8] Y.B. Gianchandani and K. Najafi, Bent-Beam Strain Sensors, *Journal of Microelectromechanical Systems*, Vol. 5, No. 1, pp. 52-58. 1996.

[9] E.I. Cole Jr., P. Tangyunyong, D.A. Benson, and D.L. Barton, TIVA and SEI Developments for Enhanced Front and Backside Interconnection Failure Analysis, in *ESREF*, pp. 991-996, 1999.

[10] E.I. Cole Jr. and R.E. Anderson, Rapid localization of IC open conductors using charge-induced voltage alteration (CIVA), in *IRPS*, pp 288-298, 1992.

[11] E.I. Cole Jr., J.M Soden, J.L. Rife, D.L. Barton, and C.L. Henderson, Novel failure analysis techniques using photon probing in a scanning optical microscope, in *IRPS*, pp. 388 – 398, 1994.

[12] R.A. Serway, *Physics for scientists & engineers with modern physics*, 2nd edn., pp 605-606. Saunders Publishing Co., New York, 1986.

[13] K. Nikawa and S. Inoue, Various contrasts identifiable from the backside of a chip by 1.3 μm laser beam scanning & current changing imaging. in *ISTFA*, pp. 387-392, 1996.

[14] K. Nikawa and S. Inoue, New capabilities of OBIRCH method for fault localization and defect detection, in *Proc. of Sixth Asian Test Symposium*, p. 219, 1997.

[15] J.A. Walraven, E.I. Cole Jr., and P. Tangyunyong, Failure Analysis of MEMS Using Thermally-Induced Voltage Alteration, *Proceedings from the 26th ISTFA*, pp. 489-496. 2000.

[16] R.P. O'Reilly, High G Testing of MEMS Devices, in *Proc. Of SPIE Vol. 6111*, 61110I-1, 2006.

APPENDIX: METALLIZATION CHECKLIST

Record S number from gel-pak: _____

- ☐ Receive MEMS devices
  Date: _____ Time: _____ Initials: _____

- ☐ Motor speed set to 10.0, deposition rates set to 5Å /s (Ti) and 8Å/s (Pt), tooling factors set to previous run values.
  Completion date: _____ Time: _____ Initials: _____

- ☐ Perform calibration run/runs of evaporation system and record all relevant information on Process Data Sheet.
  Completion date: _____ Time: _____ Initials: _____

- ☐ Inspect devices and note irregularities/defects on Process Data Sheet. Load devices and witness into MEMS FIXTURE.
  Completion date: _____ Time: _____ Initials: _____

- ☐ Conduct 10 minute UV Ozone clean.
  Completion date: _____ Time: _____ Initials: _____

- ☐ Remove fixture from clean system and mount on 45 degree rotating stage inside vacuum system process chamber. Begin pump down.
  Completion date: _____ Time: _____ Initials: _____

- ☐ Pump down vacuum deposition system to a pressure $< 1.0 \times 10^{-6}$ Torr.
  Completion date: _____ Time: _____ Initials: _____

- ☐ Calculate and Set new tooling factors based on calibration run results (if necessary).
  Completion date: _____ Time: _____ Initials: _____

- ☐ Deposit 500 A Titanium and 4250 A Platinum. Record all relevant process information on Process Data Sheet.
  Completion date: _____ Time: _____ Initials: _____

- ☐ Allow 1 hour minimum post-deposition cool down. Vent system to atmosphere and remove fixture from rotating stage. Remove MEMS devices from fixture and place back in original gel-pak container that the parts were delivered in.
  Completion date: _____ Time: _____ Initials: _____

- ☐ Measure thickness on witness sample and print thickness scan.
  Completion date: _____ Time: _____ Initials: _____

- Deliver finished product (MEMS in original gel-pak), Process Checklist (this form), complete Process Datasheet, and thickness scan to customer.
  Completion date: _____ Time: _____ Initials: _____

DISTRIBUTION

1	MS0340	John L. Sichler, 2123
1	MS0340	Steve Harris, 2123
1	MS0343	Mary E. Gonzales, 2120
1	MS0344	George Clark, 2626
1	MS0372	James M. Redmond, 1525
1	MS0421	Michael R. Sjulin, 0240
1	MS0427	Robert A. Paulsen, 2011
1	MS0447	Matt Kerschen, 2111
1	MS0530	Hae-Jung L. Murphy, 2623
1	MS0633	Todd Sterk, 2952
1	MS0824	Tze Y. Chu, 1500
1	MS0847	Peter J. Wilson, 1520
1	MS1064	Joel B. Wirth, 2614
1	MS1064	Rebecca C. Clemens, 2614
1	MS1064	Ernest J. Garcia, 2614
1	MS1064	Marc A. Polosky, 2614
4	MS1064	John A. Mitchell, 2614
1	MS1069	Mark R. Platzbecker, 1749-1
1	MS1069	Michael S. Baker, 1749-1
1	MS1069	Danelle M. Tanner, 1749-1
1	MS1069	Jonathan W. Wittwer, 1749-1
1	MS1070	Channy C. Wong, 1526
1	MS1070	Jill Blecke, 1526
1	MS1070	David S. Epp, 1526
1	MS1080	Keith Ortiz, 1749
1	MS1081	David J. Stein, 1726
1	MS1081	Jeremy A. Walraven, 1726
1	MS1160	Douglas A. Dederman, 5431
1	MS1415	David R. Sandison, 1110
1	MS1415	Carlos Gutierrez, 1114
1	MS1415	Douglas A. Crowson, 1114
1	MS1415	Jack E. Houston, 1114
1	MS9042	Davina M. Kwon, 8770
1	MS9102	James F. Stamps, 8235
1	MS9102	Paul Y. Yoon, 8235
1	MS9153	Russell G. Miller, 8240
1	MS9154	Janson Wu, 8244
1	MS9154	Jennifer Chan, 8244
1	MS9154	Judy Lau, 8244
1	MS0899	Technical Library, 9536 (electronic copy)


Sandia National Laboratories